

GEOFORSCHUNGSZENTRUM POTSDAM
STIFTUNG DES ÖFFENTLICHEN RECHTS

Xueqing Li

A Receiver Function Study of the Northwest Pacific Subduction Zone and the Hawaiian Mantle Plume

Scientific Technical Report STR00/19

URN: urn:nbn:de:kobv:b103-00199
DOI: <https://doi.org/10.2312/GFZ.b103-00199>

Imprint

GeoForschungsZentrum Potsdam
Telegrafenberg
D-14473 Potsdam

e-mail: postmaster@gfz-potsdam.de
www: <http://www.gfz-potsdam.de>

Printed in Potsdam/Germany
September 2000

Xueqing Li

A Receiver Function Study of the Northwest Pacific Subduction Zone and the Hawaiian Mantle Plume

Dissertation
zur Erlangung des Doktorgrades
am Fachbereich Geowissenschaften
der Freien Universität Berlin

Juni 2000

Scientific Technical Report STR00/19

A Receiver Function Study of the Northwest Pacific Subduction Zone and the Hawaiian Mantle Plume

Dissertation
zur Erlangung des Doktorgrades
des Fachbereichs Geowissenschaften
der Freien Universität Berlin

vorgelegt von
Xueqing Li
Juni 2000

A Research Project Study of
the Northwest Pacific Subduction Zone
and the Hawaiian Island Chain



Jiv - Nr. 20 - 2000539

Tag der mündlichen Prüfung: 18 Juli 2000

Erstgutachter: Prof. Dr. Rainer Kind

Zweitgutachter: Prof. Dr. Serge Shapiro

Contents

1	Introduction	5
1.1	Earth's structure	5
1.2	Mantle convection system	6
1.3	Plan of this work	7
2	The upper mantle discontinuities	9
2.1	Seismic observations	9
2.2	The nature of the 410 and 660	12
2.3	Subduction and mantle plume	14
2.4	The metastability	15
2.5	Discrepancies	16
2.6	Other discontinuity hypotheses	19
2.7	Other discontinuities in the upper mantle	20
3	Receiver Function Method	21
3.1	Principle processing steps of receiver functions	25
3.1.1	Data selection	25
3.1.2	Restitution	26
3.1.3	Rotation	28
3.1.4	Deconvolution	32
3.2	Amplification of weak converted energy	33
3.2.1	Stacking method	33
3.2.2	Moveout correction	34
3.2.3	Migration method	37
3.3	Receiver function inversion	38
4	The northwest Pacific subduction zone	39
4.1	Introduction	39

4.1.1	Previous studies of the 660	41
4.1.2	Previous studies of the 410	42
4.2	Data	43
4.3	Receiver function analyses	49
4.3.1	General features	49
4.3.2	Topography of the 410 and 660	52
4.4	Further discussions on the 410 and 660 topography	59
4.4.1	The continental stations HIA, BJI and SSE	59
4.4.2	Stations MDJ and INCN	61
4.4.3	Beneath Japan	63
4.5	The subducted Pacific slab	71
4.5.1	North Honshu (station TMR)	72
4.5.2	Central Honshu (stations FUJ, KFU and SGN)	72
4.5.3	The low velocity zone beneath MAJO	74
5	The Hawaiian mantle plume	77
5.1	Data	79
5.2	Topography of the 410 and 660	81
5.2.1	Beneath the island of Oahu	81
5.2.2	Beneath the island of Hawaii	84
5.2.3	Thinning of the mantle transition zone	85
5.3	The low velocity zone in the uppermost mantle	87
5.3.1	Island of Oahu	87
5.3.2	Island of Hawaii	90
5.4	Implication for the Hawaiian mantle plume conduit	94
6	Conclusions and discussion	97
6.1	Conclusions	97
6.2	Short discussion of global receiver functions	100
	Zusammenfassung	103
	Bibliography	107
	Danksagung	123
	Lebenslauf	124

Chapter 1

Introduction

1.1 Earth's structure

The Earth is composed of silicate and iron-alloy materials. Over the wide range of interior pressure and temperature conditions, the Earth responds like a viscous body under the application of long-duration of forces (global convection), but nearly elastically under the application of small-magnitude transient forces (earthquakes). The propagation of seismic waves in the Earth's interior can be recorded as ground motion which reveal many characteristics of the Earth. Seismology is one of the most important methods to study the Earth's interior.

The first seismometer was invented by Filippo Cecchi in Italy in 1875, while 1889 the first accurate teleseismic recording was obtained in Potsdam, Germany, 15 minutes after an earthquake in Japan. In 1892 John Milne developed a seismometer that was sufficiently compact to be installed in about 40 observatories around the world, making the beginning of the systematic collection of global seismic data.

Seismic waves probe the Earth's deep interior. In 1906 the Earth's core was discovered by Oldham, and in 1913 Gutenberg determined the depth to the core-mantle boundary of 2900 km. In 1909 Mohorovičić discovered the crust-mantle boundary (Moho), and in 1936 the Earth's inner core was discovered by Inge Lehmann. By 1939 Sir Harold Jeffreys compiled the travel times of thousands of seismic arrivals and developed the first detailed cross section of the Earth from surface to center (Jeffrey-Bullen tables). The recent development of seismology has thrown light on lithospheric and asthenospheric features and also on the directions of mantle convective flow.

According to radial seismic velocity changes, the Earth can be divided into crust, mantle and core. Discontinuities separate regions of smooth variations of seismic velocity inside the Earth.

At the Moho the P velocity increases abruptly from 6.0–6.5 km/sec in the crust to 7.8–8.2 km/sec in the mantle. In some cases a single reflector at the Moho is indicated; in others there appears to be a double or a number of reflectors with no certain discontinuity level. The depth of Moho changes dramatically in different geological regions, i.e. from less than 10 km under oceans to more than 80 km under mountain ranges. The crust is the most heterogeneous and anisotropic, but the best studied layer of the Earth.

The Earth's mantle is subdivided into the upper and lower mantle. In the upper mantle there is more heterogeneity and all earthquakes are limited within it. Its base is marked on a global scale by a seismic discontinuity at 660 km depth (the 660 hereafter) where velocity and density increase by about 5%. Another global seismic discontinuity in the upper mantle is located at about 410 km depth (the 410 hereafter). It has a smaller velocity and density contrast than the 660. The region between 410 and 660 km depth is often denoted the "transition zone". There are also reports about regional existence of weak discontinuities at 520 km and 210 km depths in the upper mantle (e.g. Anderson, 1979; Shearer, 1996; Vidale and Benz, 1992).

The core is below the mantle and it is composed predominantly of iron. It can be divided into a liquid outer and solid inner part, separated by a discontinuity at 5155 km depth. The outer core is believed to be the generator of the earth magnetic field. The inner core is highly anisotropic.

The basic concept in modern plate tectonics is that of a mobile lithosphere on the Earth's surface. Relative motions between mosaic surfaces of lithospheric plates are accommodated at plate boundaries. The essence of lithospheric motions is large horizontal transport, from creation to destruction of the plate. The lithosphere includes the crust and part of the upper mantle. Below the lithosphere is the asthenosphere, a region with low strength, possibly decoupled from the lithosphere and characterized by relative low velocity. The temperature there probably approaches melting. Its depth is often taken to be as 60–200 km.

Two frequently used radial layered Earth models are the IASP91 (Kennett and Engdahl, 1991) and the PREM (Dziewonski and Anderson, 1981). The Moho in the IASP91 is at 35 km depth, adequately representing a continental structure. The PREM model has a crust thickness of 24 km. A discontinuity at 220 km depth is included in the PREM model.

1.2 Mantle convection system

Heat in the Earth has been produced by radioactive decay, the release of gravitational energy during the accretion of the Earth and by the separation of the core from the mantle. This has resulted in convection at rates of centimeters per year. As Jeffreys pointed out, the Earth's mantle must flow as it cannot sustain masses such as mountain ranges higher than about 10 km. There is

much discussion on the amount of interactions between the upper and lower mantle convection, i.e. whether there is whole mantle convection or separate systems in the two sections.

It was argued (see Ringwood and Irifune, 1988) that young plates of descending oceanic lithosphere which approach temperature equilibrium with the mantle at 650 km depth may become trapped to form a gravitationally stable chemical and thermal boundary layer separating the upper and lower mantle, while mature plates may be buckled and thickened when they encounter this boundary layer, puncture the layer and ultimately enter the lower mantle. Mass-balance considerations require that an equivalent volume of lower mantle material would then ascend as mantle plumes through the boundary layer and become mixed into the upper mantle. According to this model, a dynamic equilibrium is established between young subduction processes that establish and maintain a boundary layer at 660 km depth to isolate the upper and lower mantle, and mature subductions and mantle plumes that cause substantial exchange of material and mixing between the upper and lower mantle. On the other hand, where the boundary layer of former oceanic lithosphere at 660 km depth remains intact, it serves to isolate the upper and lower mantle so that a layered convective system is formed.

Creager and Jordan (1986) claimed they have evidence of subducted plates penetrating into the lower mantle. Olson et al. (1990) proposed that whole mantle convection is consistent with seismic tomography, mantle geochemistry and numerical modeling of convection. The 660 discontinuity itself now becomes an investigative tool rather than a target. The depth variation of upper mantle discontinuities is an important clue to reveal the mantle convection regime.

1.3 Plan of this work

Seismological models of upper mantle structure provide important constraints on the Earth's convection system. Resolving the details of the upper mantle discontinuities is important for modeling the composition of the mantle and for understanding the effect that the discontinuities may have on mantle convection.

Recently, numerous permanent and temporary seismic stations and networks have been set up around the world. It is possible to get the seismic records for the research needs from data management systems like IRIS, GEOFON, GEOSCOPE, FREESIA, etc. The use of seismograms collected from a large number of stations and earthquakes around the world enable us to study the global and the regional structure of the Earth.

In this work, the receiver function technique (e.g. Owens et al., 1984; Kind et al., 1995) is applied to study the upper mantle structure in the northwest Pacific subduction zone and in the Hawaiian hotspot area. In the northwest Pacific, the Pacific plate is subducted into the upper mantle to more than 600 km depth, indicated by seismicity. In Hawaii, the volcanic

edifice of the Hawaiian islands and seamounts are believed to result from the passage of the oceanic lithosphere over a stationary mantle hotspot (Wilson, 1963; Morgan, 1971; Morgan et al., 1995). In both regions the upper mantle structure is affected by the cold and warm materials, respectively. To study the extension of the temperature anomaly is important for understanding the Earth's convection system.

The olivine component of the mantle material is intensively studied in laboratories (e.g. Ito and Takahashi, 1989; Irifune, 1987). With increasing temperature and pressure, the olivine crystal undergoes a series of phase transformations which will result in a variation of the seismic structure. The effect of the temperature anomaly on the main upper mantle discontinuities will be discussed in chapter 2.

Recently, the receiver function technique is increasingly applied to investigate the upper mantle discontinuities. To isolate the upper mantle conversion phases, newly developed move-out correction and migration methods are applied to separately distributed seismic stations as well as station arrays. The receiver function method used in this study will be introduced in chapter 3.

In chapter 4 and 5, receiver function studies in the area of the northwest Pacific subduction zone and the Hawaiian mantle plume are presented. Regional tectonic background and the previous seismological works in these two areas will be first introduced in each chapter, and followed by description of data, processing steps, results and interpretations.

In chapter 6, I will summarize the observations of the 410 and 660 topography in the northwest Pacific subduction zone and in the area around the Hawaiian mantle plume.

Chapter 2

The upper mantle discontinuities

2.1 Seismic observations

As early as in the 1940s it was clear that at a distance of about 15° there is an abrupt change of the ray parameters associated with the first arrival travel-time curves of P and S waves. It was not until the 1960s the seismic data were adequate to reveal two triplications in the travel-time curves at a distance of 15° to 30° , leading to the discovery of two mantle discontinuities at depths of 410 and 660 km. These triplications arise from the waves grazing along the discontinuities with strong reflections and refractions and these phases dominate the upper mantle seismic signals. With short-period seismograms recorded by a seismic array in southern California, Walck (1984) showed clearly the two upper mantle triplications. By fitting the travel times and amplitudes of direct P and S waves, the upper mantle velocity structure can be obtained (Priestley et al., 1994; Mechie et al., 1997; Ryberg et al., 1996, 1997, 1998).

The upper mantle discontinuities are observable by diverse seismic methods. There is a variety of phases which are converted from or reflected at the top or bottom side of the discontinuities. Each phase can be observed within a certain distance range which is favourable for observing and isolating it from the seismic wave field. These secondary phases arrive at a seismic station earlier or later than the originating direct waves depending on the reflection and/or conversion geometry. Usually they are studied by comparing them with the direct waves because of the similar raypaths in the mantle (and in the core for some phases). Their differential travel times relative to the direct waves are related to the discontinuity's depth and their amplitudes and the frequent contents provide information on the velocity and density contrasts as well as the sharpness of the discontinuity. Possible phases that have been used are summarized below and their raypaths are illustrated in Fig. 2.1.

multiple ScS reverberations: A bunch of multiple reflections from the upper mantle discon-

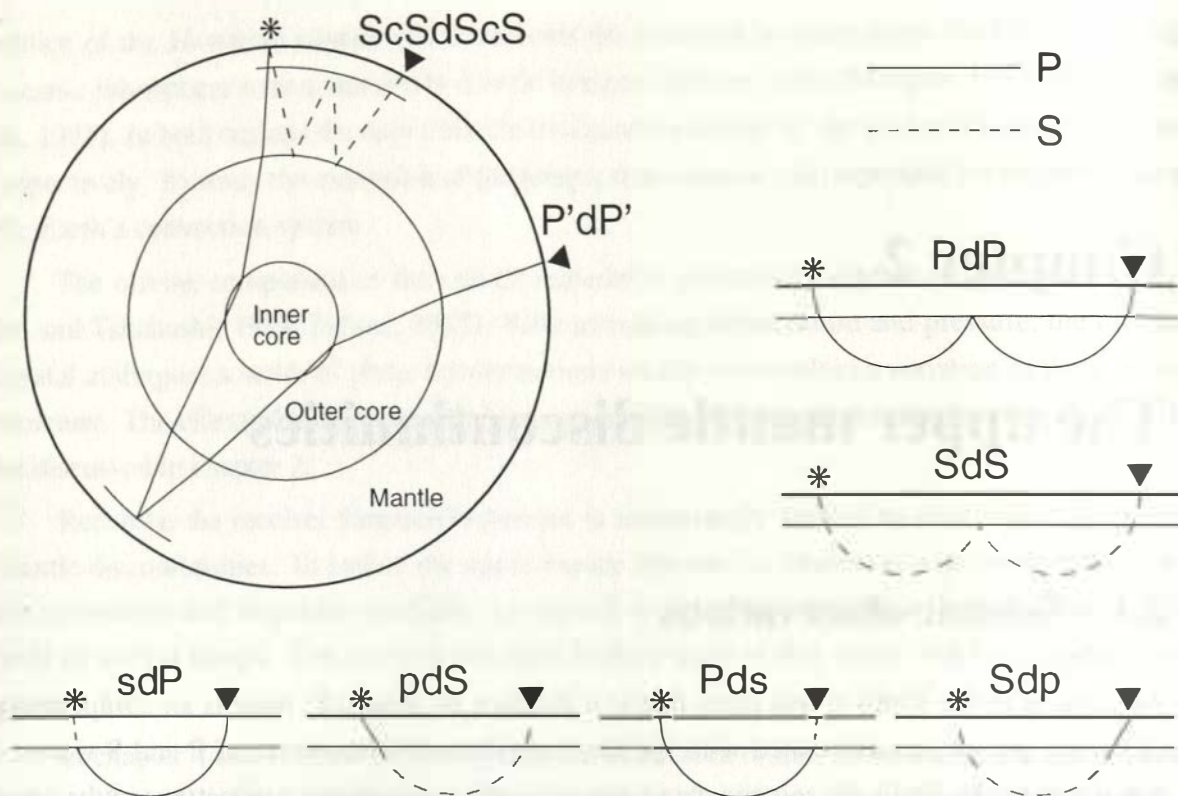


Figure 2.1: Sketch showing different secondary seismic phases used to detect upper mantle discontinuities. They are: multiple ScS reverberations; underside reflections recorded as precursors to P'P'; underside reflections recorded as precursors to PP and SS; source-side conversions sdP and pdS; and receiver-side conversions Pds and Sdp.

tinuities can be generated from long-period (> 20 sec) waves of multiple core-mantle boundary reflections ScS_n . An example of these phases is shown in Fig. 2.1 (ScSdScS). The multiple ScS reverberations have been intensively studied with intermediate and deep-focus earthquakes surrounding China (Revenaugh and Jordan, 1991a,b; Revenaugh and Sipkin, 1994a,b).

Precursors to PP, SS and P'P': Underside reflections from upper mantle discontinuities are observed as precursors to a number of the reference waves which are reflected at Earth's surface. According to the reference phases these studies include:

- **Precursors to SS**, from which the 410 and 660 have been observed and mapped globally (e.g. Shearer, 1991; Shearer and Masters, 1992; Shearer, 1993; Petersen et al., 1993b; Gossler and Kind, 1996; Flanagan and Shearer, 1998a; Gu et al., 1998);
- **Precursors to PP**, from which the 410 has been globally observed whereas the 660 was not found (e.g. Estabrook and Kind, 1996; Shearer and Flanagan, 1999);

- **Precursors to P'P' (PKPPKP)**, showing high frequency (~ 1 Hz) reflections of both the 410 and 660, implying that the discontinuities can be as thin as 4 km (e.g. Benz and Vidale, 1993; Stunff et al., 1995). The phase is best observed in a epicentral distance range of 65° to 75° with a caustic occurring near 71° (Benz and Vidale, 1993).

Converted waves: The conversion coefficient depends almost entirely on the jump in velocity and is less sensitive to the change in density (Castle and Creager, 1997). According to the position where the seismic wave interacts with the discontinuity, the studies are grouped into source-side and receiver-side conversions.

- **Source-side conversions:** happened by the reflection or transmission of seismic waves directly above or below the source. The accuracy of the depth estimations of conversions from these data depends largely on the accuracy of earthquake locations.

S-to-P conversion (e.g. Bock and Ha, 1984; Vidale and Benz, 1992; Collier and Helffrich, 1997; Castle and Creager, 1998);

P-to-S conversion (e.g. Faber and Müller, 1984);

- **Receiver-side conversions:** happened when seismic waves, which have propagated through the mantle, travel across any discontinuities beneath a station. A P-to-S converted phase will arrive at the station later than the P wave, whereas a S-to-P converted phase will appear as a precursor to the S wave.

P-to-S conversion (e.g. Vinnik, 1977; Kind and Vinnik, 1988; Stammer et al., 1992b; Yuan et al., 1997; Dueker and Sheehan, 1997, 1998; Shen et al., 1998a,b; Li et al., 1998; Kosarev et al., 1999);

S-to-P conversion (e.g. Bock and Kind, 1991).

Among the different methods, reflection of the SS wave from the underside of discontinuities (SdS) and the P-to-S converted waves beneath the seismic station (Pds, known as receiver function) are the most widely used phases. The P-to-S conversion samples an area of discontinuities beneath the seismic station, therefore the study is restricted mainly to the continental area where seismic stations are available. Its horizontal resolution is usually within several hundred kilometers depending on the wavelength used. Studies of SS-precursors, however, sample the discontinuities in an area of the mid-point between the source and receiver, therefore the observation is globally available. Because most of these SdS studies have been done with long-period data (20 sec), the resolution is relatively low (Fresnel zone is larger than 1000 km).

As mentioned above, the differential arrival times between the SdS and the SS waves as well as between the Pds and the P waves are used to infer depths of the upper mantle discontinu-

ities. The use of an inaccurate velocity model can cause estimation errors by converting times to discontinuity depths. This kind of bias can be mostly removed by considering the differential times between the two discontinuities as a measurement of transition zone thickness, because the affection of velocity variation above the 410 is removed in this way.

Using different seismic methods described above, the 410 and 660 km discontinuities have been observed extensively. Both appear to be global features with several percent increase in compressional and shear wave velocities as well as density and are thus included in almost all upper mantle velocity models.

2.2 The nature of the 410 and 660

Establishing the underlying cause of the upper mantle discontinuities in material properties has been a major effort in the past few decades, and the work continues. Whereas the crust-mantle (Moho) and core-mantle boundaries are accepted as compositional changes (between silicic crust and mafic mantle and between peridotitic mantle and iron-rich core, respectively), the main upper mantle discontinuities at 410 and 660 km depth are more commonly believed to arise from phase changes in mantle mineralogy due to pressure and temperature variations in the Earth's interior (Bernal, 1936; Ringwood, 1975).

Since the 1950s it has been known that the upper and lower mantle are composed dominantly of olivine (about 70%). The common upper mantle mineral such as olivine ($\text{Mg, Fe})_2\text{SiO}_4$ and enstatite ($\text{Mg, Fe})\text{SiO}_3$ undergoes a series of phase transformations with increasing pressure. In particular, the low-pressure olivine crystal converts to the β -spinel structure at pressure and temperatures expected near 410 km depth (137.3 Kba, 1535°C), the β -spinel structure converts to γ -spinel structure near 500 km depth, and then the γ -spinel structure converts to perovskite ($(\text{Mg, Fe})\text{SiO}_3$) and magnesiowüstite ($(\text{Mg, Fe})\text{O}$) at temperature and pressure conditions near 660 km depth (24 GPa, 1600°C) (e.g. Liu, 1979, 1976; Ringwood, 1975). These mineralogical phase transitions compact the crystal lattice and cause an increase in seismic wave velocity and density. Because the phase transformation can occur over a fairly narrow range in depth (proportional to pressure), it is plausible that upper mantle discontinuities may indicate internal phase boundaries of the mantle minerals.

The phase changes can be affected by the ambient temperature condition. The equilibrium depth positions (pressure) of discontinuities will be altered by a temperature anomaly. Their relationship is defined by the "Clapeyron slope" ($\partial P/\partial T$). According to the mineralogical experiments, the olivine to β -spinel phase change expected at 410 km depth occurs with an exothermic Clapeyron slope of about 1.5–2.5 MPa/K (e.g. Akaogi et al., 1989; Katsura and Ito, 1989), while the phase changes at 660 km depth with an endothermic Clapeyron slope of

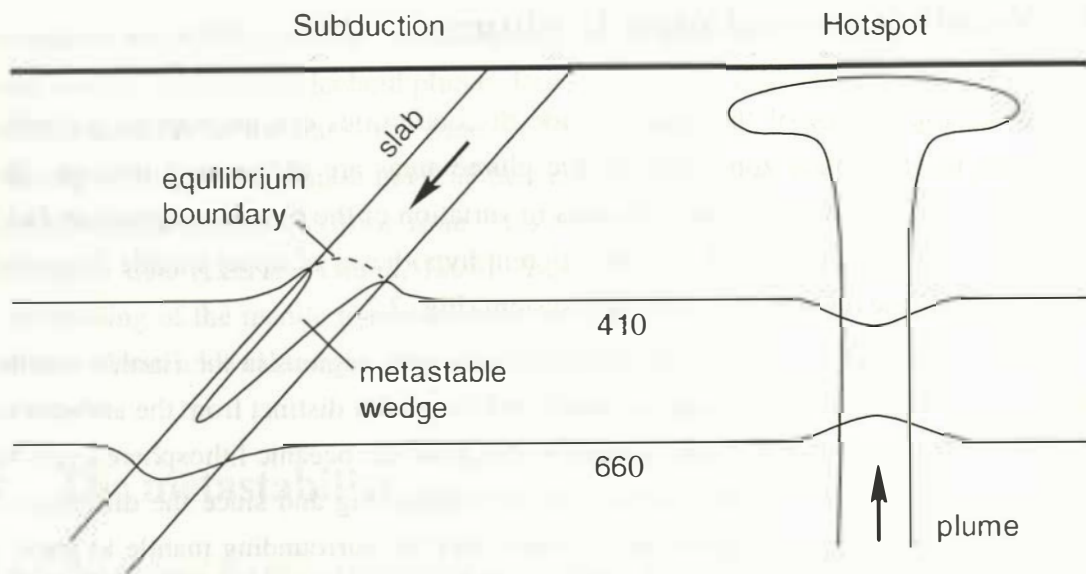


Figure 2.2: Sketch showing the topography of the 410 and 660 caused by temperature anomalies in subduction zones and hotspot areas.

about $-2 \sim -4$ MPa/K (e.g. Ito and Yamada, 1982; Ito et al., 1990). Thus, the olivine to β -spinel (the 410) equilibrium position will be uplifted within a cold mantle environment, and depressed when temperature increases; but the γ -spinel to perovskite and magnesiowüstite (the 660), in contrary, will reach equilibrium at deeper and shallower depth at lower and higher temperatures, respectively (Fig. 2.2). For example, a 15 km elevation of the equilibrium of the 410 predicts a 400°C temperature decrease (e.g. Akaogi et al., 1989). Every 100°C decrease in mantle temperature will cause a 5–10 km increase in 660 depth, hence a 30 km discontinuity topography at 660 km depth observed in subduction zones required a lateral temperature anomaly of 300°C to 600°C in terms of the Clapeyron slope alone (Shearer and Masters, 1992).

According to the exothermic and endothermic nature of the phase boundaries, the topographic variations of the 410 and 660 should be anticorrelated in response to temperature anomalies at the transition zone depths. Such anticorrelation is observed beneath different tectonic regions (Revenaugh and Jordan, 1991a; Gossler and Kind, 1996; Gu et al., 1998). A 5 km thicker transition zone under cratonic areas and 9 km thinner under oceans are concluded to have about $100\text{--}200^\circ\text{C}$ temperature difference (Gossler and Kind, 1996).

The arrival time of a reflected or a converted phase depends on the depth of the discontinuity which is predicted by the thermal property of the discontinuity and the ambient temperature condition. Thus, the study of the 410 and 660 topography is now used as the thermometer of the upper mantle.

2.3 Subduction and mantle plume

Although the topography of the upper mantle discontinuities can be mapped globally, their observations in subduction zones and mantle plume areas are of the most interest. Because these regions represent the extreme scenarios in variation of the mantle temperature field, they can provide the best chance to check the different hypotheses of upper mantle discontinuities and hence to explore the mantle convection system (Fig. 2.2).

Subduction zones are among the most heterogeneous regions in the Earth's mantle. The subducting lithosphere is both compositionally and thermally distinct from the ambient mantle, and results in relatively fast seismic velocities. Because the oceanic lithosphere cools for tens of millions of years at the Earth's surface before subducting and since the diffusion of heat in rock is slow, slabs remain significantly cooler than the surrounding mantle to great depths (McKenzie, 1969; Koper et al., 1998). The thermal structure of a slab depends primarily on the rate of subduction and on the age of the subducting lithosphere (e.g. Molnar et al., 1979) and therefore varies greatly for different subduction zones. For a mature subducting plate, it is assumed that the interior of the plate is 800°C cooler than the surrounding mantle at a depth of 400 km, 400°C cooler at 650 km and attains thermal equilibrium with the surrounding mantle at 900 km (Ringwood and Irifune, 1988). The cool temperatures can alter the stability fields of various minerals, slow the kinetics of the reactions and complicate the $\alpha \rightarrow \beta \rightarrow \gamma$ system.

Studies of short-period near-source conversions have been applied in the subduction zones. The 410 is found to be uplifted by ~15 km (Vidale and Benz, 1992) near the core of several subducting slabs and by 60 km (Collier and Helffrich, 1997) in Izu-Bonin close to and within the slab. In south America, however, Collier (1999) observed no 410 deflection in the region where seismicity is absent between 200 and 600 km depth, and interpreted it as a "warm" slab at intermediate depth. The observed 660 topography is larger than that of the 410. The 660 is depressed by ~25 km near slabs (Vidale and Benz, 1992), in Izu-Bonin by up to 40 km (Collier, 1999) and by ~60 km (Castle and Creager, 1998, 2000). In Tonga the depression of the 660 reaches a value of ~70 km (Bock and Ha, 1984; Niu and Kawakatsu, 1995). Using receiver function technique, Vinnik et al. (1996a) found also a thicker transition zone in the subduction zone beneath Eurasia.

A mantle plume rises from a thermal boundary layer and has a narrow lateral extension in the upper mantle (Nataf, 2000). According to the exothermic nature of the 410 phase transition, it would be deflected downwards in a hot plume, whereas the endothermic 660 phase transition would be deflected upwards with increasing temperature. The lateral extension as well as the magnitude of the 410 and 660 topographic anomalies can provide information on lateral temperature variations, diagnosing the origin depth of mantle plumes (Shen et al., 1998b).

The receiver function study of the Iceland hotspot detected a ~20 km thinner transition

zone (relative to IASP91) within a small region (200 km radius) (Shen et al., 1998b), implying a lower mantle origin of the Iceland plume. Beneath the East Pacific Rise, however, there is no significant anomaly of the transition zone thickness (Shen et al., 1998a), which could suggest that the upwelling of the mantle material beneath the ridge does not associate with an excess temperature in the mantle transition zone. This result is consistent with the study of long-period SS-precursor data (Lee and Grand, 1996). Beneath the Yellowstone hotspot, there is a 20–30 km thinning of the mantle transition zone occurring over 200–300 km lateral scale, which could result from a lateral temperature variation of 250°C (Dueker and Sheehan, 1997).

2.4 The metastability

In subduction zones, the lateral topographic variation of the 410 is controlled by the temperature anomaly across the slab (e.g. Schubert et al., 1975; Helffrich et al., 1989). However, within the central part of a slab, the 410 phase transition could be sufficiently slowed down because of the low temperature. If the phase change is much slower than the motion of a slab, the phase boundary could be depressed within the core of the slab and form a wedge-shaped region of metastable olivine. Such a wedge may persist in the subducted slab to a depth well below 410 km (Fig. 2.2) (e.g. Sung and Burns, 1976a,b; Katsura and Ito, 1989; Bina and Helffrich, 1994; Kirby et al., 1996; Schmeling et al., 1999). Numerical simulations for different thermal models of slabs showed that the metastability should appear in cold and quickly subducted slabs with a width of 20–60 km and extending to a depth of more than 500 km (implied by deep seismicity) (Rubie and Ross, 1984; Kirby et al., 1996; Dässler and Yuen, 1996), but there might be no wedge at all in a slowly subducting slab. The regions of metastable olivine may be heterogeneous with non-planar boundaries between the olivine and spinel phases (Frohlich, 1989).

The existence of metastable olivine has important implications for mantle convection (e.g. Sung and Burns, 1976a). Metastable olivine would create a negative density anomaly, making the 410 phase transition an impediment to subduction rather than an aid, as would be the case if the transition were uplifted to its equilibrium position (Koper et al., 1998). The existence of metastable olivine is also crucial to the transformational faulting hypothesis for the explanation of deep earthquake mechanisms (> 350 km) (e.g. Kirby, 1991; Kirby et al., 1996). This hypothesis explains deep events as the result of the localized transformation of metastable olivine to the higher-density phases along thin zones known as anti-cracks.

Indirect evidence for the existence of metastable olivine, in the form of deep double seismic zones, has been observed in Tonga (Wiens et al., 1993) and Izu-Bonin (Iidaka and Furukawa, 1994). Although other interpretations are possible, such nearly parallel zones of seismicity

are predicted by the transformational faulting hypothesis, because the phase transformations depend mainly on the critical temperature (Sung and Burns, 1976a), thus the phase boundary, where the deep events would occur, should be well approximated by an isotherm.

Direct seismological evidence for the existence of metastable olivine is, however, both sparse and inconclusive. This hypothesis was supported by Iidaka and Suetsugu (1992), who concluded from a study of travel time residuals that metastable α -olivine exists to a depth of at least 550 km in the southwestern Japan subduction zone. However, investigations by Koper et al. (1998) indicate that seismic detection of a metastable olivine wedge may not be possible, and recent analyses (e.g. Silver et al., 1995; Myers et al., 1995; Tibi et al., 1999) suggest that the 1994 deep Bolivia earthquakes may not be compatible with the transformational faulting hypothesis. Tomographic techniques cannot give the necessary resolution of wedges even given an ideal data set and station geometry (Zhao et al., 1997b). One of the reasons is the low resolving power of tomographic methods at this depth, the other is that the hypothetical metastable wedge is a low-velocity feature. As the olivine is far into the fields of high-density phases, the velocity contrast across the phase boundary would decrease with depth (Koper et al., 1998) and the first-arriving seismic energy will be diffracted and refracted.

2.5 Discrepancies

1. Discrepancy between seismic observations and laboratory predictions

Not all of the properties of the upper mantle discontinuities are predicted well by mineralogical experiments.

(1) topography of the discontinuities.

One possible contradiction between the predictions and the seismic observations is the amplitude of the 410 topography. Bina and Helffrich (1994) argued that the expected 410 Clapeyron slope is steeper than that of the 660, thus the 410 topography should be larger than the 660 topography. However, seismological observations with long-period data show that the large-scale topographic variations of the 410 are significantly less than that of the 660 (e.g. Shearer, 1993; Flanagan and Shearer, 1998b). This could be explained as the underestimation of the 410 topography by the long-period data studies, since the estimations by the short-period data in the same areas are significantly larger (e.g. Collier and Helffrich, 1997; Castle and Creager, 1998, 2000). Synthetic seismograms show that the studies of long-period underside reflection phases like PdP and SdS underestimate topography of the discontinuities for the cases of both uplift and depression, but the underestimation of the 410 is larger than that of the 660 (Neele et al., 1997), resulting in smaller 410 uplift observations (e.g. Shearer, 1991; Flanagan and Shearer, 1998a).

(2) sharpness of the discontinuities.

Another contradiction between the seismological observations and mineralogical experiments is the sharpness of the upper mantle discontinuities. Every phase change in the Earth's mantle will lead to a pressure-temperature region where both product and reactant coexist, form a zone of transitional seismic properties interpolating those above and below the phase change (Bina and Wood, 1987). The amplitude of a seismic phase produced by the gradient zone depends on its width and the seismic wavelength. When the width of the gradient zone is thin relative to the wave length (not more than 1/4 wave length), this "discontinuity" is seismically detective.

Since the upper mantle discontinuities have been observed with short-period seismic waves (Benz and Vidale, 1993), they should be seismically sharp. The main frequency range of the short-period signals is about 2 sec which corresponds to a wavelength of 18–20 km in the transition zone depth, therefore the discontinuity should extend 4–5 km vertically. This value is smaller than what is suggested from petrological experimental results and thermodynamic models of the phase transition (Sung, 1979; Bina and Helffrich, 1994). According to the laboratory predictions, the width of the 410 phase transition depends on the ambient temperature conditions; it would be 20 km at 950°C and 10 km at 1750°C (Bina and Helffrich, 1994).

The best observations of a sharp 410 are obtained under the Basin and Range province in the western US and the Indian Ocean (Benz and Vidale, 1993) where the ambient temperatures are probably high. However, the depth observed under the Indian Ocean (420 km, (Shearer, 1993), 410 km, (Benz and Vidale, 1993)) is in disagreement with the prediction of the phase boundary hypothesis, which predicts a depth of at least 435 km for such a sharp boundary. Also, the 35 km width of the 410 transition observed beneath the Russian platform (Priestley et al., 1994) should imply a very low ambient mantle temperature and the depth of the 410 should be significantly shallower than the observed value of 400–435 km. These discrepancies could be related to the uncertainty of the experimental conditions and seismological observations. It is, however, possible to find thermodynamic models yielding narrow transition intervals and thus a sharp 410 prediction (e.g. Helffrich and Wood, 1996; Helffrich, 2000). According to the estimation of the 410 sharpness by Sung (1979), the phase transition will proceed from 10 to 90% completion across a 50°C interval in temperature. In the slab thermal model of Schubert et al. (1975), this corresponds to a thickness of the transition of less than ~7 km.

In contrary to the 410, the 660 sharpness is difficult to estimate by petrological experiments. The olivine phase change at 660 km depth is expected to occur within a few kilometers width (e.g. Ito and Takahashi, 1989). However, another transition for garnet to perovskite which might contribute also to the 660 is expected to occur more smoothly, within a zone about 70 km wide (Ita and Stixrude, 1992). These two transitions may actually occur at slightly different depths and over different depth intervals, so that the 660 may be more complex than a single

gradient or a single discontinuity (e.g. Duffy and Anderson, 1989).

2. Discrepancy among different seismic observations

While Revenaugh and Jordan (1991b), Gossler and Kind (1996) and Gu et al. (1998) concluded an anticorrelation of the 410 and 660, Stammer et al. (1992b) and Stammer and Kind (1992) did not. With the long-period data, the transition zone is found to be thinner under oceans and thicker under continents (Gossler and Kind, 1996; Gu et al., 1998). Lee and Grand (1996) showed that there is no significant difference in the 410 and 660 depths beneath sea floor younger than 10 Ma and those beneath older sea floor. Shearer (1991, 1993) shows that neither transition zone width nor 410 topography appears to have correlation to any surface tectonic features. In the northwest Pacific, the 660 lies deeper but the 410 is neither significantly deeper nor shallower. The variation of the transition zone thickness is dominated by the 660 topography due to its higher amplitude relative to the 410 topography (Shearer, 1991, 1993).

Different seismological methodologies yield different estimates of discontinuity depths (Bock et al., 1995; Chaljub and Tarantola, 1997). Observations with short-period and broadband data show usually larger topography than with long-period data because of the higher resolution power. The long-period studies of mid-path interaction (like precursors to SS) are able to reveal many different types of environments, since their bouncing points distribute more widely around the Earth's surface, but their resolution power is limited because of the large Fresnel zone. With reflected SS waves of 25 sec period, the lateral resolution is limited to about 10° , (e.g. Shearer and Masters, 1992). Chaljub and Tarantola (1997) show that using SS precursors, a 660 uplift is faithfully estimated at length scales larger than 1500 km, while the resolution of a 660 depression is larger than 3000 km. Thus, these long-period phases are ideal to study a large-scale discontinuity structure, for example, the worldwide existence of the 410 and 660 and their topographic differences between continents and oceans (Shearer, 1991; Gossler and Kind, 1996).

However, there are large lateral velocity variations in the mantle. The S velocity, for example, can vary up to 10% in different surface tectonic provinces. The temperature field near subduction slabs is expected to show shorter wavelength variations because of the about 100 km scale length of thermal diffusion of subducted lithosphere. Temperature variations should result in the 410 and 660 depth variations. Up to 50 km topography of the 410 and 660 are observed in the immediate vicinity of subducting slabs over horizontal scales of only a few degrees (e.g. Collier and Helffrich, 1997). Such a feature can not be detected by long-period data described above. The resolution of short-period near-source conversions and of near-receiver conversions are relative high. The spatial topographic resolution of a near-receiver converted phase with 10 sec period is 150 km horizontally and 15 km vertically at a depth of 660 km (van der Lee

et al., 1994). Thus a better resolution of narrow bumps or troughs of the 410 and 660 could be obtained with the study of these converted phases, although the study regions are limited either to the plate boundaries where earthquakes occur or to the areas where seismic stations are deployed. Because the thermal structure of a slab depends both on the rate of subduction and on the age of the subducting lithosphere (e.g. Molnar et al., 1979) and therefore varies greatly for different subduction zones, the topographic observations of the 410 and 660 obtained by short-period near-source conversions show difference in different observation regions.

2.6 Other discontinuity hypotheses

While the olivine phase hypothesis is widely accepted, it has also been challenged by models which argue that small compositional changes may also be present close to or coincident with the depths of the phase changes (e.g. Anderson and Bass, 1986; Duffy and Anderson, 1989; Jeanloz, 1991). For example, a change in bulk chemistry (enrichment in Fe or Si or both) could be added to a phase transition in order to simultaneously satisfy the observed density and seismic velocity jumps (Jeanloz, 1991; Ita and Stixrude, 1992; Stixrude et al., 1992).

Generally the phase transition hypothesis explains well the 410 with the olivine amount in the upper mantle varying from 40% (Duffy and Anderson, 1989; Duffy et al., 1995) to 60% (Irifune, 87; Bina, 93). However, high-pressure experiments in mineral physics have shown that although the velocity jump across the 660 can be explained by the phase change (e.g. Liu, 1976), the chemical changes are still possible occurring at or near 660 km depth, but with small velocity contrast (e.g. Jeanloz, 1991).

The hypotheses of a phase or a compositional change predict different responses of the discontinuity to lateral temperature changes. Heat diffusion in the mantle is at rates comparable to material motion. The discontinuity will adopt its equilibrium position in the mantle, moving up or down either with or against the mass flux direction. If the discontinuity is compositional, the material moving through it will not readily mix with those on the other side of the discontinuity due to the high viscosity. Therefore, the discontinuity will bulge downwards or upwards in the direction of mass flux. In a subduction zone, a compositional change between upper and lower mantle could result in a dynamical displacement of the 660 to several hundred kilometers by impinging slabs (Christensen and Yuen, 1984). However, the thermodynamic properties of a phase change describe an elevation or a depression of the discontinuity depending on the sign and the magnitude of its Clapeyron slope and the maximum topography should be less than several tens of kilometers. The seismological observations of the 660 topography are up to 70 km (e.g. Collier and Helffrich, 1997; Castle and Creager, 1998) and are inconsistent with the large depth variations predicted by compositional changes.

The properties of the 660 is important for understanding the mantle convection systems. A compositional change near 660 km depth will separate the mantle into two convection regimes, the slabs encounter resistance near 660 km which prevents the penetration. A mineral phase change at the 660 implies a whole-mantle convection model. Downgoing slabs in subduction zones could penetrate through the 660 into the lower mantle because the impedance of the phase boundary is small. Even in the case that there is a large density increase occurring at 660 km depth impeding the penetration of slabs (Christensen and Yuen, 1984), the buoyancy loads in the upper mantle supported by the lower mantle should yield a large 660 deflection. However, since the observed 660's topography was not large enough to support the inferred buoyancy loads, the whole-mantle convection model is still preferable (Morgan and Shearer, 1993).

2.7 Other discontinuities in the upper mantle

A discontinuity near 220 km depth has been proposed to be caused by a compositional change between garnet lherzolite and eclogite (Anderson, 1979) and the existence of an anisotropic layer caused by preferred alignment of olivine crystals (Leven et al., 1981). But a significant 220 appears not to be a general feature of any tectonic region. Although in some areas there is strong evidence for a structure near this depth (Hales et al., 1980; Drummond et al., 1982; Leven et al., 1981), it is absent in many cases (e.g. Shearer, 1991; Walck, 1984; Grand and Helmberger, 1984), indicating that the impedance contrast at 220 km must be less than that of the PREM model. Another possibility is that its depth is too variable to form coherent reflections.

The observations of the 520 are debatable: whereas Gossler and Kind (1996) and Gu et al. (1998) noticed that it is a regional appearance, Shearer (1990), Shearer (1991), Shearer (1993), Shearer and Masters (1992) and Shearer (1996) claim that this discontinuity is a global feature with a relative large density but small velocity increase. Bock (1994) noticed that it is possible to misidentify sidelobes between the 410 and 660 phases in the long-period data as signals from a discontinuity at 520 km depth.

Below the 660, discontinuities have been reported at depths of 720 km (Revenaugh and Jordan, 1991b), 920 km (Kawakatsu and Niu, 1994) and 1200 km (Stunff et al., 1995). The existence of these deep discontinuities would support the compositional transition hypothesis of the upper mantle discontinuities.

Chapter 3

Receiver Function Method

Receiver function analysis has been, for more than 30 years, a useful method to obtain the crustal and uppermost mantle velocity structure (e.g. Phinney, 1964; Burdick and Langston, 1977; Langston, 1977a, 1979, 1981; Owens et al., 1984; Owens and Zandt, 1985; Owens et al., 1987; Ammon et al., 1990), and to identify upper mantle discontinuities (Vinnik, 1977; Kind and Vinnik, 1988; Stammer et al., 1992b) underneath a 3-component seismic station. In the past few years, the conventional receiver function method, which is suitable for separately distributed seismic stations, has been successfully extended to applications to portable station arrays (Dueker and Sheehan, 1997, 1998; Yuan et al., 1997; Jones and Phinney, 1998; Li and Nábělek, 1999; Kosarev et al., 1999; Ryberg and Weber, 2000). In these studies, some data processing techniques which are routinely used in the multi-channel reflection seismology are successfully applied to the earthquake data recorded by seismic arrays, producing detailed images of conversion boundaries in the crust and the upper mantle.

Teleseismic P waves which are incident upon a seismic discontinuity below a station will produce P-to-SV conversions at the discontinuity. In a ray coordinate system at the station (L-, Q- and T-component, see Fig. 3.1), the amplitudes of the converted SV wave dominate the Q-component, while the energy of the direct P waves concentrates on the L-component. Theoretically there is no energy on the T-component for a laterally homogeneous and isotropically layered medium. By deconvolving the signal of the L-component from the other components, the effects of source and ray path of the incident P wave are removed. The deconvolved Q- and T-components are called receiver functions. Receiver functions provide a wealth of information on the Earth's interior within the crust and upper mantle. Such information is carried by the converted waves.

As shown in Fig. 3.1, a small part of teleseismic P wave energy converts to SV energy (P_s) on a discontinuity. Usually there are also multiple conversions appearing on the Q-component which have the amplitude comparable to the P_s phase. Two types of multiple phases are shown

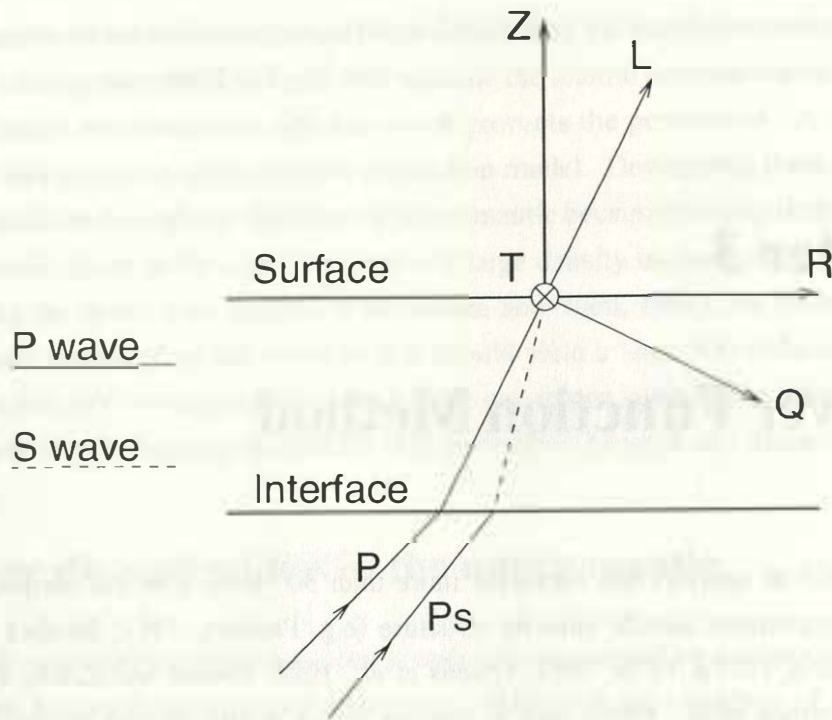


Figure 3.1: Sketch showing a teleseismic P wave propagating through the mantle and converting to an S wave at the interface beneath the station.

in Fig. 3.2a (Pps and Pss), which have additional reflections between the discontinuity and Earth's surface. Fig. 3.2b shows a simplified Q-component receiver function trace corresponding to the model in Fig. 3.2a. With the definition of the ray coordinate system used in this study and for a discontinuity with a downward velocity increase, the directly converted phase Ps has positive polarity, while the amplitudes of multiple phases Pps and Pss are positive and negative, respectively.

Delay times are defined as the differential travel times between each converted phase and the direct P wave, i.e. $t_{Ps} - t_P$, $t_{Pps} - t_P$ and $t_{Pss} - t_P$, respectively. They depend on the conversion depth and the P and S wave velocities above the discontinuity. For the IASP91 model (Kennett

Table 3.1: Timings of conversion phases of the IASP91 model (incident P wave has a epicentral distance of 67°).

Code	depth (km)	Ps (sec)	Pps (sec)	Pss (sec)
Moho	35	4.4	15.1	19
410	410	44.1	132.2	176
660	660	68.1	196.5	265

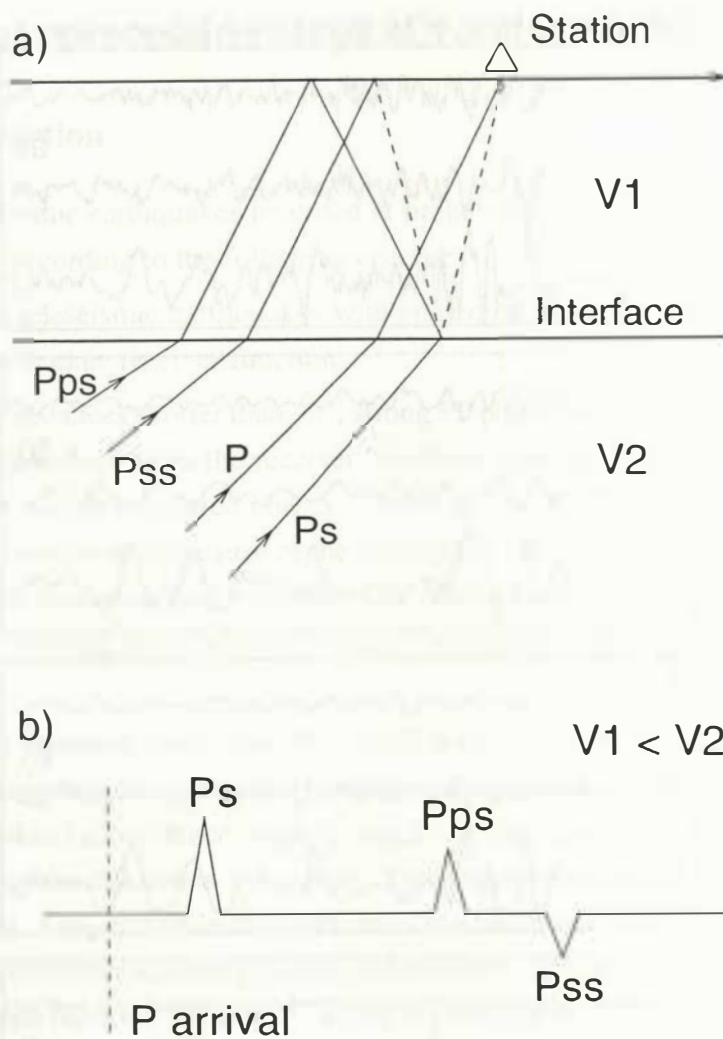


Figure 3.2: a) Diagram showing the major P-to-S converted phases for a layer over a half-space model. b) Simplified Q-component receiver function corresponding to the model in a).

and Engdahl, 1991), the delay times of P-to-S conversions and some multiple phases at main discontinuities are listed in Table 3.1.

Generally, most of the studies are focused on directly converted phase Ps, because the multiple reverberations are usually less coherent due to their longer ray paths and increased timing sensitivity to dipping interfaces (see Cassidy, 1992). Also the multiples from a deep discontinuity sometimes interfere with PP phases.

The basic processing steps for calculating receiver functions include selection of the earthquake records; restoring ground displacement; rotation into ray coordinate system; deconvolution of source and path effects. These steps are illustrated in Fig. 3.3 with the help of a data example recorded at the broadband station BJI. In the following sections the processing

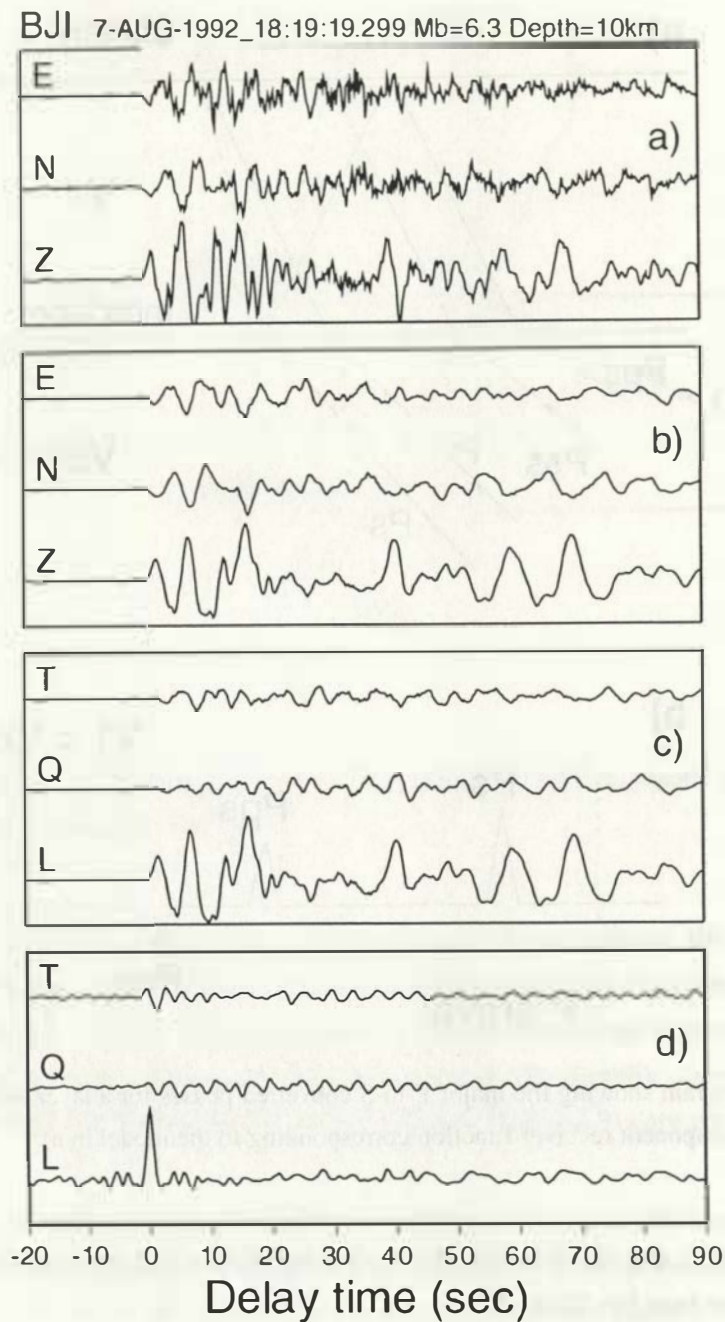


Figure 3.3: Example of receiver function processing with data from the station BJI. a) An original teleseismic record; b) Restitution (optional); c) Rotation; d) Deconvolution.

steps will be introduced in detail. Data examples completing the introduction are records at the broadband station HIA. The locations of the two permanent stations BJI and HIA are found in Fig. 4.2 and Table 4.2.

3.1 Principle processing steps of receiver functions

3.1.1 Data selection

In this study, teleseismic earthquakes recorded at broadband three-component seismic stations have been selected according to the following criteria:

1. Records of teleseismic earthquakes with epicentral distances ranging from 30° to 95° have been used to calculate receiver functions.

For epicentral distances shorter than 30° , strong PP phase arrives in the useful time window and can not be deconvolved from the receiver functions (see Fig. 3.11). It will strongly interfere with the upper mantle converted phases. Moreover, the P wave records for this epicentral distance range are complicated because of the triplication phenomenon due to the upper mantle discontinuities. The deconvolution procedure can rule out much of these complication effects but not all. The remaining non-conversion energy will cause mis-identification of conversion interfaces.

For epicentral distances larger than 95° , the P waves are very weak. With increasing distance, the P wave becomes core-mantle boundary diffraction (P_{diff}) and is even weaker. Another argument is that the incidence angle is small for large epicentral distance, and therefore the P-to-S conversion coefficient is very small. This can be seen in Fig. 3.4, in which the conversion coefficients of upper mantle discontinuities at 410 km and 660 km depth for the IASP91 model have been calculated according to Aki and Richards (1980). In Fig. 3.4, the useful range of epicentral distance between 30° and 95° is highlighted for the 410 and the 660. In this range, the amplitudes of P410s and P660s are between 2-5% of that of the incident P wave and they decrease with the increasing epicentral distance.

2. Only clear records of P waves with relatively high signal-to-noise ratio have been selected. For most stations which have been operated for many years, a large amount of high quality earthquake data are available. Earthquakes with magnitude (Mb) larger than 5.7 have been selected. Since the operation periods of a few new FREESIA (Japanese network) stations are much shorter, for these stations I changed the magnitude criterion to 5.5 in order to include those weak but relatively well recorded earthquakes.

3. Earthquakes within all depth ranges were used. Focal depth was not considered as a factor in data selection.

- (1) Receiver function processing (mainly rotation and deconvolution) can remove most depth phase energy from the Q- and T-components. To show this effect, several earthquake records at station HIA containing significant depth phases are selected. Fig. 3.5a shows 7 original Z-component records of events with focal depths ranging from 80–240 km. Each trace shows a clear depth phase pP. After careful rotation with angles calculated for the incident

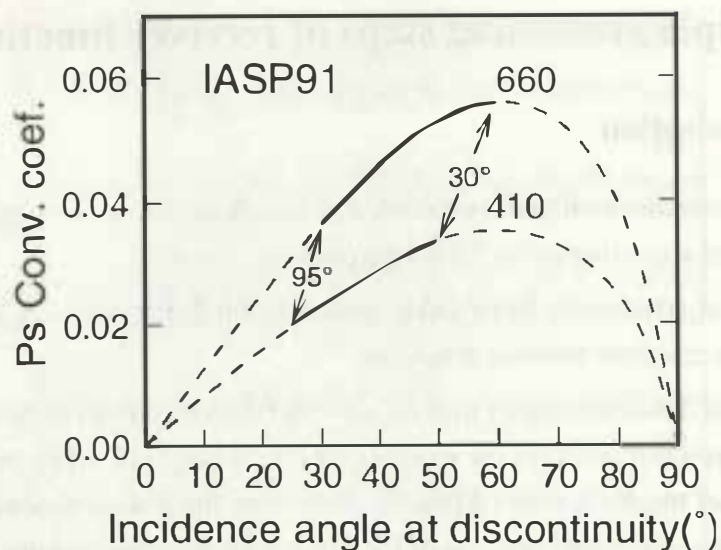


Figure 3.4: Ps conversion coefficient as function of incident angle. The values associated with epicentral distances of 30° and 95° at the 410 and 660 are indicated by symbols “30°” and “95°”.

direct P wave, however, the depth phases almost disappear from their receiver functions of the Q-component (Fig. 3.5b). This could be expected since the pP and sP phases have almost the same ray paths and slownesses as the direct P waves of teleseismic events.

(2) The receiver function technique isolates conversion phases through diverse stacking or coherently displaying techniques of a large amount of data. After a moveout correction of receiver functions according to their ray parameters, the corresponding conversion phases will be coherently enhanced, whereas the depth phase energy will be reduced because of the random distribution of the focal depths.

3.1.2 Restitution

The seismic stations used in this study are composed of broadband seismometers of STS-1, STS-2, and Guralp-3T, except the PASSCAL experiment XL94–95, which deployed 3 short-period stations of 1-Hz Mark-L4 in North Korea. Normally, instead of original ground velocity records, ground displacement is used to calculate receiver functions. Using ground displacement can, in many cases, broaden the response of short-period instruments into a more useful teleseismic frequency range. It also permits the comparison of seismograms recorded by different seismometers possible. Usually restitution filters, which are constructed according to seismometer parameters (natural frequency and damping factor) are used to remove the instrument response. For broadband stations, the restitution of different kinds of seismometers can be substituted by direct integration of the raw records, and in this way the data processing can

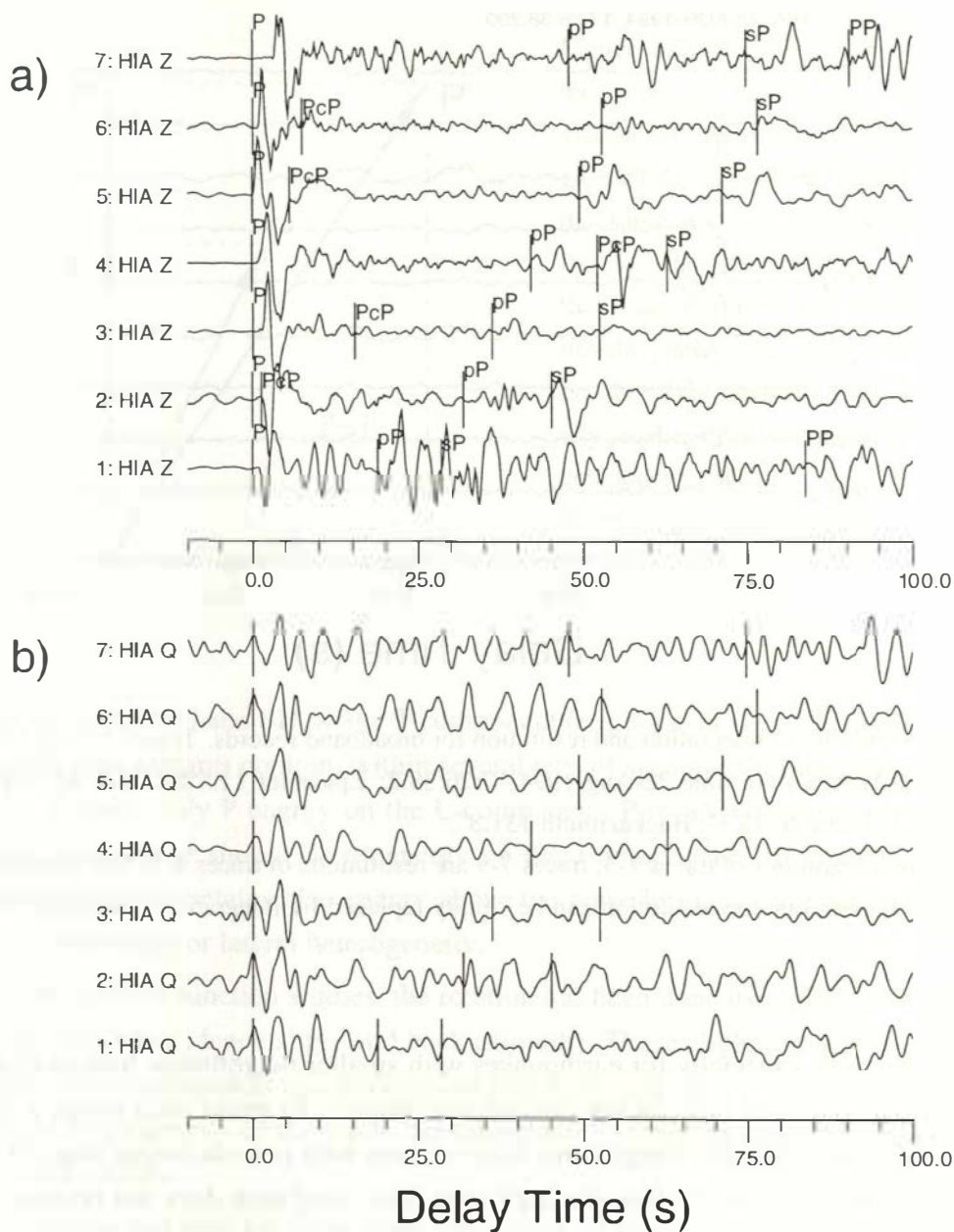


Figure 3.5: a) Original Z-component records at HIA showing strong depth phases; b) After rotation and deconvolution in Q-component, the depth phases disappear because of their similar slowness to the P wave slowness. The P arrival and the expected depth phases on each trace are marked by bars.

be simplified. In Fig. 3.6, traces 1-3 are original earthquake records of ground velocity of Z-, N- and E-components at the station HIA recorded with STS-1 seismometer, traces 4-6 are their simple integrations and traces 7-9 are their restitutions. The effects of the integration are identical to that of the restitution. Thus, the integration are used in this work instead of restitution, except for the short-period stations in North Korea.

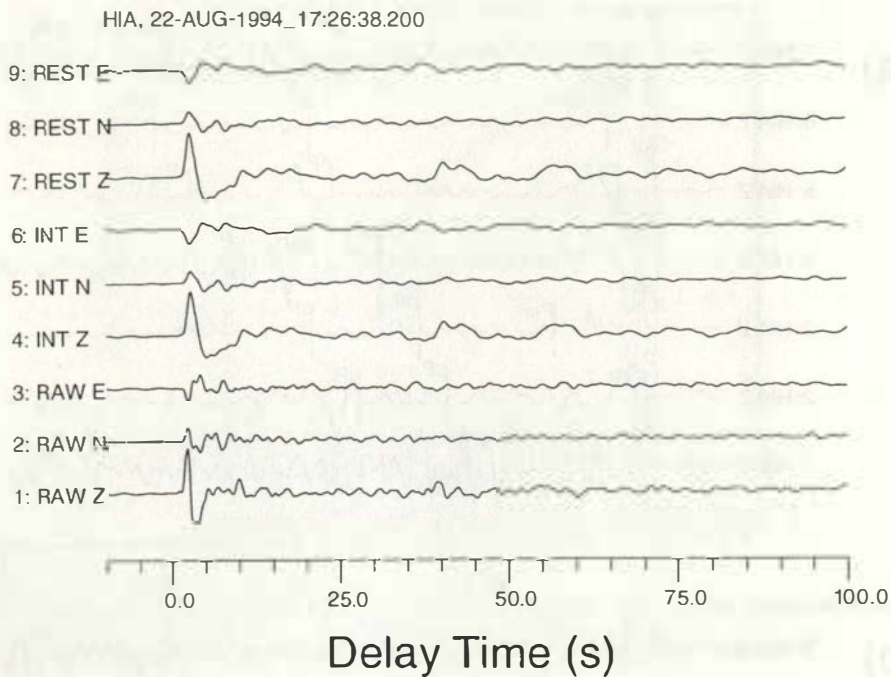


Figure 3.6: Similarity of integration and restitution for broadband records. Traces 1-3 are 3-components raw records at HIA. Origin time 22-Aug-1994-17:26:38.2; Epicenter 11.5°S, 166.4°E; Depth 148 km; Magnitude 6.1; Distance 73.3°; Backazimuth 131.8°.

Traces 4-6 are integrations of traces 1-3; traces 7-9 are restitutions of traces 1-3. The similarity of traces 4-6 and 7-9 suggests that the restitution can be simply replaced by integration in the case of broadband records.

In some cases, especially for earthquakes with smaller magnitudes, long-period noise occurs after the integration (also in the case of restitution). To avoid such noise, a 30 sec high pass filter is applied after the integration. Since signals with periods longer than 30 sec are not useful in receiver function studies, the high pass filter used here does not remove any useful information.

3.1.3 Rotation

The Z-, N- and E-components of the displacement seismograms are rotated into the ray coordinate (L, Q, T), in which the L-component is in the direction of the direct P phase, the Q-component is parallel to the SV wave and points positively away from the source, whereas the T-component is the third component in the right-hand coordinate system of the L- and Q-axes, parallel to the SH direction (see Fig. 3.1).

In a horizontally layered, isotropic medium, P energy is mainly seen on the L-component,

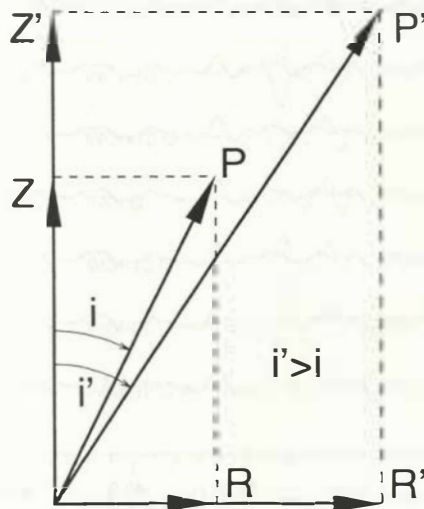


Figure 3.7: Possible error of the incidence angle. The deviation of the incidence angle can be caused by adding the same noise level to both the R- and Z-amplitudes of the direct P wave. For upper mantle phases, the amplitude on the R-component is usually smaller than that on the Z-component, which will result in over-estimated incidence angles ($i' > i$).

SV on the Q-component and SH on the T-component (e.g. Kind et al., 1995; Yuan et al., 1997). Theoretically seismograms contain, within several tens of seconds after the arrival of the direct teleseismic P wave, only P energy on the L-component, P-to-SV converted energy on the Q-component, while there should be no energy on the T-component. In practice, however, the T-component usually contains also energy above the noise level, which is an indication of the presence of anisotropy or lateral heterogeneity.

In many receiver function studies, the rotation has been done using the angles of the theoretical P incidence (incidence angle and back azimuth). These angles are calculated according to the locations of earthquakes and stations and based on a 1-D earth's velocity model. Because of the lateral heterogeneity of the earth, the theoretical P incidence sometimes deviates largely from its real direction.

The rotation can also be done using the angles of observed incidence of P waves. By calculating the eigenvalues of the co-variance matrix from the three-component earthquake P wave records, these angles can be conveniently obtained (Stammler et al., 1992b). There are, however, sources of errors in the calculation of angles. Background noise, for example, may in some cases bring errors to the determination of both incidence angle and back-azimuth. As shown in Fig. 3.7, for a near vertically incident teleseismic P wave, the incidence angle may be over-estimated if the same noise level has been added to each component. Similarly, errors may also occur in the back-azimuth estimations.

In order to test the effect of errors in the rotation angles, receiver functions of both Q- and T-components have been calculated with rotations by a series of different back-azimuths (Fig. 3.8) and incidence angles (Fig. 3.9), ranging from 30° smaller to 30° larger than the theoretical

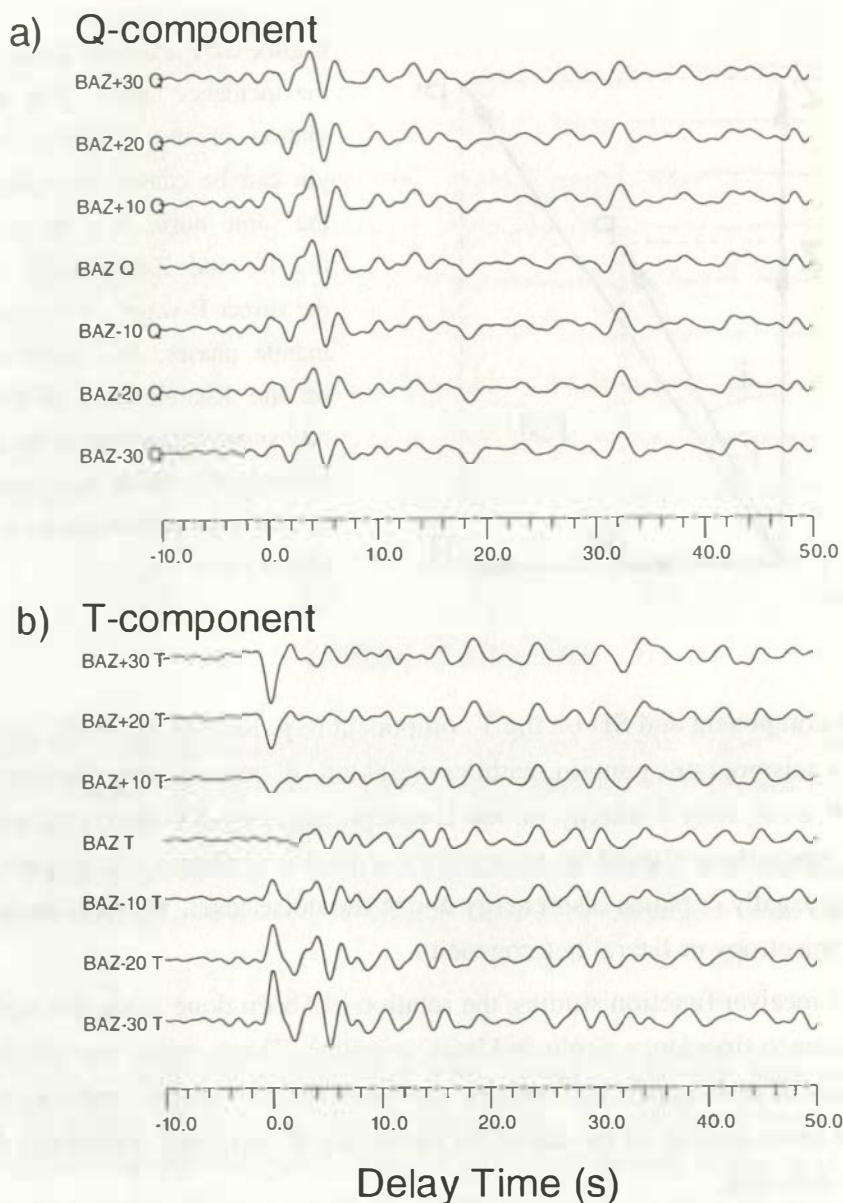


Figure 3.8: Rotation with back azimuth deviations of -30° to 30° from the theoretical values. The original earthquake records are shown in Fig. 3.6 (traces 1-3).

a) Q receiver functions show little difference in waveform; b) Significant waveform differences (polarity inversion) within the first several seconds in T receiver functions are observed. The amplitudes of the T-components are magnified by a factor of 2.

values. A 3-components earthquake record at the station HIA (traces 1-3 in Fig. 3.6) is used in the experiments. The resulting receiver functions generally do not show significant differences, except for the waveforms in the first several seconds. Errors in the back-azimuth do not affect the Q-component (Fig. 3.8a) and errors in the incidence angle do not affect the T-component

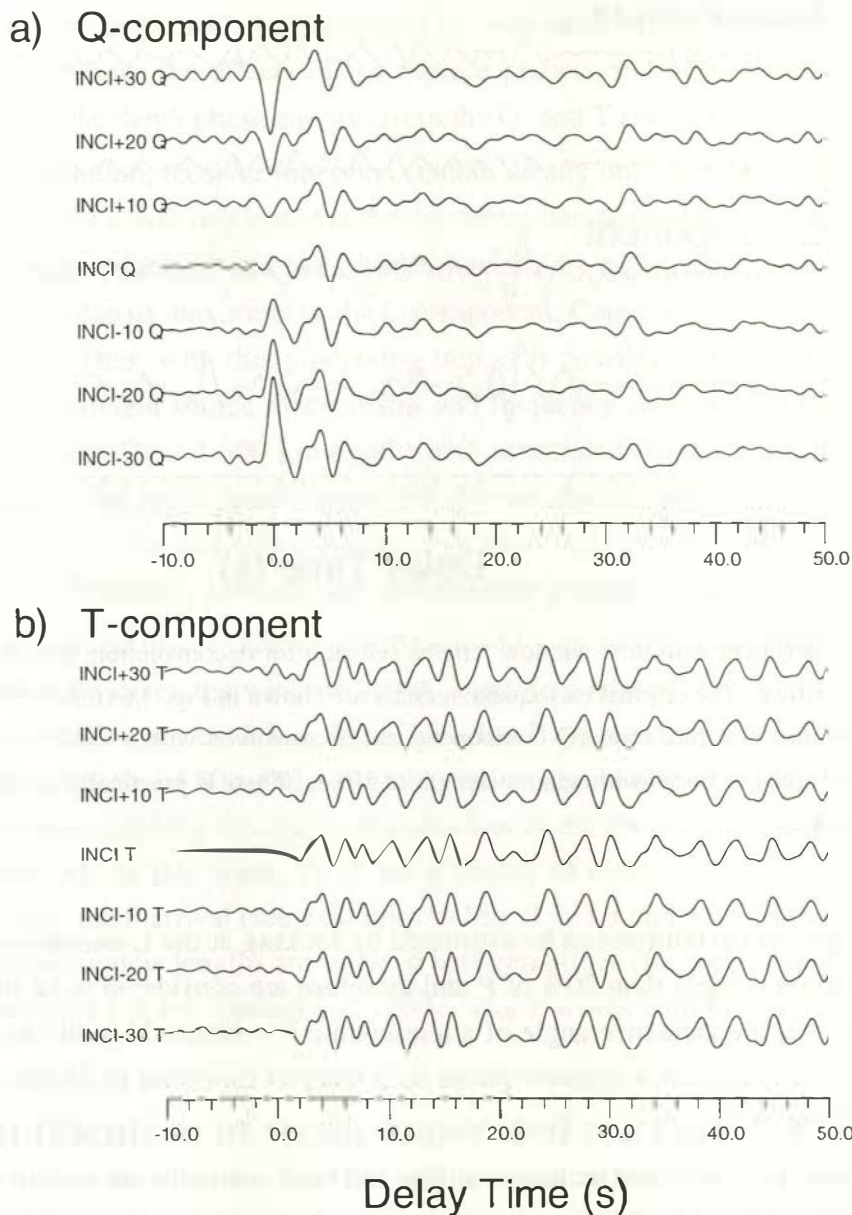


Figure 3.9: Rotation with incident angle deviations of -30° to 30° from the theoretical values. The original earthquake records are shown in Fig. 3.6 (traces 1-3).

a) Q receiver functions show waveform differences (polarity inversion) within the first several seconds; b) There is no significant waveform difference in T receiver functions. The amplitudes of the T-components are magnified by a factor of 3.

(Fig. 3.9b).

Frequently we can see in the receiver function data a phase with negative amplitudes at or just prior to the zero time. Such a phase is not a “side lobe” caused by deconvolution. The

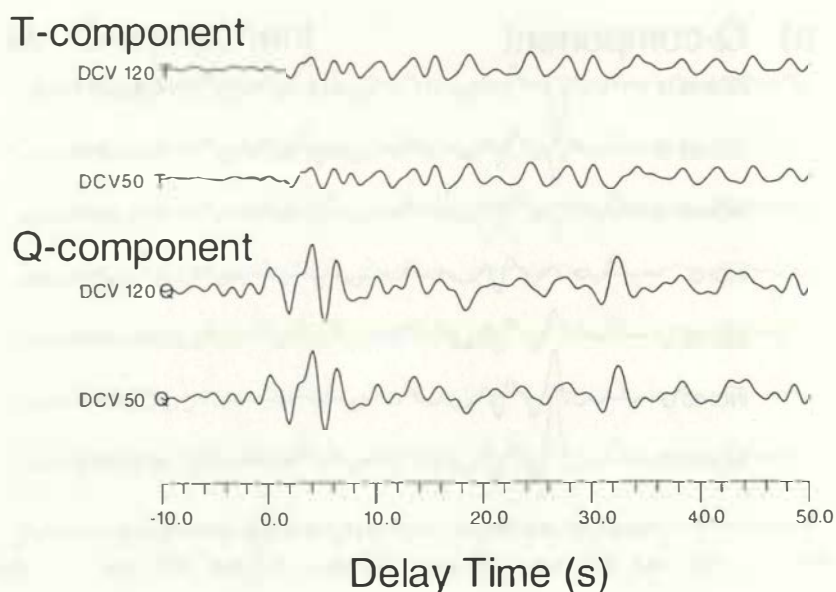


Figure 3.10: Experiment with time window lengths selected for deconvolution, showing that the selection is not very critical. The original earthquake records are shown in Fig. 3.6 (traces 1-3). The first trace (T receiver function) and third trace (Q-component) are deconvolved with a window length of 120 sec, while the second and 4-th traces with window length of 50 sec. There is practically no difference between the associated traces.

side lobes of the deconvolution can be estimated by looking at the L-components; e.g. in Fig. 3.3d the side lobes are less than 20% of P and therefore are considered to be insignificant. As shown in Fig. 3.7, the incidence angle of a teleseismic P wave could easily be over-estimated and, after the rotation, cause a negative phase in Q receiver functions as illustrated in the upper three traces of Fig. 3.9a.

In this study, the calculated incidence angles and back-azimuths are used to rotate the ZNE-component data to obtain the LQT-components and only the Q-component is used to image the upper mantle structures. From the experiments above it is clear that errors of rotation angles are not crucial for the upper mantle converted waves. However, to avoid possible errors, both the “theoretical angles” and the “calculated angles” of the P incidence are calculated, and when the deviation of the angles is larger than 20° , the data are not used.

3.1.4 Deconvolution

A critical processing step to calculate source-equalized receiver functions is deconvolution, i.e. to deconvolve the L-component from Q- and T-component seismograms. This process is justified by the assumption that the L-component contains the source and near-source ray path

effects and it is not significantly contaminated by near-receiver structure. The deconvolution process can thus remove the effects of the rupture process and near-source structure effects (including most of the depth phase energy) from the Q- and T-component seismograms.

After deconvolution, receiver functions contain ideally only the conversions of direct and multiply reverberated waves originated at the discontinuities beneath the recording station. Differences in the source duration and magnitude of events are equalized, all components of each event are normalized to its maximum of the L-component. Conversion amplitudes are preserved by this procedure. Thus, with this processing step, it is possible to incorporate data from (1) earthquakes with different source mechanisms and frequency contents; (2) intermediate-depth earthquakes (between 50 and 300 km depth) with associated depth phases that arrive within the time window of the upper mantle converted arrivals, and (3) earthquakes with complicated source-time functions. The last item is particularly important since these events have often large magnitudes, a rich frequency content, and consequently greater signal-to-noise ratios.

The deconvolution time window must be long enough so that most energy of the direct P wave is included. However, the window length is not very critical. For the earthquake records shown for station HIA (traces 1-3 in Fig. 3.6), the P wave coda is less than 20 sec. Two different window lengths of 50 s and 120 s are used to deconvolve the receiver functions (Fig. 3.10). Both windows are long enough to include most of the P wave energy, the resulting traces are almost identical. In this work, the P wave energy of most earthquake records is limited within 50 sec after the P arrival (see examples in Fig. 3.3, 3.5 and 3.6). In the data processing, the deconvolution window lengths are selected between 80 sec (for records with high frequency and short duration of P wave signals) and 120 sec (for P waves with long duration).

3.2 Amplification of weak converted energy

3.2.1 Stacking method

The amplitudes of upper mantle conversions depend mainly on the velocity contrast of the discontinuities and are usually small. For the IASP91 model, the amplitude ratios of P410s and P660s to P are smaller than 6%, since the velocity contrasts of 410 and 660 km discontinuities are less than 5% (Fig. 3.4). Stacking receiver functions of different earthquakes from one station can help to suppress the random background noise and enhance the coherent conversion signals.

A variety of stacking methods have been employed to improve the signal-to-noise ratio and extract converted waves. The delay time of a P-to-S converted wave relative to the originating P wave is a function of the P wave slowness and hence the epicentral distance. This dependence

(often called moveout) is small for shallow conversion depths at the Moho or intra-crustal interfaces but large for upper mantle conversions. Therefore different strategies are used for crustal and upper mantle studies. For individual stations, the crustal structure can be obtained by direct stacks of receiver functions (e.g. Owens et al., 1984) because of the small moveout of the phases. More exactly, receiver functions can be grouped by similar ray parameters or back azimuths and stacked directly within each group (e.g. Searcy et al., 1996). However, for the study of upper mantle conversions, where delay times vary significantly with epicentral distances, more sophisticated methods are needed. Paulssen (1988) has used a variant of $\tau - p$ stack, in which p is the differential slowness of the conversion with respect to the direct wave, τ is the vertical delay time after the direct arrival. Vinnik (1977), Kind and Vinnik (1988) and Stammer et al. (1992b) suggested a practically similar approach, which accounts, however, better for the expected moveout characteristics of the Ps conversions in a typical upper mantle model. This method is called “delay-and-sum” method and is in fact a sum of receiver function amplitudes along the corrected moveout curve. Stacking is made for a trial value of conversion depth and this process is repeated for all supposed conversion depths varying throughout the whole upper mantle. The depth interval can be taken as 20 km, for example, which is thought to be exact enough. Finally, the phases with conversion characters (with a fixed moveout) are enhanced by their coherent stacking in the summation, meanwhile, other phases with different moveout (multiples, scatters, etc.) and also the random noise are suppressed. In this way, the conversions from the upper mantle can be observed more easily in the summed receiver functions. These stacks spatially average any 410 and 660 topography within an annulus between 150 and 250 km and between 300 and 500 km in diameter, respectively.

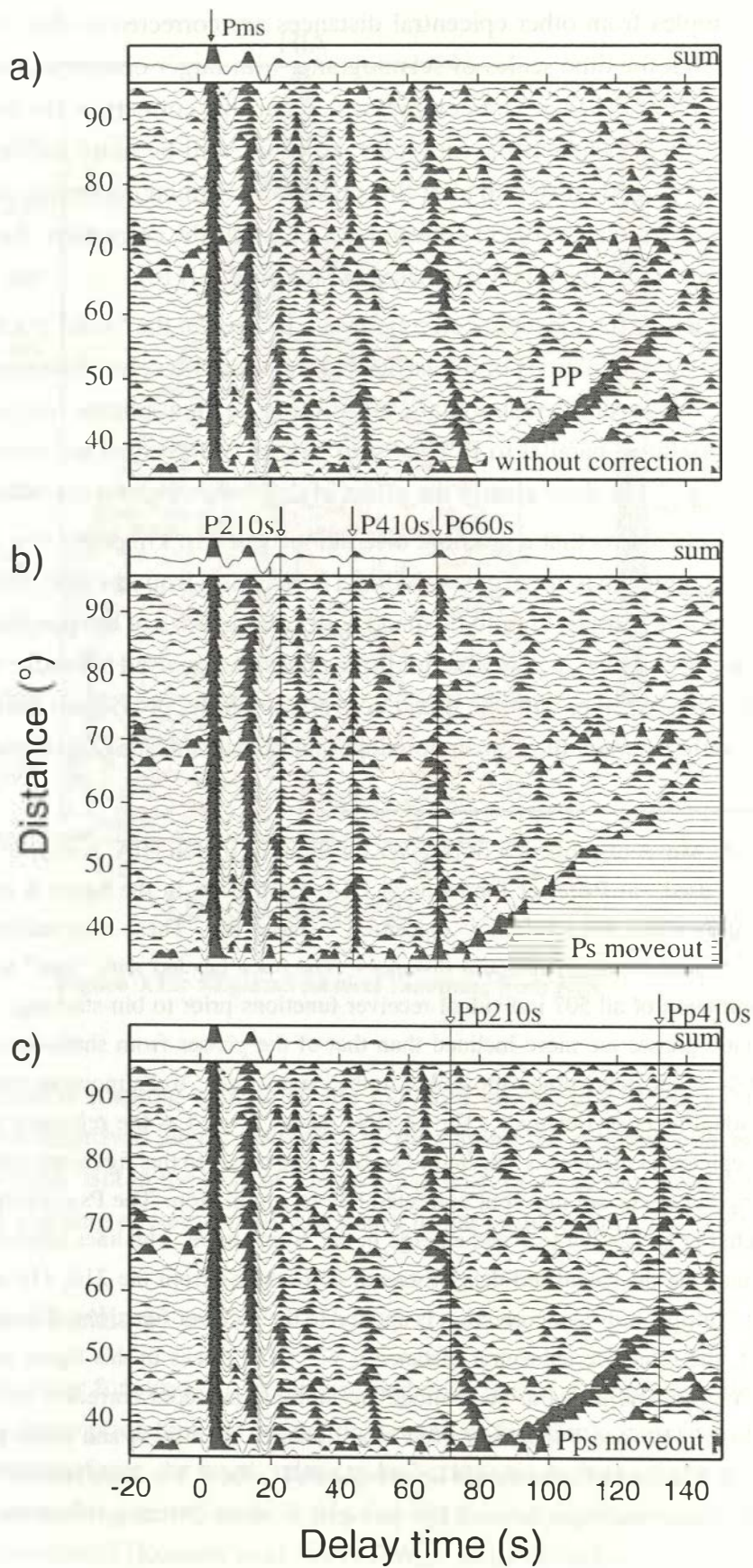
With almost the same idea, Gurrola et al. (1994) suggested a “velocity spectrum stack”, in which a series of the receiver functions are stacked after the moveout correction for a supposed velocity structure. By searching for a perfect stacking point with the largest stacking energy, they could obtain the most suitable velocity model for the structure below a station.

3.2.2 Moveout correction

If the receiver functions are aligned along the P arrivals and sorted according to their epicentral distances, the converted phases originating at different depths have different moveout slopes which are not parallel to P (Fig. 3.11a). For a deeper conversion depth, the moveout slope is larger. Multiples, however, show different behavior, i.e., while the delay time of a Ps converted wave decreases with increasing epicentral distance, the time of a multiple increases.

To compare directly the timing of phases at individual receiver functions, these moveout differences have to be corrected. A slowness of 6.4 sec° is selected as a reference, which corresponding to an epicentral distance of about 67° in the IASP91 model. The times of receiver

HIA



function samples from other epicentral distances are corrected to that of the reference trace. This means that the time scales of seismograms with larger epicentral distances are stretched, while with shorter distances are compressed. After this correction, the conversion phases will be parallel to the P whereas the multiples, however, will be more inclined (Fig. 3.11b). The waveforms are slightly distorted after this procedure. Similar correction can also be applied for multiple phases instead of direct conversions, i.e. after the correction, the multiple phases will be parallel to P while the direct Ps phases are not (Fig. 3.11c).

The effects of the moveout corrections can be seen in the “sum” traces in Fig. 3.11. These traces are direct summations of all associated individual receiver functions. In Fig. 3.11a, the “sum” trace shows only crust signals, since these shallow phases have a small moveout and therefore are almost parallel to P. The “sum” traces of the corrected receiver functions in Fig. 3.11b and Fig. 3.11c show clearly the effect of different moveout corrections.

Fig. 3.11c shows that a possible discontinuity at 210 km depth (the 210) produces a multiple Pp210s which may interfere with direct conversion from the 660 (P660s). In this case, the receiver function analysis should be made with care because of the possible misidentification of the Ps phase. Moreover, a plausible multiple phase can be used to certify the existence of a discontinuity, and, together with the direct conversion phase, provide an estimation of the average Poisson’s ratio between the conversion depth and Earth surface (Zandt and Ammon, 1995).

Figure 3.11: Moveout correction of receiver functions at station H1A. A total of 507 individual receiver functions is used. a) Receiver functions at H1A. Each trace in the figure is the direct summation of original receiver functions within 1° epicentral distance bin. These summed traces are then displayed according to their average epicentral distances. The trace labeled with “sum” at top of the figure is the direct summation of all 507 individual receiver functions prior to bin-stacking. The moveout curves of upper mantle phases are more inclined than that of the phases from shallower depth. Therefore, only signals at 0–20 sec delay times are visible in the “sum” trace. b) Ps moveout correction is applied to all 507 individual receiver functions. The IASP91 model is used as the reference velocity model, and the reference epicentral distance is selected to be 67° . The traces in this figure are obtained similarly as in a), but the original traces are moveout corrected before summation. The Ps conversions from 410 and 660 are corrected to be parallel to P and emerge in the “sum” trace. The lines labeled “P210s”, “P410s” and “P660s” indicate the calculated delay times of conversions from the 210, 410 and 660 for the IASP91 model. c) Multiple moveout correction is applied to the receiver functions. The reference velocity model is IASP91, the reference epicentral distance is 67° . The traces in this figure are obtained similarly as in a), but the original traces to be summed are multiple moveout corrected receiver functions. The Ps conversions (P410s and P660s) are even more inclined than in a) and consequently disappear in the “sum” trace. But the multiples should be now parallel to the P. The lines labeled “Pp210s” and “Pp410s” indicate the calculated delay times of Pps multiples from the 210 and 410 for the IASP91 model.

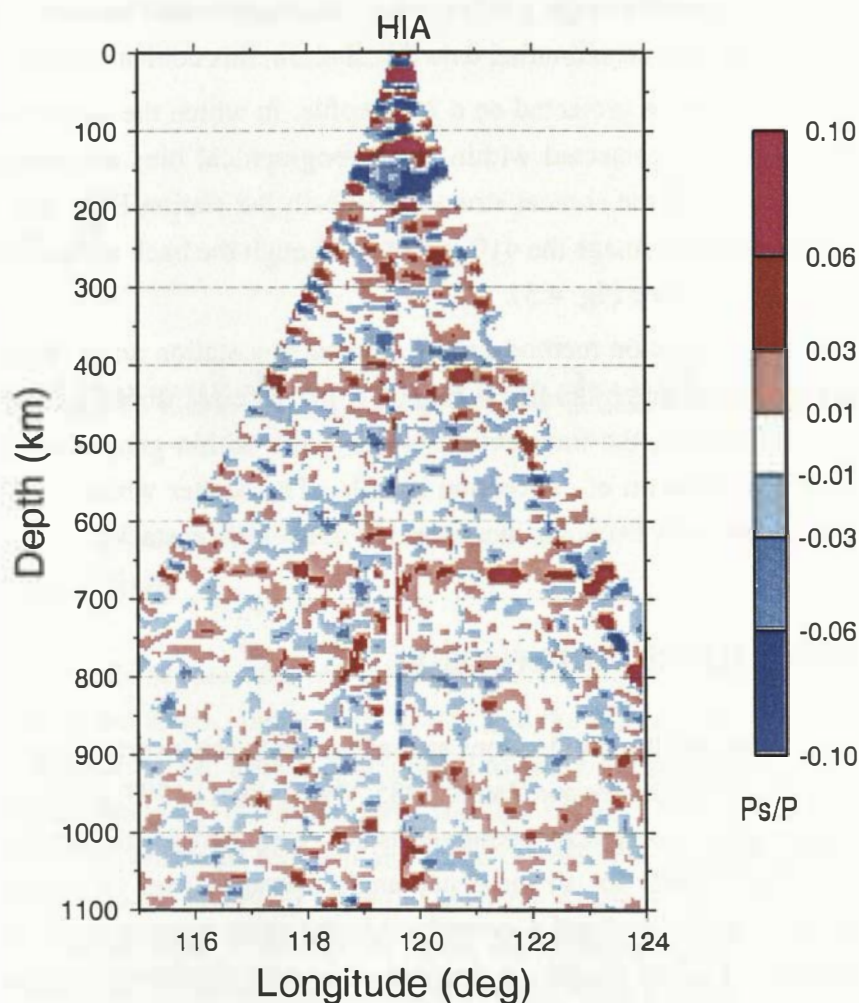


Figure 3.12: Migrated receiver functions from HIA

Relative to previous stacking technique, the moveout corrections of individual receiver functions can provide improved lateral resolution by displaying the coherent conversion phase on each conversion point. But in the case of a large noise level or short wave length topography of a discontinuity, a stacking strategy is still necessary to get reliable and stable signals.

3.2.3 Migration method

The ray path of a receiver function can be determined with use of a reference velocity model (IASP91). With the assumption that the energy on a receiver function comes from P-to-S converted wave at planar interfaces, the amplitudes can be back-projected onto the spatial locations of the conversion points along the ray path. In this way the S wave impedance contrast along the ray path can be reconstructed (Kosarev et al., 1999). With an ideal back azimuth distribution of

receiver functions, it is possible to get a 3-D conical structural model beneath a station. But in real case, because of the uneven azimuthal data distribution, this conical model is fragmentary.

Such a 3-D image can be projected on a 2-D profile, in which the amplitudes of different migrated receiver functions projected within same geographical bins are stacked. Fig. 3.12 shows an E-W projection of the conical structure beneath the station HIA. The receiver functions from this station clearly image the 410 and 660 although the back azimuth distributions of the data is not ideally even (see Fig. 4.5).

Furthermore, this migration method can be applied to a station array. Receiver functions at different stations pass through the upper mantle from different directions. By stacking the receiver function amplitudes, the intersection of ray paths within geographical bins can significantly improve the isolation of conversion signals. The scatter which may be coherent at individual stations commonly becomes incoherent in multi-station stacks.

3.3 Receiver function inversion

The waveforms of Ps and multiple reflections at shallow depth are inverted to get velocity-depth models (Owens et al., 1984; Owens and Zandt, 1985; Owens et al., 1987; Kind et al., 1995; Yuan et al., 1997). Plane wave theoretical seismograms are computed for the starting model using the method of Haskell (1962) for an incidence angle averaged over all epicentral distances. The theoretical traces are rotated and deconvolved in the same manner as the observed traces. The optimal parameters of the model are found by interactively minimizing the mean square deviation of the observed and theoretical traces and of the starting and final models (Kind et al., 1995). The V_p/V_s ratio can also be determined by this method. However, this inversion is highly non-unique (Ammon et al., 1990). It is relatively easy to obtain a good data fit with very complicated, probably not always realistic crustal models. This inversion procedure is applied for Hawaii data.

Chapter 4

The northwest Pacific subduction zone

4.1 Introduction

In the northwest Pacific region, the old (130 Ma) Pacific plate is subducted underneath the Eurasian Plate along the Kuril-, Japan-, Izu-Bonin- and the Mariana-trench with a rate of more than 90 mm/yr (DeMets et al., 1990). From north to south beneath Japan, the dipping angles of the slab becomes steeper (10° in the north and more than 30° in the south) and the strike direction changes from northeast to north and to northwest. The seismicity reaches a depth of more than 600 km beneath northeast China. Under the southern part of Japan the seismicity cuts off at about 500 km depth. In southwest Japan, the Philippine Sea Plate is subducted under the Eurasian Plate to the northwest from Nankai Trough, with a rate of 45 mm/yr since about 15 Ma.

The fate of the subducting Pacific Plate has been debated for a long time and remains controversial. Earlier tomographic studies (Kamiya et al., 1988; Zhou, 1988; Zhou and Clayton, 1990; Spakman et al., 1989, etc.) obtained unequivocal models of deep slab structure below the northwest Pacific island arcs, especially at the mantle transition zone depths (between 410 and 660 km depth). While Kamiya et al. (1988) suggested penetration of the Japanese slab below the 660, according to Zhou (1988) and Zhou and Clayton (1990), the major segments of seismic slabs should be flattened to sub-horizontal under Japan and the Izu-Bonin trench, and spread downward under parts of the Mariana and Kuril trenches. These different results could be caused by the lack of spatial resolution (Spakman et al., 1989). The tomographic inversions of P-wave data by van der Hilst et al. (1991, 1993) and Fukao et al (1992) imaged that beneath the region from the southern Kuril trench to Izu-Bonin, where the slab lies flat above the 660. Outside this region (at the northern Kurils and from the southern Izu-Bonin island arc to the Mariana trench), however, the slabs penetrate smoothly the 660 into the lower mantle. This result is supported by recent tomographic works (Bijwaard et al., 1998; Widiyantoro et al.,

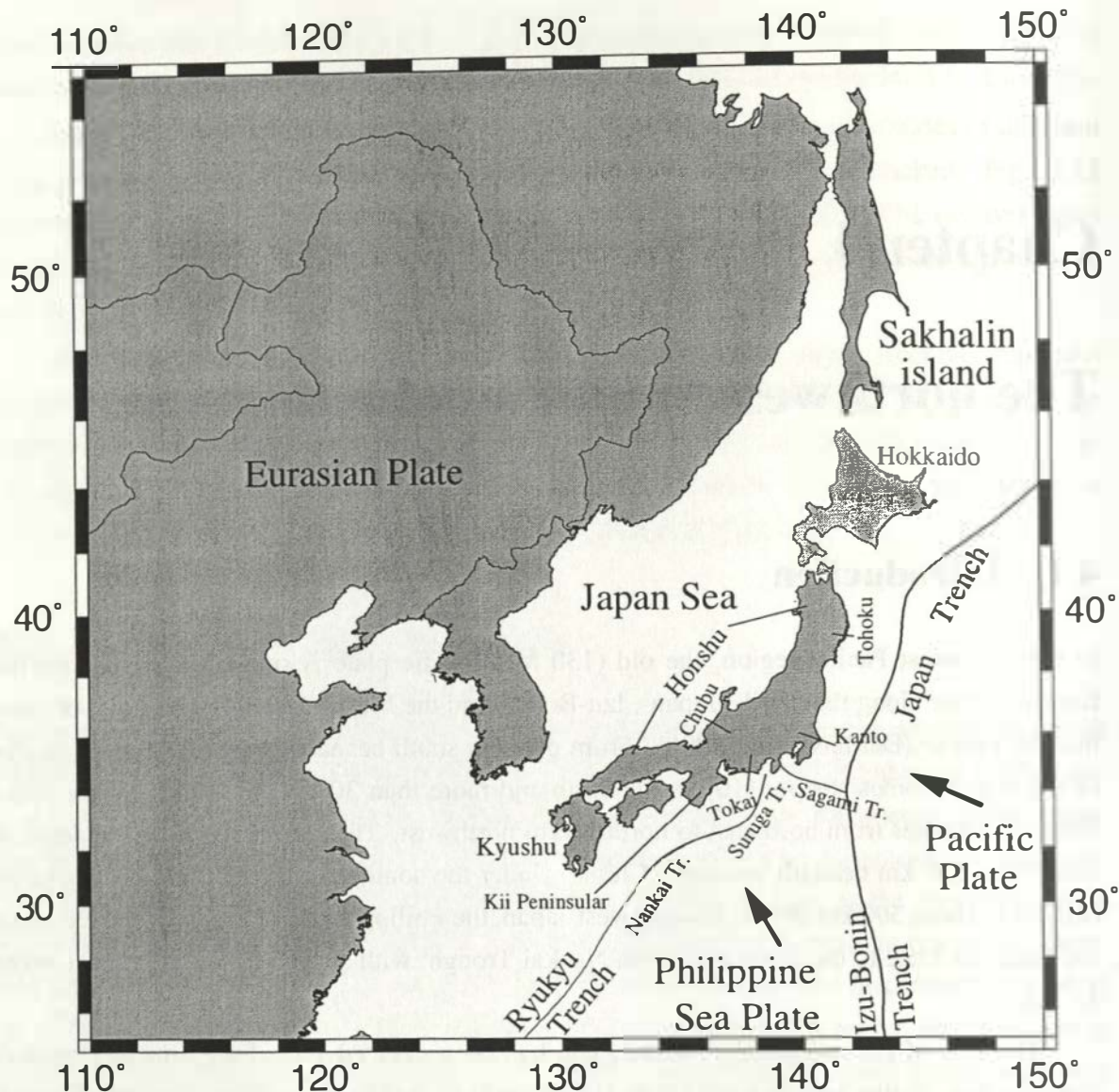


Figure 4.1: Map of the northwest Pacific subduction zone.

1999), however, Widiyantoro et al. (1999) pointed out that the S-wave image does not show clearly the deflection of the slab.

The subducted oceanic lithosphere can produce thermal perturbations and, when it reaches the upper mantle transition zone, topographic anomalies of the phase boundaries (the 410 and 660). If the slab is deflected and a large amount of cold slab material extends along the 660 over a broad area (a few hundred kilometers across) which is the case imaged by the tomography (e.g. van der Hilst et al., 1991; Fukao et al, 1992), a broad depression of the endothermic 660 phase boundary would be expected to have the same lateral extension (Shearer and Masters, 1992) and it could be observed with short- and long-period seismic data.

4.1.1 Previous studies of the 660

Long-period SS precursors were studied in the northwest Pacific subduction zone (e.g. Shearer, 1991; Shearer and Masters, 1992; Gossler and Kind, 1996; Flanagan and Shearer, 1998a; Gu et al., 1998). A large 660 trough is observed which is ~ 1500 km wide, 5000 km long and 15–20 km deep (Shearer, 1991, 1993; Shearer and Masters, 1992; Flanagan and Shearer, 1998a). Beneath Japan and the Kurils the depression of the 660 should reach about 20 km depth and due to small amplitude of the 410 topography, the transition zone should be ~ 20 km thicker (Shearer and Masters, 1992; Shearer, 1993; Flanagan and Shearer, 1998a). This broad 660 deepening is supported by ScS study (Revenaugh and Jordan, 1991a) and tomographic reports (e.g. van der Hilst et al., 1991; Fukao et al., 1992). However, also with long-period SS data contrary results are obtained by other authors. Petersen et al. (1993b) observed an elevated 660 to 10–20 km in the northwest Pacific ocean. The variations of the thickened and thinned transition zone shown by Gossler (1995) appear to occur in close proximity in the northwestern Pacific: relative to the IASP91, the transition zone is thinner under Kamchatka, the Kurils, Japan and northeast China, and becomes thicker beneath northwest China.

Studies of near receiver P-to-S conversions show the 660 topography beneath some individual stations: the 660 is relative deep in the subduction zone (Vinnik et al., 1996a); its depression is more than 50 km beneath Japan (station INU) (Thirot et al., 1998) Beneath station MDJ (Mudanjiang, northeast China) a multiple structure of the 660 is found down to 780 km depth at the tip of the subducting slab (Niu and Kawakatsu, 1996).

In Izu-Bonin, high resolution studies have been done using short-period near source phase conversions from teleseismic observations. Similar to the observations of long-period data (Shearer and Masters, 1992), a 660 trough (down to ~ 690 km depth) is observed (Collier and Helffrich, 1997). Its center lies at about (28°N , 140°E). The 660 reaches a normal depth (~ 670 km) beneath the northern part of Izu-Bonin (32°N). Vidale and Benz (1992) found a 10–20 km deepening of the 660 in Bonin (28°N) where it is 100 km far away from the intersection of the slab with the 660 towards the trench. Up to 50 km deepening of the 660 beneath Izu-Bonin is reported by Wicks and Richards (1993) and Castle and Creager (1997, 1998, 2000). The deepening begins right below the place of the seismicity cutoff (Castle and Creager, 1998). To the north ($\sim 32^{\circ}\text{N}$), the depression is over several hundreds of kilometers broad. To the south ($\sim 28^{\circ}\text{N}$), the depression of the discontinuity is concentrated in a narrow band.

A narrow band of the 660 depression could imply a penetration of slabs through the discontinuity. Over a considerable period of geological time, the subducted cold material could accumulate in a relatively small area in the transition zone. The cold and dense slab material can become entrained in the lower mantle (Griffiths et al., 1995; Guillou-Frottier et al., 1995; Christensen, 1996; Zhong and Gurnis, 1997). Thermal models which show subducting slabs

penetrating cleanly through the 660 into the lower mantle predict a greatly reduced mantle temperature in a narrow zone (Schubert et al., 1975; Creager and Jordan, 1986). The depression of the 660 phase boundary should be narrow, which could be the case in south Izu-Bonin ($\sim 28^\circ\text{N}$) (Castle and Creager, 1998). However, these thermal models predict neither the 660 deepening observed by Collier and Helffrich (1997) and Benz and Vidale (1993) (conversion points are at least 100 km to the side of the slab in both papers), nor the observations of a broad 660 depression in north Izu-Bonin ($\sim 32^\circ\text{N}$) by short-period studies (Castle and Creager, 1997, 1998, 2000; Wicks and Richards, 1993) and in the northwest Pacific by long-period data (Shearer, 1991; Shearer and Masters, 1992; Flanagan and Shearer, 1998a). The most likely explanation for the wide regional 660 depression is that the slab broadens or deflects near 660 km depth, thus spreading the cold slab temperature into the adjacent mantle (van der Hilst et al., 1991; Shearer and Masters, 1992).

The apparent deflection of the slab could result from the resistance to slab penetration through the 660 phase change (e.g. Machel and Weber, 1991). The interaction of subducting slabs with mantle structure depends on several conditions, including the viscosity of the various layers, the Clapeyron slopes of the mineral phase changes and the regional subduction history. Seismological observations and numerical simulations of mantle flow suggest that the lower mantle is at least 10–30 times more viscous than the upper mantle (Gurnis and Hager, 1988). An increase in viscosity across the 660 could cause the impinging slabs to buckle and thicken, to produce strong slab distortion (Gurnis and Hager, 1988). Also, an increased Clapeyron slope magnitude can cause the separation of the upper and lower mantle. But these models failed to explain the case in the northwest Pacific, where the subducted lithosphere deflects at the base of the upper mantle below particular island arcs, but sinks into the lower mantle below the others.

The northern Izu trench is argued to have retreated seaward almost 1000 km to the northeast since 20 to 17 million years ago (e.g. van der Hilst and Seno, 1993). Numerical modeling of slab dynamics (Christensen, 1996) shows that for a rapid retreating trench model, slabs are expected not immediately to penetrate into the lower mantle, but rather temporarily to lay out horizontally upon the 660. In this case, the subducted cold material floating on the 660 should cause the temperature anomaly extending to a large area.

4.1.2 Previous studies of the 410

Relative to the 660, there are less observations of the 410 and the results show large discrepancies. The 410 studies are concentrating in the short-period data of the Izu-Bonin area. A 410 “swell” is observed by Collier and Helffrich (1997) which has the maximum uplift of 50 km over about 6° broad and centered at (31°N , 139°E). No 410 is observed in Izu-Bonin by Vidale and Benz (1992). Beneath central Japan an up to 60 km uplift of the 410 is reported by a

receiver function study (Thirot et al., 1998).

The slab in Izu-Bonin could be thicker than expected or it cools the mantle more effectively than previously thought (Collier and Helffrich, 1997). The 410 depth could be strongly distorted by the slab. The short-period observations mentioned above were made inside or in the vicinity of the slab. That might be the reason for the discrepancy of the results.

4.2 Data

1. Seismic stations

In this chapter, receiver function analysis is used to study the upper mantle discontinuities in the northwest Pacific subduction zone (Fig. 4.1). Recently, more and more seismic data have become available from 3-component broadband stations located in this area. I have found 35 stations located in Japan, South and North Korea, Russia and northeast China (Fig. 4.2, Table 4.1 and Table 4.2). These stations belong to the CDSN (the Chinese Digital Seismic Network), the French GEOSCOPE network, the GSN (the Global Seismographic Network), the Japanese FREESIA network (Fundamental Research on Earthquakes and Earth's Interior Anomalies) and a PASSCAL experiment XL95-96. The 3 short-period PASSCAL stations in North Korea are considered as one (named XL) because they were very closely deployed (Table 4.1). The data

Table 4.1: CDSN, GEOSCOPE and GSN Stations

Code	latitude (°)	longitude (°)	number of RFs	network
BJI	40.04	116.17	289	CDSN
ERM	42.01	143.15	227	GEOSCOPE
HIA	49.26	119.74	507	CDSN
INCN	37.48	126.63	114	GSN
INU	35.34	137.01	533	GEOSCOPE
MAJO	36.54	138.20	329	GSN
MDJ	44.61	129.59	352	CDSN
SSE	31.09	121.18	243	CDSN
YSS	46.95	142.75	269	GSN
XL*	40.13	128.37	55	PASSCAL

*XL = "pseudo-station" for PASSCAL experiment XL95-96, which deployed 3 short-period seismic stations SOK (40.135°N, 128.369°E), HMP (40.111°, 128.286°E) and RJU (40.168°N, 128.331°E).

Table 4.2: FREESIA Stations

Code	latitude (°)	longitude (°)	number of RF's
ABU	34.86	135.57	40
CHS	35.70	140.85	36
FUJ	35.22	138.42	143
GJM	39.95	140.11	47
HKW	35.09	138.13	112
HSS	42.96	141.23	138
ISI	34.05	134.45	189
IWT	35.92	139.73	39
JIZ	34.91	138.99	226
KFU	35.73	138.56	114
KIS	33.86	135.89	203
KZK	37.29	138.51	131
NAA	35.22	137.36	105
NMR	43.36	145.74	122
OHS	34.68	138.01	61
SBT	37.96	139.45	57
SGN	35.50	138.94	195
SMZ	34.98	138.51	52
TKA	31.51	130.78	171
TKD	32.81	131.39	198
TMR	41.09	141.38	62
TNK	44.77	142.08	133
TNR	34.90	137.88	118
TYM	34.97	139.84	102
YMZ	36.92	140.24	42

of FREESIA can be requested from its data center in Japan, all other data are available from the IRIS data center in Seattle, Washington.

2. Data

Data provided by IRIS and GEOSCOPE are in Seed format, by FREESIA in MiniSeed format. The waveform data of each earthquake records are requested in a time window from 100 sec before to 200 sec after the theoretical P arrival. As described in the last chapter, records of earth-

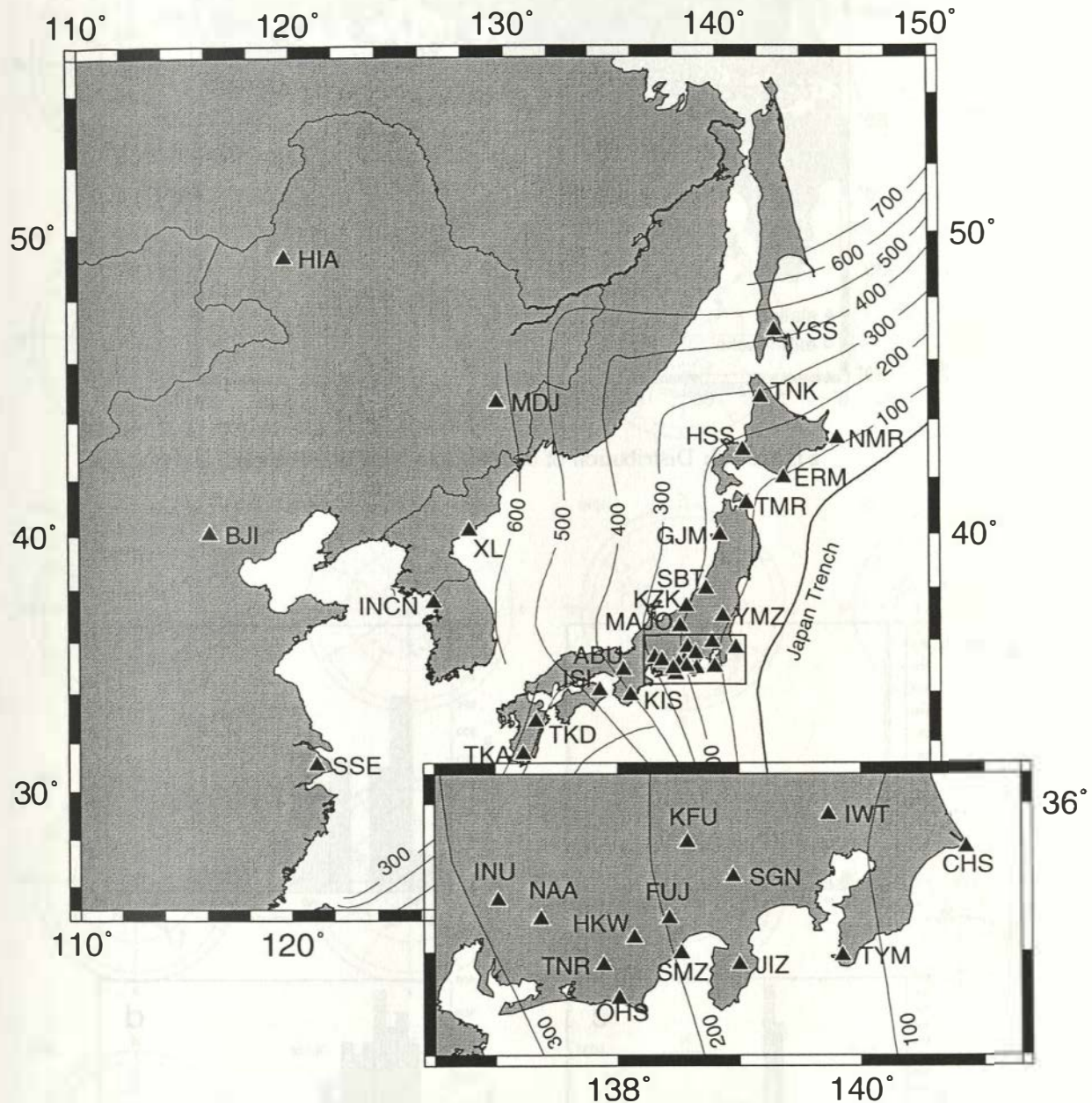


Figure 4.2: Stations used in this work. Contour lines delineate the Pacific and the Philippine slabs (Gudmundsson and Sambridge, 1998).

quakes with magnitudes larger than 5.5 and epicentral distances within 30–95° are requested. Because the FREESIA network was set up after 1995, some of its stations have a very short operation time. Records at these stations are used also for earthquakes with magnitudes greater than 5.3 and relatively high signal-noise ratios. The criteria of data selection is described in the

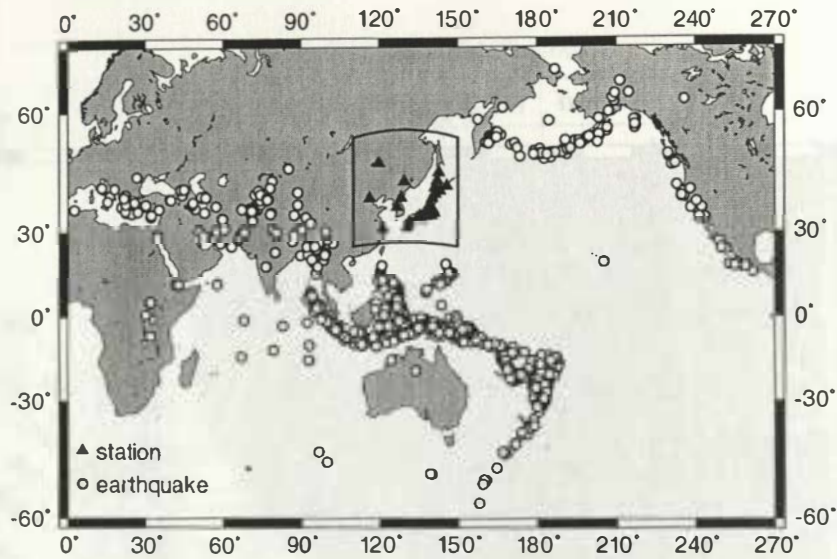


Figure 4.3: Distribution of earthquakes used in this work.

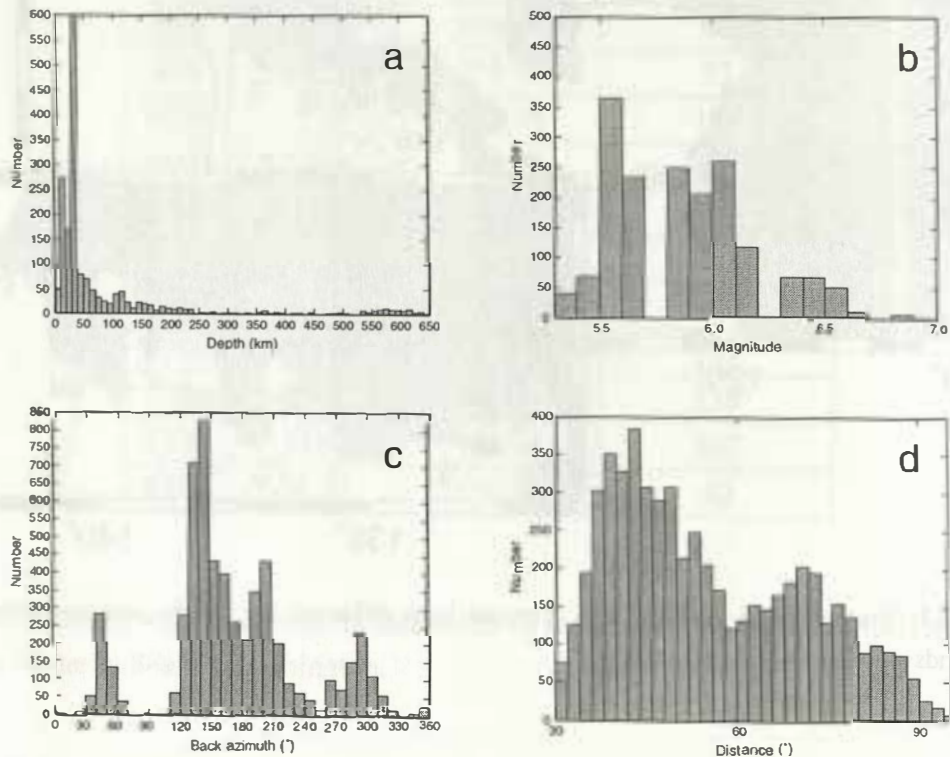


Figure 4.4: Earthquake information of receiver functions used in this study. Distributions of focal depths (a) and magnitudes (b) of all 1284 earthquakes. Distributions of back azimuths (c) and epicentral distances (d) of all 5749 receiver functions.

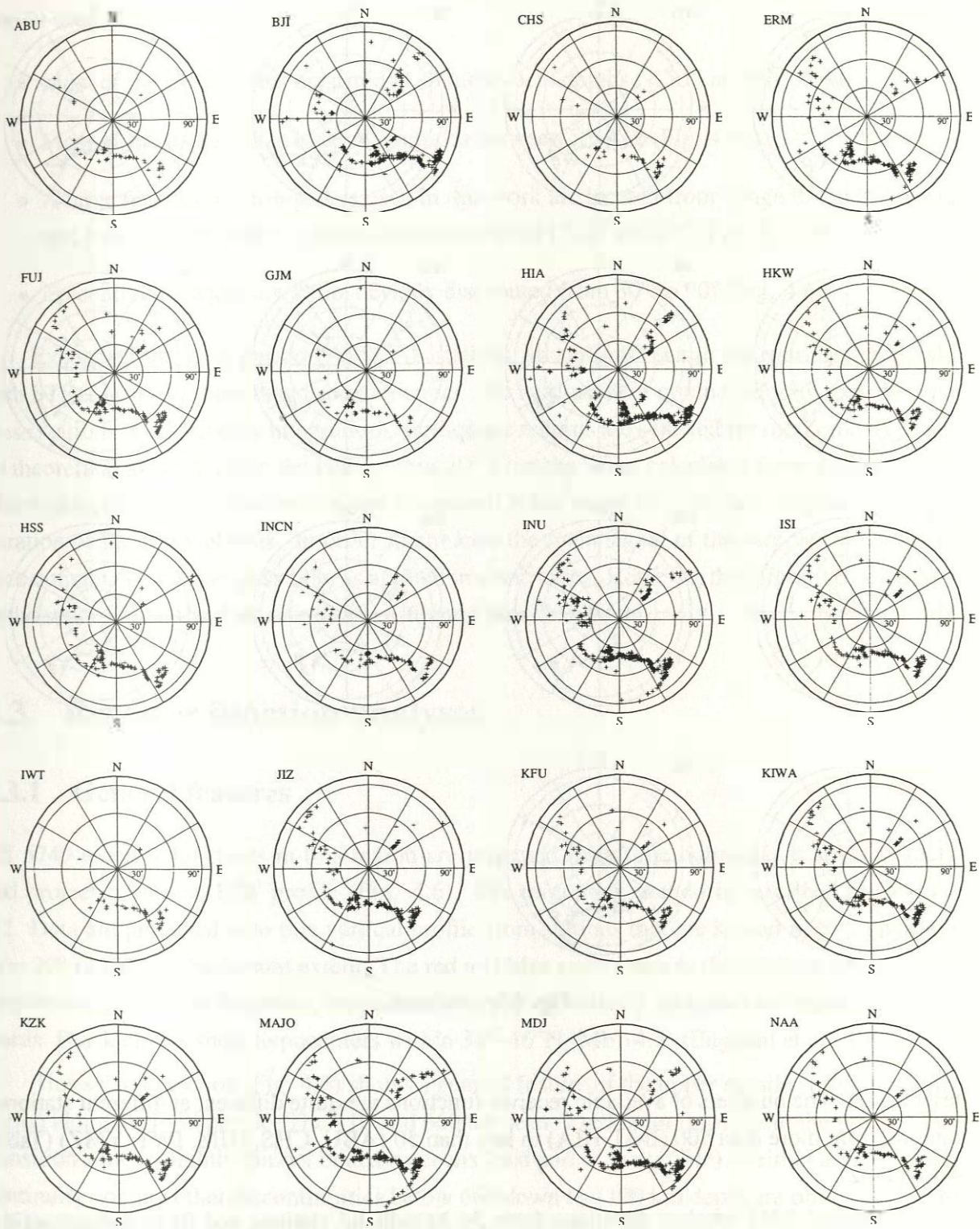


Figure 4.5: Back azimuth-epicentral distance distributions of all events recorded at each station.

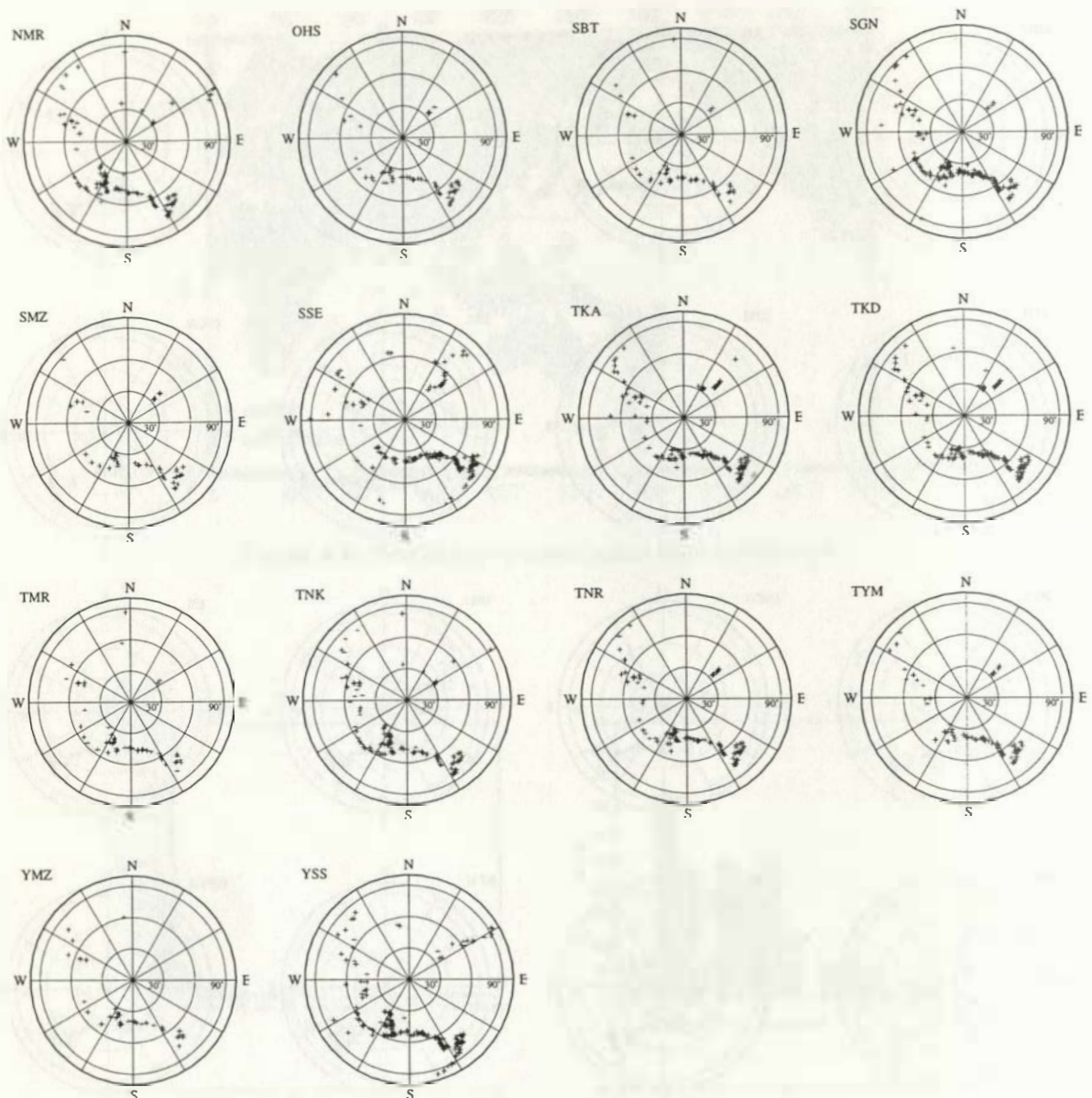


Fig. 4.5: continued.

last chapter. The numbers of available receiver functions are quite different at different stations, ranging from more than 500 (INU, HIA) to less than 50 (ABU, CHS, GJM, IWT, YMZ) (Table 4.1 and 4.2).

A total of 5749 receiver functions from 34 broadband stations and from 3 short-period stations are used in this work. More than 1000 earthquakes are selected to calculate the receiver functions (Fig. 4.3). Fig. 4.4a and 4.4b show their depth and magnitude distributions, Fig. 4.4c and 4.4d show the back azimuth and epicentral distance distributions of all receiver functions. Fig. 4.5 shows the back azimuth-epicentral distance distributions of receiver functions at each

station used in this study.

- Most of the earthquakes occurred at shallow focal depths (<50 km) (Fig. 4.4a);
- Most of the earthquakes have magnitudes between 5.5–6.2 (Fig. 4.4b).
- A large number of earthquakes used in this work are located from Tonga to the Indonesia arc, their back azimuths to each station are within 120° to 220° (Fig. 4.5 and 4.4c);
- Epicentral distances are almost evenly distributed from 30° to 90° (Fig. 4.4d);

Except for the short-period PASSCAL stations, all stations used in this work are equipped with STS-1 or STS-2 broadband seismometers. The restitution of ground velocity records from these stations is replaced by integration. Earthquake records are selected for rotation only when its theoretical azimuth angle deviates within 20° from the value calculated from the P arrivals. The width of the deconvolution window is selected in the range 80 to 120 sec, depending on the duration of the P waveforms. In order to enhance the main signal of the receiver functions in time domain, a 5 sec low pass filter is applied in some cases. However, the migration procedure in the space domain is done using the un-filtered broadband data.

4.3 Receiver function analyses

4.3.1 General features

All 5749 receiver functions in this region are migrated from time domain into space domain and projected onto an E-W profile (Fig. 4.6). The migration method is described in Chapter 3.2. Data are projected onto this vertical profile from stations that are spread in N-S direction over 20° (2200 km) horizontal extent. The red and blue colors denote the positive and negative amplitudes of receiver functions, respectively, implying velocity increases or decreases downwards. Black circles show hypocenters within 34° – 46° N ($M_b > 4.5$) (Engdahl et al., 1998).

This seismic section (Fig. 4.6) shows a general feature of the upper mantle structure in this region along the E-W profile. The 410 and 660 are seen in red color throughout the profile. The transition zone is slightly thinner beneath oceans (east part of the profile). Neither a 520 km discontinuity nor any other discontinuities below 660 down to 1100 km depth are observed. There are no significant negative signals from a possible low velocity zone at about 300 km depth which was suggested by Revenaugh and Sipkin (1994a) and Revenaugh and Sipkin (1994b).

From central to western Honshu and to Kyoshu in southwest Japan, there are 22 broadband stations which are located within 4° latitude (Fig. 4.2). The piercing points of receiver functions from these stations at 660 km depth cover an area less than 6° broad in latitude. These receiver

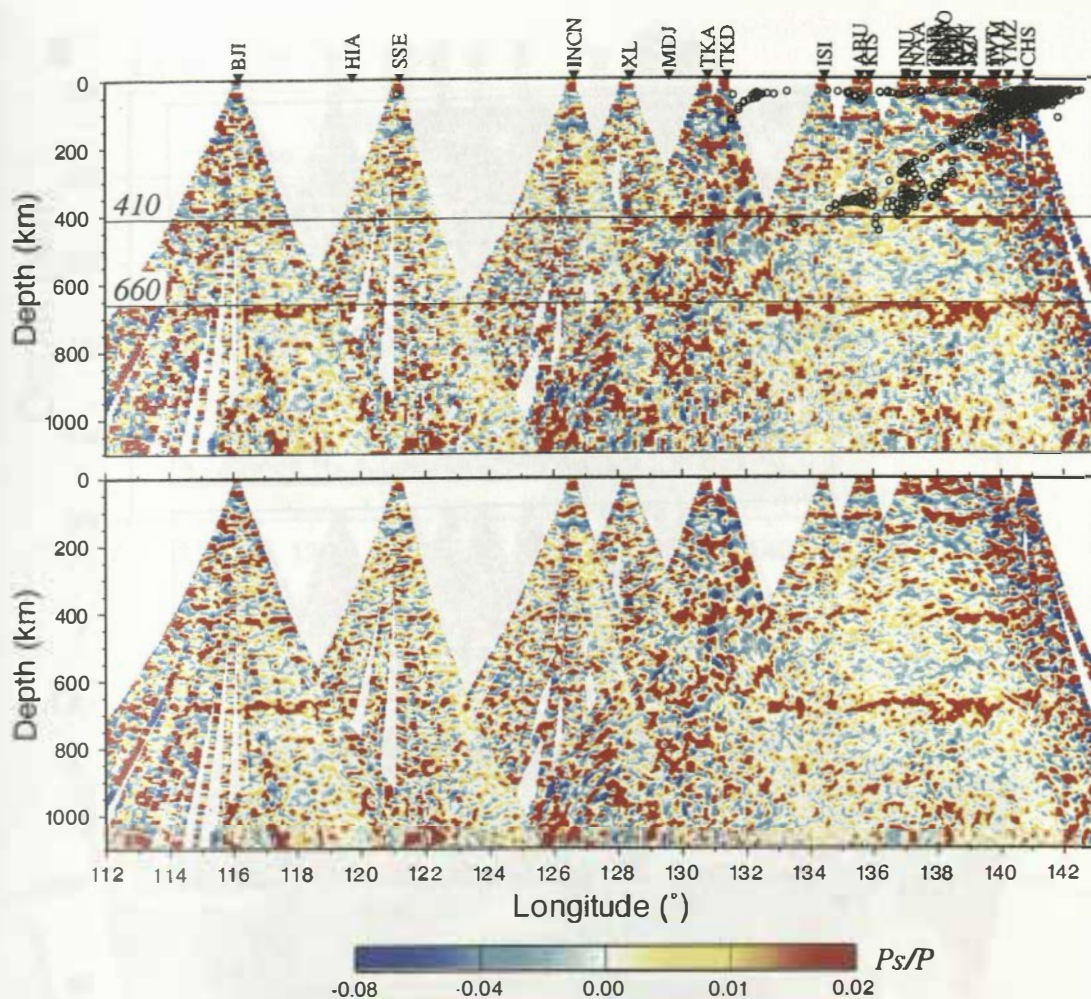


Figure 4.7: An E-W projection of migrated receiver functions from 26 stations located between 30° – 40° N latitude. In the subduction zone (east side of the profile) the lateral average of the data in N-S direction is less than 6° (660 km). Seismicity is within 30° – 38° N latitude ($M_b > 4.5$).

of the large lateral data averaging. Under the Japanese islands the 410 is almost continuous from east to west with little topographic changes, except a small gap (near 136° E) right in the position where the slab intersects the 410 implied by seismicity (Fig. 4.7).

Beneath the continents, the 410 and 660 can be imaged by the migrated receiver functions from individual continental stations BJI, SSE and HIA. The 410 and 660 under station HIA have been already shown in the last chapter (Fig. 3.12). In Fig. 4.7 the migrated receiver functions from stations BJI and SSE do not overlap at depth shallower than 660 km, thus the 410 and 660 image in this segment of the profile reflect their existence beneath BJI and SSE.

In the northeast part of the area (Fig. 4.2), the Japanese stations which are located within 137° – 146° E from central to northern Honshu and to Hokkaido (northern Japan) are selected. Their receiver functions together with those from station YSS in Sakhalin (24 stations totally)

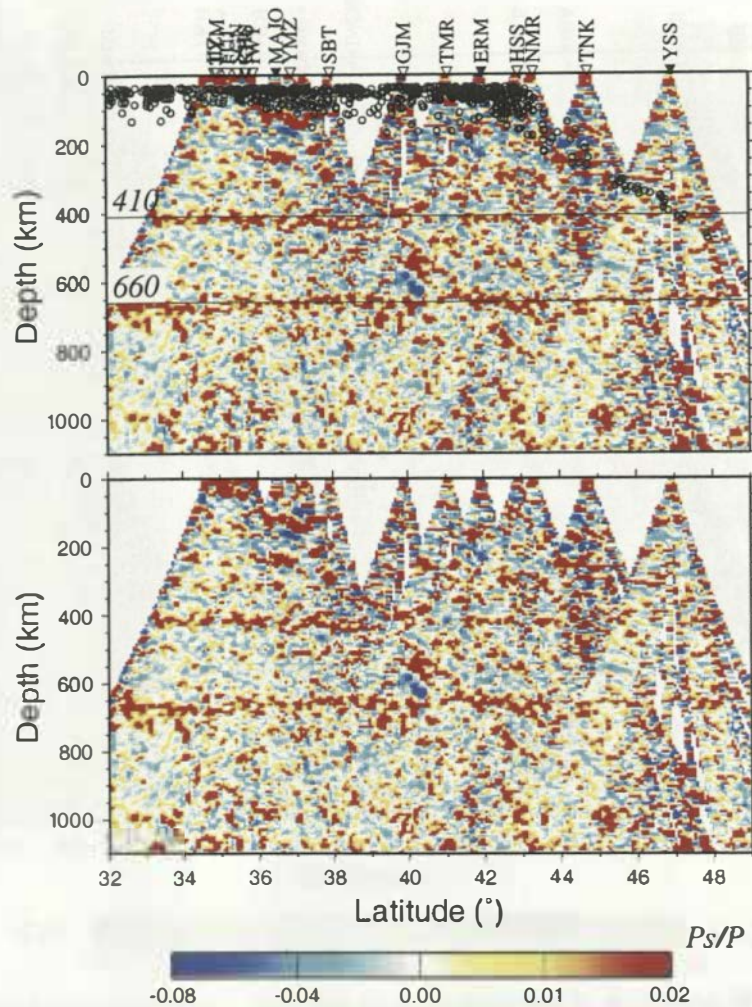


Figure 4.8: A N-S projection of migrated receiver functions from 24 stations which are located between 137° – 146° E longitude. The data averaging in E-W direction covers 6° (540 km). The shown seismicity is within 140° – 146° N longitude ($M_b > 4.5$).

are migrated and projected onto a N-S profile (Fig. 4.8). In this profile, the lateral data averaging in E-W direction is limited within 6° (540 km) at 660 km depth and the 410 and 660 below the island are imaged along the N-S direction. A slight uplift of the 660 occurs around 40° N. At the northernmost part of this section, the 410 and 660 become weak where the slab intersects them. But there is no indication of a large lateral extended deepening of the 660.

4.3.2 Topography of the 410 and 660

In order to map the lateral topographic variation of the 410 and 660 in the northwest Pacific, the migrated receiver functions are projected onto several E-W profiles which have 4° width in N-S

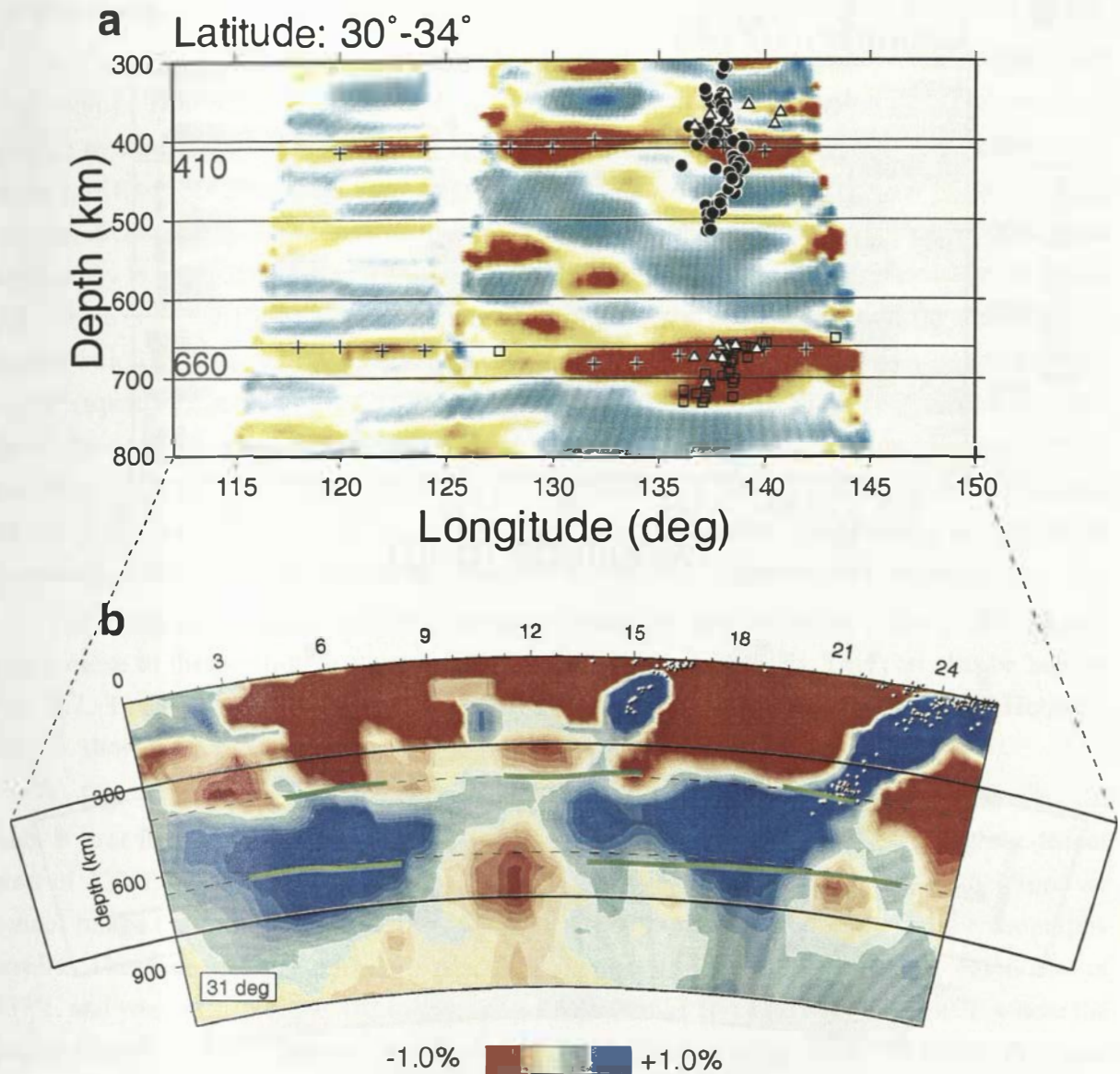


Figure 4.9: a). Migrated receiver functions within 30° – 34° N latitude are projected onto an E-W profile. The depths of the maximum amplitudes of the 410 and 660 are measured and marked by crosses. These measurements are also used in Fig. 4.11a and 4.12a. Black dots indicate the seismicity, squares are the depth measurements by Castle and Creager (1998) and triangles by Collier and Helffrich (1997). b). Tomographic section at 31° N latitude (Bijwaard et al., 1998). Red lines are the 410 and 660 measurements from a). White dots are seismicity shown by the tomographic study. They are not identical to the dots in a), because the receiver functions concentrate somewhat north.

direction. Along each profile, data are spatially averaged within a box of about 4° (~ 360 km) broad and 20 km high. After migration, the 410 and 660 phases are identified in each profile and the location of their maximum amplitudes are determined. Two examples of such profiles

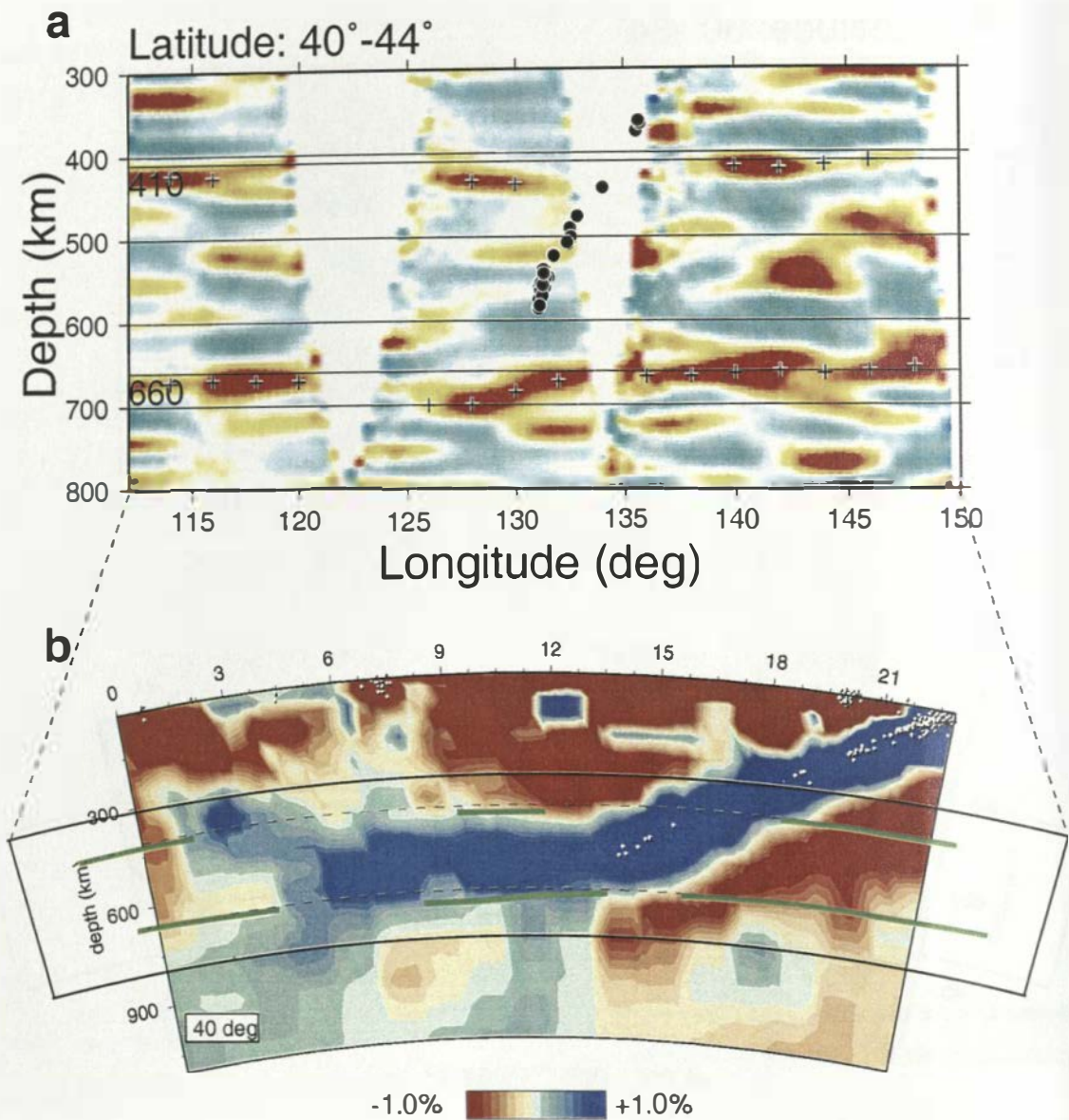


Figure 4.10: a). Migrated receiver functions within 40°–44°N latitude. Symbols are the same as in Fig. 4.9. b). A tomographic section at 40°N latitude (Bijwaard et al., 1998).

are shown in Fig. 4.9a and 4.10a.

In these two E-W profiles, the migrated receiver functions between 30°–34°N and between 40°–44°N are displayed. Black dots denote the seismicity within the associated regions, squares are 660 depth measurements by Castle and Creager (1998), and triangles are data obtained by Collier and Helffrich (1997). The crosses denote the positions of the maximum amplitudes of the 410 and 660 phases. These depth measurements are shown as red lines in tomographic sections at 31°N (Fig. 4.9b) and at 40°N (Fig. 4.10b) (Bijwaard et al., 1998), respectively. They

are also shown in the horizontal images of the 410 and 660 topography (Fig. 4.11a and 4.12a).

In Fig. 4.9a, the seismicity is not quite identical to those used by the tomographic study (Fig. 4.9b). This is because the receiver functions concentrate somewhat north to the tomographic section. The 660 phase is strong between 130° – 145° E and becomes weak in the west. From 140° E to 130° E, the 660 deepens gradually to the west (see also Fig. 4.7), but not abruptly and significantly as predicted by short-period studies (Castle and Creager, 1998). The largest topography is up to 20 km at around 130° E, exactly in the region where it should be hit by the slab. There is no clear large 660 deepening right beneath the seismicity cutoff (at about 500 km depth) which was found by Collier and Helffrich (1997) (triangles) and Castle and Creager (1998) (squares) in the same region. Although there is some energy in the receiver function image at the depth consistent with the results of the short-period data (Castle and Creager, 1998), the 660 is more likely not deeper than 680 km. Between 118° and 124° E where the slab should lie flat on the 660 imaged by the tomography, the receiver function image shows no significant deepening of the 660 which would be expected from a broad extension of cold slab material.

The 410 is very close to its global average value (410 km) along the entire profile. A 410 gap is close to the position of the seismicity at this depth ($\sim 135^{\circ}$ E). This can also be seen in Fig. 4.7. The shallow 410 observations in this region (up to 350 km by Collier and Helffrich (1997), shown by the triangles) is not confirmed by the receiver function image.

In Fig. 4.10a, the 660 is depressed to 700 km depth where it should be interacted by the slab. It is at its normal depth (660 km) in the region east of 132° E and is only slightly deeper west of 120° E. Between 120° – 125° E there is almost no data at 660 km depth, therefore we cannot image the 660 in this area where a flat-lying slab is suggested by seismic tomography results. There are three segments of the 410 observations in Fig. 4.10. In the region east of 137° E and west of 120° E the 410 topography varies within 10 km. At around 130° E where the station MDJ is located (Table 4.1 and Fig. 4.2), the 410 seems to be at 440 km depth. At about 135° E where the slab crosses the 410, there are unfortunately no data.

The depth values of the 410 and 660 are measured on such profiles in every 2° . These data are plotted in two horizontal sections with blue or yellow colors on their associated geographical positions (Fig. 4.11a and 4.12a). The green crosses in each figure mark the positions of piercing points at the corresponding discontinuity, describing the data distribution at that depth. No measurement is made where the 410 and 660 phases are not identified. Fig. 4.13a maps the variation of the transition zone thickness, the value in each geographical box is the depth difference between the associated 660 and 410. There is no measurement if the 410 and/or 660 phase are not observed. Fig. 4.11b, 4.12b and 4.13b are tomographic cross sections at 410, 660 and 520 km depth (Bijwaard et al., 1998). The regions of the largest anomaly of the 660 topography (Fig. 4.12a) and of the transition zone thickness (Fig. 4.13a) are delineated with red and blue colors, respectively.

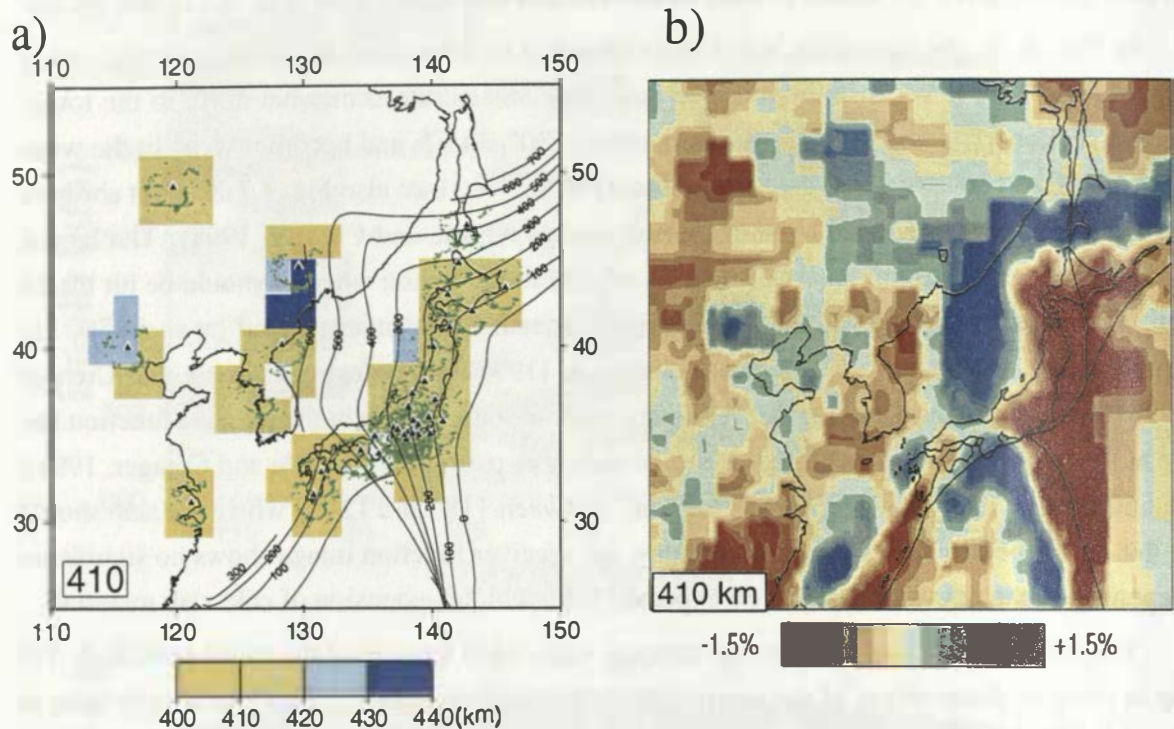


Figure 4.11: a). Depth measurements of the 410 from receiver functions. Yellow and blue colors mark different depth values. No measurements are made when the phase is difficult to be identified. Green crosses mark the conversion points at 410 km depth and describe the sampling area of the data. Black triangles are stations. Lines of slab contours are from Gudmundsson and Sambridge (1998). b). Tomographic image at 410 km depth (Bijwaard et al., 1998). Blue and red colors indicate fast and slow velocity anomaly, respectively.

- In Fig. 4.11a, the 410 keeps its global average depth in almost the entire region. It shows little topography and seems to be less affected by the subducting process: There is no observations of significant updoming due to cold temperature. This is consistent with the observations of SS precursors (e.g. Shearer, 1991). Along the 400 contour line of the Pacific slab, there is no 410 observations by the receiver functions in southern Japan (33° – 36° N, 135° E) and southern Sakhalin (45° – 48° N, 142° E). This can also be seen in the receiver function profile in Fig. 4.9a and it agrees with the observations of Vinnik et al. (1996a). The largest 410 topography is the apparent 30 km depression in the region south to the station MDJ (44° N, 130° E). The feature was also observed by Flanagan and Shearer (1998b). This region is more than 4° (~ 360 km) apart from the 400 contour line of the slab and in the direction away from the trench. This apparent deep 410 could be caused by the low velocities in the back arc regions at shallow depth (Flanagan and Shearer, 1998a). If this is not the case, I have no explanations for this deepening of the

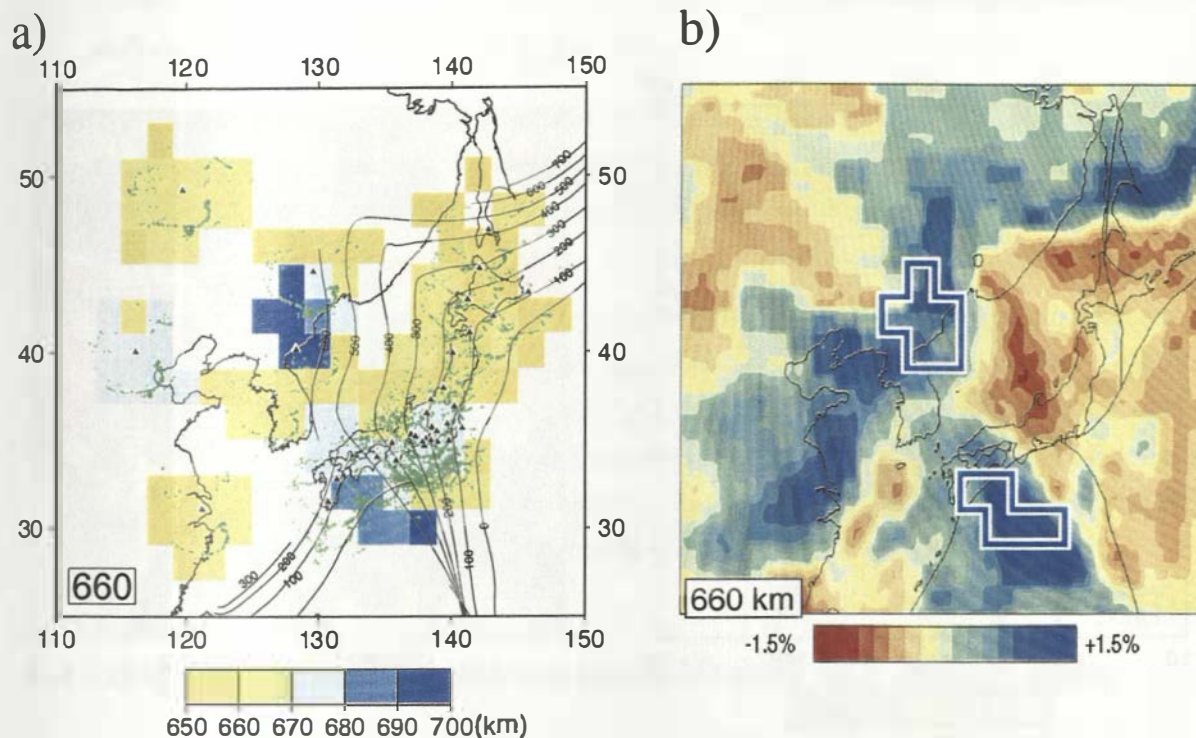


Figure 4.12: a). Measurements of the 660 from receiver functions. Symbols are the same as in Fig. 4.11a. Piercing points are at 660 km depth. b). Tomographic image at 660 km depth (Bijwaard et al., 1998). Blue boxes delineate the two regions with the deep 660 measurements.

410 which is far away from the slab.

In the thermal elevation model of the 410 due to the slab penetration, the topographic anomaly of the 410 should extend laterally over more than 200 km and therefore be detectable by receiver functions. Thus, the absence of the 410 in this region might be attributed to large topographic anomalies within a small scale, probably caused by dynamically delayed olivine-spinel phase transformation. Another possibility of the dim 410 could be the broadening of the α - β phase transformation which makes it less seismic visible (Helffrich and Bina, 1994; Collier and Helffrich, 1997).

- Relative to the 410, the 660 shows larger topography (Fig. 4.12a). The deepest 660 is found to be at 680 and 700 km depth in the regions where it should be hit by the slab (4.12b). The deep hypocenters corresponding to these two regions reach about 500 to 600 km depth, respectively. In the region around 32°N, 120°E (near the station SSE), receiver functions do not show a consistent image of the slab as the tomography does (see also Fig. 4.9). In the region around 30°N, 130°E there is no observations of the 660 by the receiver functions (see also Fig. 4.7). Between 40°–48°N and 120°–125°E there is a

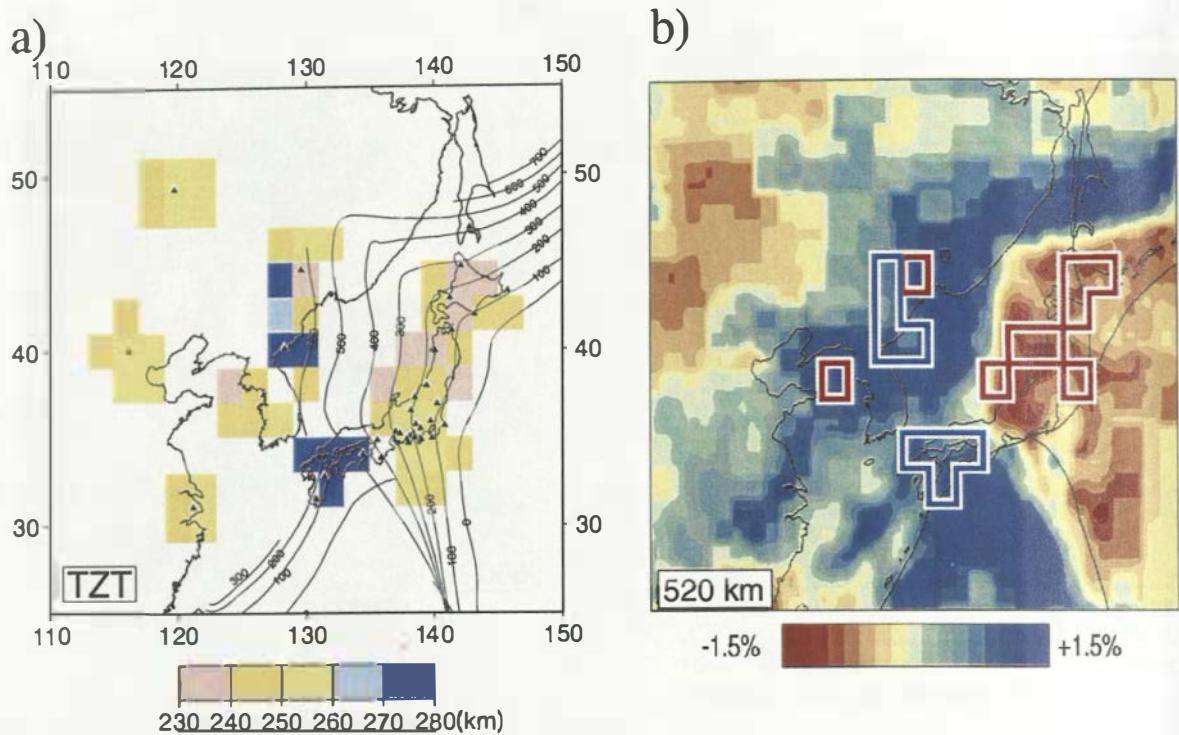


Figure 4.13: a). Transition zone thickness from receiver functions. Symbols are the same as in Fig. 4.11a. No measurements are made if 410 and/or 660 are absent. b). Tomographic image at 520 km depth (Bijwaard et al., 1998). Blue and red boxes delineate the regions of thicker or thinner transition zone measured from receiver functions relative to the IASP91 model (250 km).

lack of data sampling.

Thermal models of subducting slabs which cleanly penetrate the 660 (e.g. Schubert et al., 1975; Creager and Jordan, 1986) predict a 100–200 km wide slab with a maximum temperature anomaly of -900°C . Such a slab will cause a narrow 660 depression. In Fig. 4.12, the largest 660 deepening is associated with the coldest slab segment (near 40°N , 125°E) which is indicated by the existence of deep seismicity (till about 600 km depth). East to Kyushu (30°N), where seismicity cuts off at about 500 km depth, the 660 deepening is 20 km. West to this region there are no observations of the 660, which might be attributed to the regional tectonic history (trench retreating).

The 660 depth measurements from receiver functions (Fig. 4.12a) do not support the idea of a broad 660 deepening suggested by the studies with long-period data (e.g. Shearer, 1991, 1993; Shearer and Masters, 1992; Flanagan and Shearer, 1998a). In contrary, the 660 topography in Fig. 4.12 is more consistent with the new tomographic image by Widiyantoro et al. (1999), which shows that in spite of the deflected slab imaged by P

wave tomography, the S wave tomography shows that in Izu-Bonin region the slab is not deflected, but penetrates the 660 also in the north.

- The transition zone thickness is, relative to the value in the IASP91 (250 km), up to 30 km thicker in the region where the tomography shows the existence of the slab at that depths and is about 20 km thinner beneath the northeast Japan where the velocity is imaged to be low (Fig. 4.13b).

The variations of the transition zone thickness provide a temperature measurement at the transition zone depths. According to Gossler and Kind (1996), the thinner (~ 20 km) and thicker (~ 30 km) thickness values imply the temperature anomalies of about $+150^\circ\text{C}$ and -200°C , respectively, in the associated regions (Fig. 4.13). However, the values of the cold temperature could be underestimated, particularly in the region around 40°N , 130°E , where the slab should subduct with smaller dipping angle (Helffrich, 2000).

4.4 Further discussions on the 410 and 660 topography

In this section the 410 and 660 are studied in time domain with the individual receiver functions from individual stations. The moveout correction method which is described in Chapter 3.2 is applied to get coherent conversion phases in receiver functions.

4.4.1 The continental stations HIA, BJI and SSE

At these stations, the 410 and 660 phases are seen clearly in the individual receiver functions. Fig. 3.11b shows the receiver functions from the station HIA. The individual traces are moveout corrected and then summed within 1° bins of epicentral distances. The “sum” trace at the top of this figure is the summation of all individual traces. Fig. 4.14 shows receiver functions at the station SSE and BJI in the back azimuth window of $90\text{--}270^\circ$. Grey lines labeled “P410s” and “P660s” indicate the calculated delay times for the 410 and 660 in the IASP91 model,

Table 4.3: The 410 and 660 beneath HIA, BJI and SSE

station	t_{410} (sec)	t_{660} (sec)	$t_{660}-t_{410}$ (sec)
HIA	45.0	69.0	24.0
BJI	45.1	69.6	24.5
SSE	44.2	68.6	24.4
IASP91	44.1	68.1	25.0

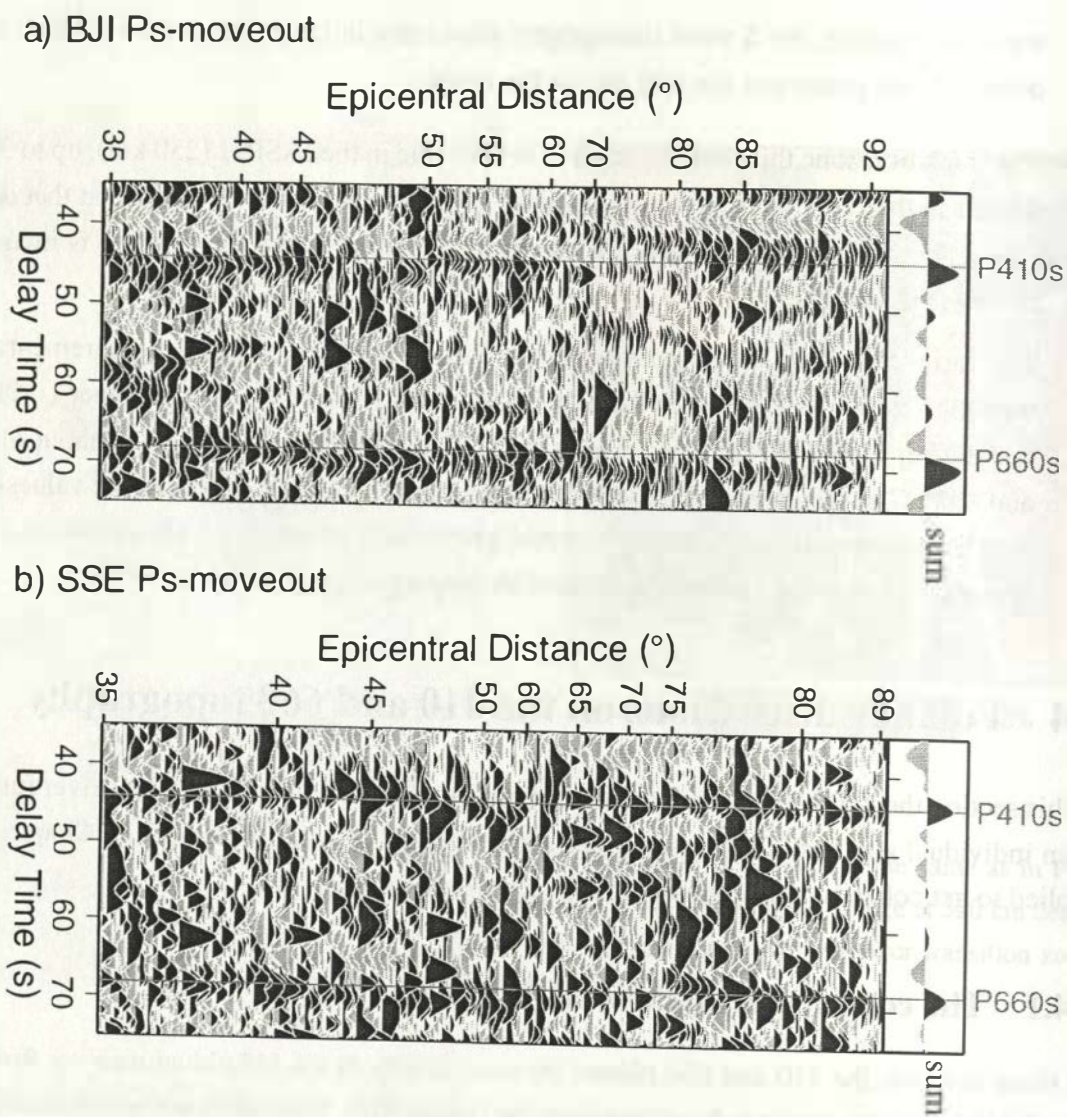


Figure 4.14: Part of individual receiver functions (back azimuth between 90° – 270°) from stations BJI and SSE. They have been Ps moveout corrected and sorted by their epicentral distances. The traces labeled “sum” at the right side are summations of all individual receiver functions from each station. Grey lines labeled “P410s” and “P660s” indicate the calculated delay times of the 410 and 660 for the IASP91 model, with a reference distance of 67° .

with a reference distance of 67° . For each station, the delay times of the 410 and 660 phases are measured from the summation traces (Figs. 4.14 and 3.11b) and listed in Table 4.3. The transition zone thickness beneath HIA, BJI and SSE are 250 km (24.0 sec), 255 km (24.5 sec) and 254 km (24.4 sec), respectively, which seems not to be influenced by the subduction process.

MDJ Ps-moveout

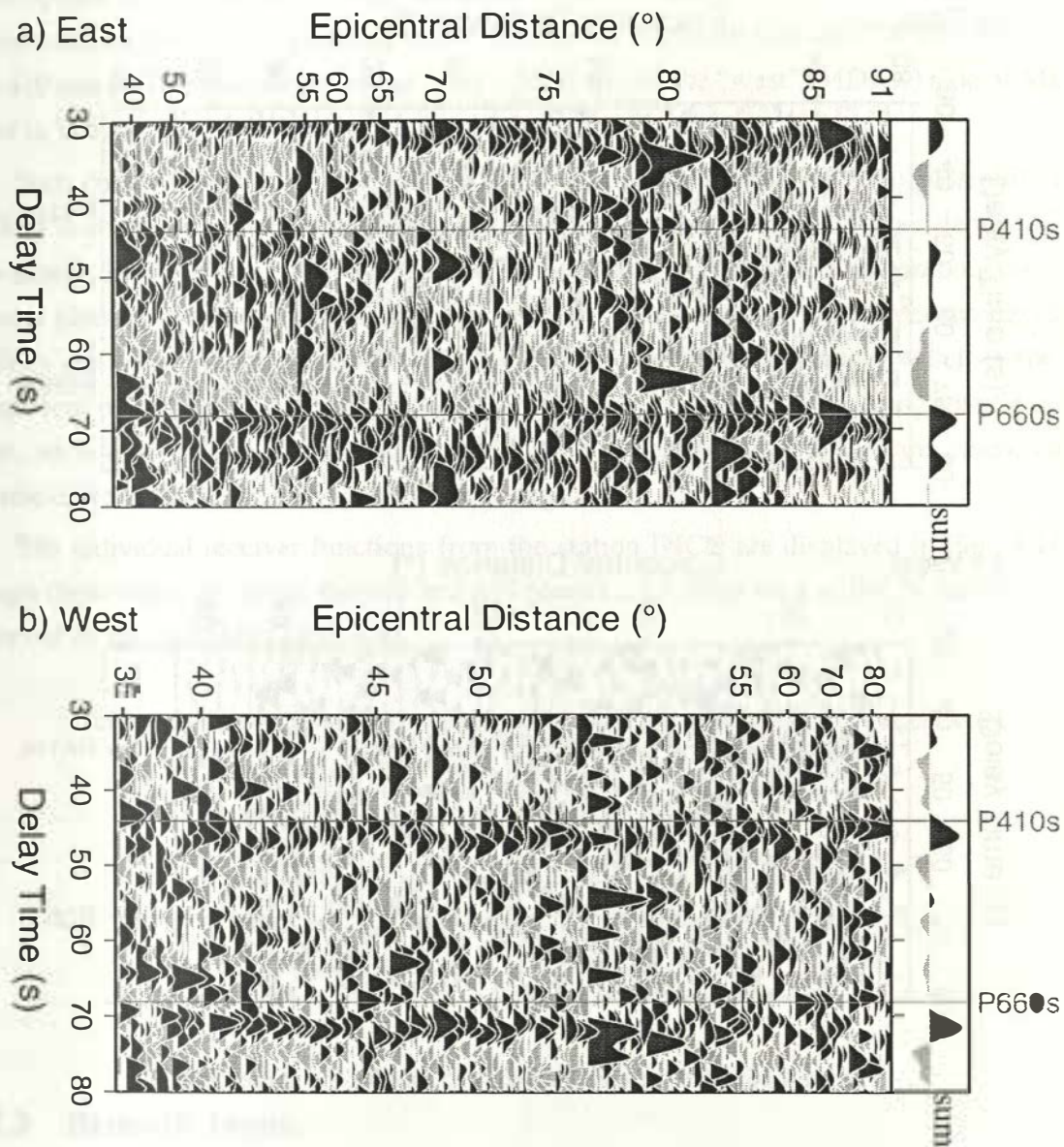


Figure 4.15: Individual receiver functions from station MDJ which have back azimuth between 0° – 170° (“East”, shown at the top) and 170° – 360° (“West”, shown at the bottom). In each figure, the traces have been Ps moveout corrected and sorted by their epicentral distances. The “sum” traces are the summations of receiver functions within each azimuthal range.

4.4.2 Stations MDJ and INCN

Near these two stations, the slab might reach about 660 km depth. The 600 contour line of the Pacific slab indicates that the strike is almost in N-S direction at these stations (Fig. 4.2).

INCN Ps-moveout

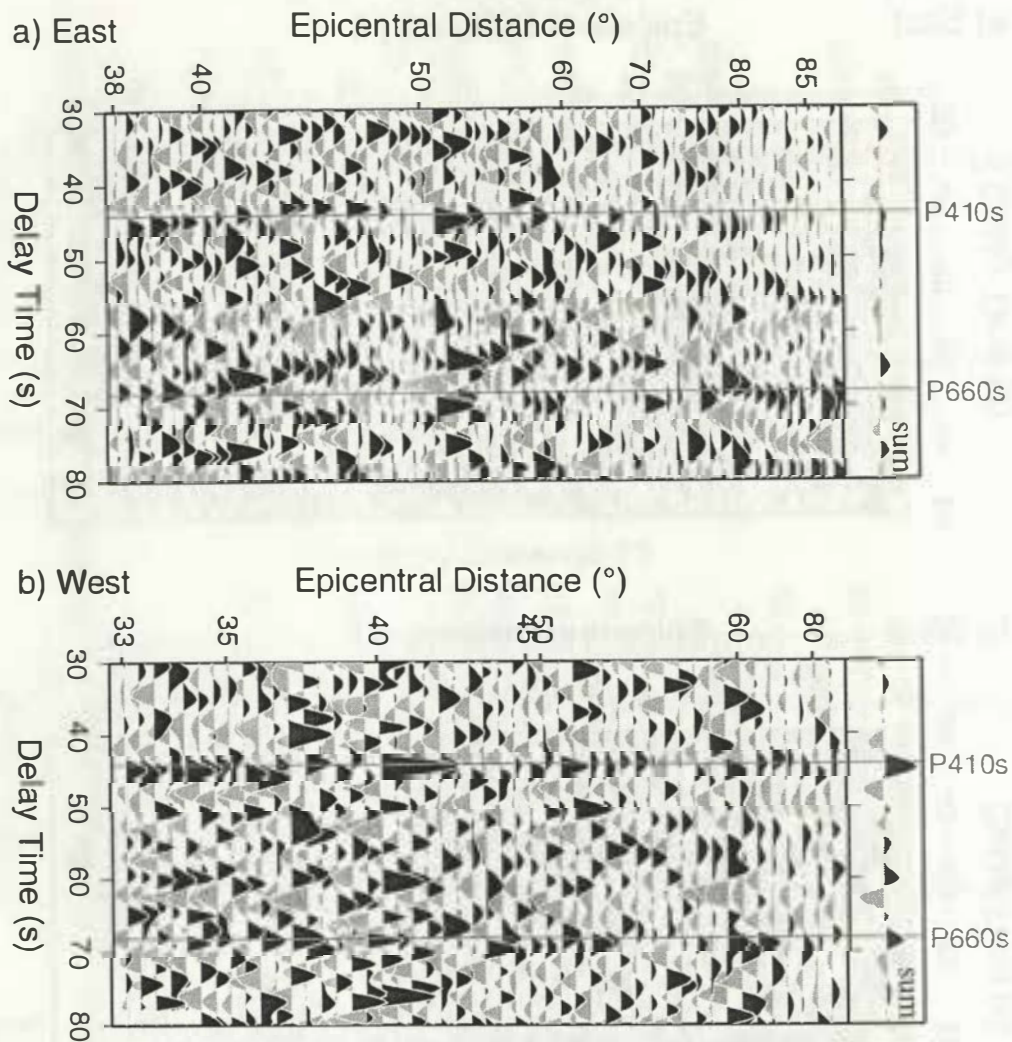


Figure 4.16: Like the case in Fig. 4.15, but for the station INCN.

At station MDJ, the receiver functions are divided into two groups with their back azimuths between 0° – 170° (east side of the station, named “East”), and between 170° – 360° (west side of the station, named “West”). In each group, the traces are moveout corrected and sorted by their epicentral distances (Fig. 4.15). The “sum” trace is the summation of receiver functions in each group. The 410 and 660 conversion phases of the two group are quite different. For the “west” traces, both the 410 and 660 phases are clear in the summation trace as well as in the individual traces and both are later than predicted by the IASP91. In the summation trace their delay times are 46.2 and 71.5 sec, implying the conversion depths to be ~ 430 and ~ 698 km, respectively. The transition zone thickness is about 268 km (25.3 sec), almost 20 km thicker than that of the

IASP91 (250 km). On the "east" traces, however, the 410 phase is absent while the 660 seems to be composed of two discontinuities. The delay times of these two phases are 69 and 74.5 sec in the summation trace, corresponding to the conversion depths of 670 and 730 km, respectively. The 410 and 660 measurements at the "east" (MDJ-e) and the "west" (MDJ-w) side of MDJ are listed in Table 4.4.

Such observations of the 660 beneath MDJ are difficult to explain. One possibility is that the 660 is composed of a "multiple-discontinuity structure" down to a larger depth (Niu and Kawakatsu, 1996) which may be caused by the existence of "non-olivine components" in the mineral phase transformation (Vacher et al., 1996, 1998). Although the upper mantle discontinuities are widely accepted as the phase transformations of the olivine, which is the main component of the mantle, the mineral phase transformation of the remaining mantle components, such as pyroxene and garnet, may also play an important role in some cases, causing seismic discontinuities occurring at different depths.

The individual receiver functions from the station INCN are displayed in Fig. 4.16. Although these traces are noisy, the 410 and 660 phases are visible west of INCN, but they are not observed on the east side (Table 4.4).

Table 4.4: The 410 and 660 beneath the east and the west side of MDJ and INCN

station	t_{410} (sec)	t_{660} (sec)	$t_{660}-t_{410}$ (sec)
MDJ-e	-	69.0	-
MDJ-w	46.2	71.5	25.3
INCN-e	-	-	-
INCN-w	44.8	68.7	23.9

4.4.3 Beneath Japan

The 660

Below Japan the 660 deepening occurs gradually from east to west with the largest topography of 20 km (Fig. 4.6, 4.7 and 4.12). In Fig. 4.9a, however, there is some energy appearing at 720 km depth consistent with the observations of the short-period data (Castle and Creager, 1998). It is possible that this is a local deepening only in the southern part of the sampling region, thus it becomes weak when the data are averaged in a large region (Fig. 4.6).

The 660 phase in southern Japan can be shown in detail with the individual receiver functions at several stations. Fig. 4.17 shows part of the receiver functions from stations JIZ, KIS and ISI. The piercing points of these traces at 660 km depth are within 31°–33°N (Fig. 4.18).

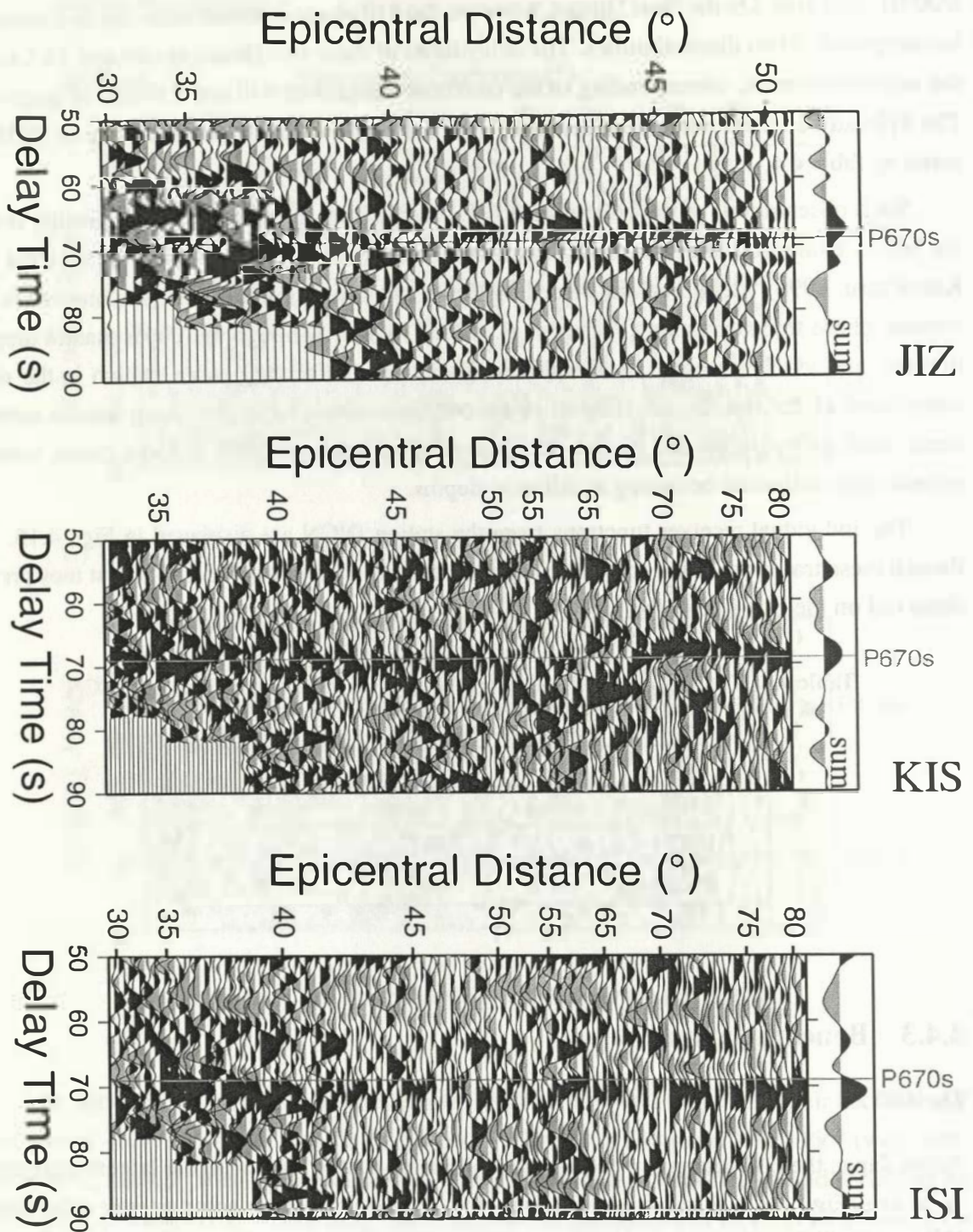


Figure 4.17: Part of individual receiver functions from stations JIZ, KIS and ISI which have piercing points at 660 km depth within 31° – 33° N latitude. The traces are moveout corrected and sorted by their epicentral distances. The “sum” trace of each station is the summation of the individual receiver functions shown here.

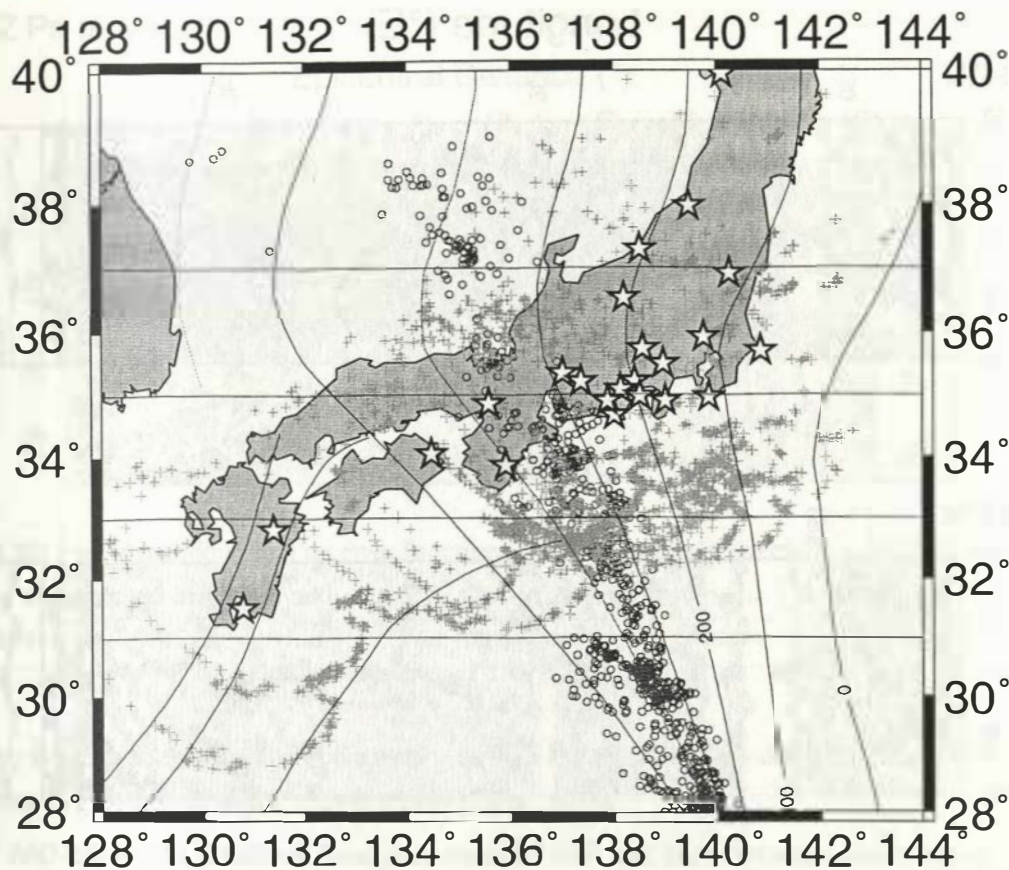


Figure 4.18: Piercing points (crosses) at 660 km depth of the receiver functions from Japanese stations show the sampling region of the data at this depth. Circles are deep (>300 km depth) seismicity with $M_b > 4.5$. The four E-W lines are at latitudes of 31, 33, 35 and 37°N.

The traces are moveout corrected and sorted by their epicentral distances. The “sum” trace of each station is the summation of the traces shown in the figure.

The 660 phase is visible in the individual traces. Its delay time is 67.5, 68.5 and 70.8 sec in the “sum” traces of station JIZ, KIS and ISI, respectively. The discontinuity is at 655, 665 and 690 km depth in the associated region, deepening from east (JIZ) to west (ISI) (see Fig. 4.2). These values are listed in Table 4.5. At JIZ, there is a weak phase with the delay time

Table 4.5: The 660 in the area between 31°–33°N at JIZ, KIS and ISI

station	t_{660} (sec)	the 660 depth (km)
JIZ	67.5	655
KIS	68.5	665
ISI	70.8	690

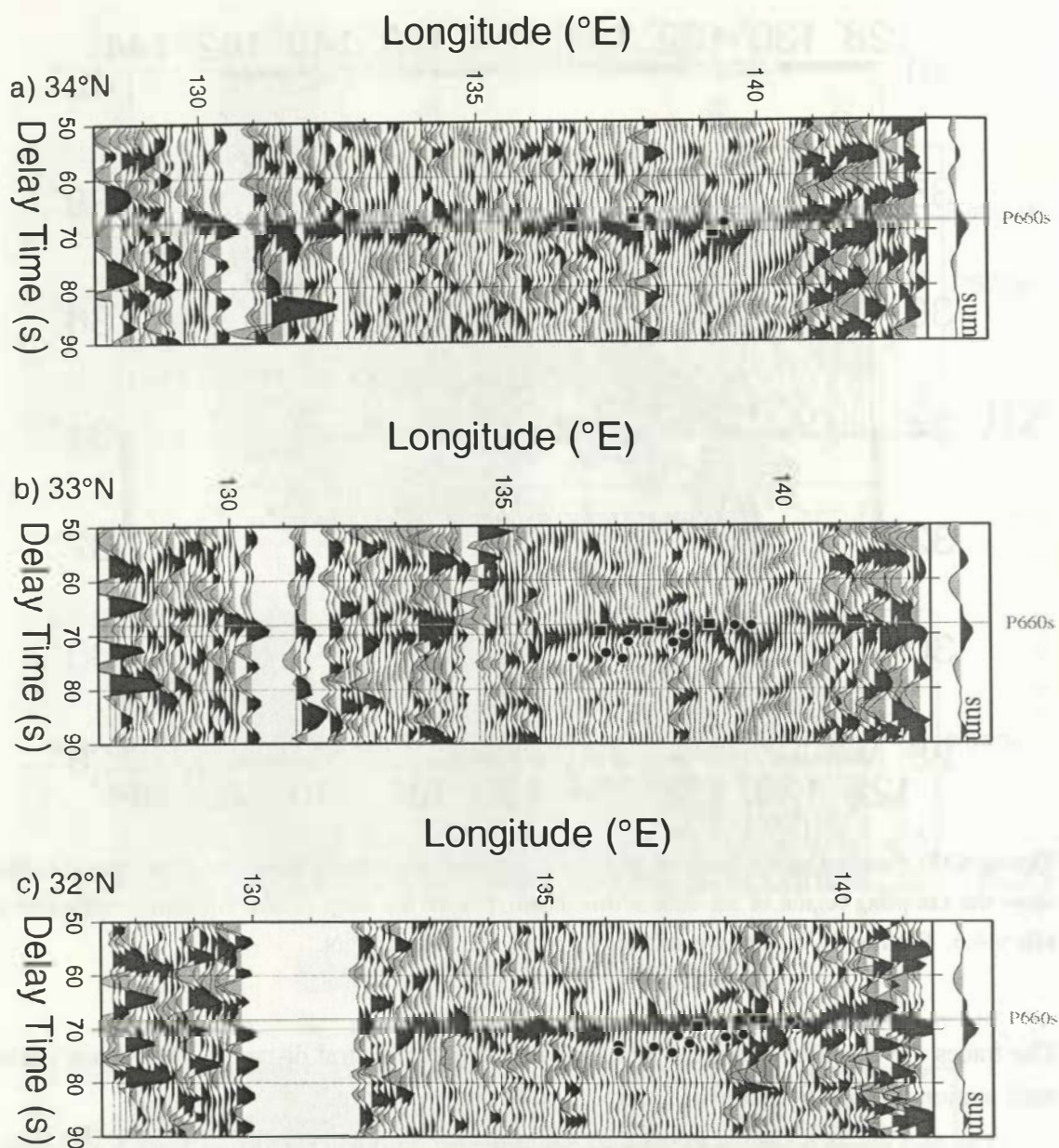


Figure 4.19: Three E-W profiles at the latitudes of 32, 33 and 34°N show lateral variations of the 660 topography beneath southern Japan. Each profile is composed by the projection of the moveout corrected receiver functions which have the piercing points at 660 km depth within 1° to each side of it (see Fig. 4.18). In each profile along the E-W direction, the receiver function are summed within 0.1° longitude bins and without moving average. The “sum” trace of each profile is the summation of the individual receiver functions prior to the longitude stacks. Grey lines labeled “P660s” indicate the calculated 660 delay time in the IASP91 model, with a reference epicentral distance of 67°. Black dots and squares are depth measurements by Castle and Creager (1998) and Collier and Helffrich (1997), respectively, at the corresponding position. These values are transferred into time domain using the IASP91 reference model.

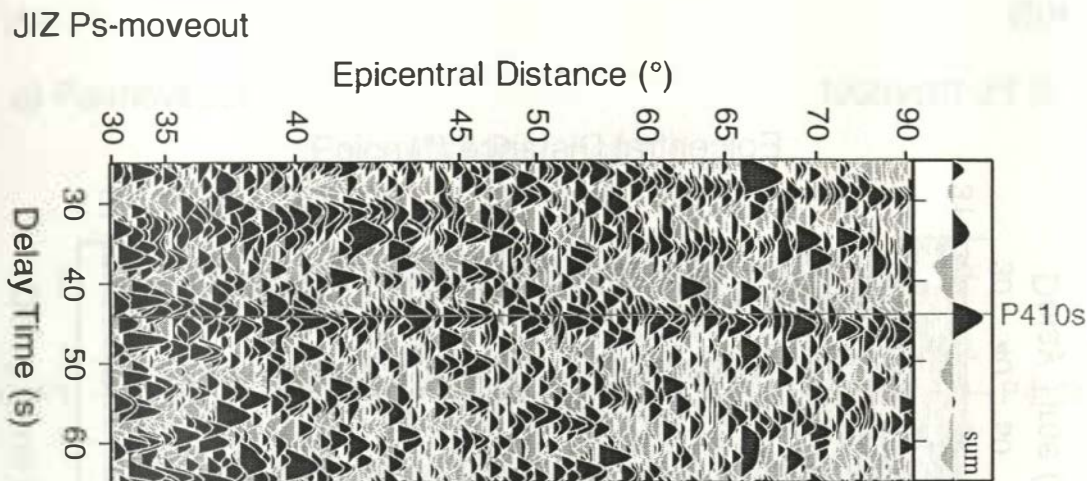


Figure 4.20: Part of the individual receiver functions (back azimuths between 90° – 270°) from the station JIZ. They are moveout corrected and sorted by their epicentral distances. The “sum” trace on the right side is the summation of all individual receiver functions from this station.

of 73 sec corresponding to a discontinuity at 715 km depth. This depth is consistent with the measurements by Castle and Creager (1998) (Fig. 4.9a).

At 660 km depth, receiver functions sample well the area between the latitude 31 – 35° N (Fig. 4.18). To determine the location of the large delay of the P660s at JIZ (73 sec) could come, three E-W profiles at the latitudes of 32 , 33 and 34° N are produced (Fig. 4.19). In each profile along the E-W direction, the receiver functions are summed within bins of 0.1° longitude and 2° latitude. The “sum” trace of each profile is the summation of the individual receiver functions. The 660 depth measurements of Collier and Helffrich (1997) (black squares) and Castle and Creager (1998) (black dots) are transferred into time domain, using the IASP91 reference model, and plotted in the associated profiles (Fig. 4.19).

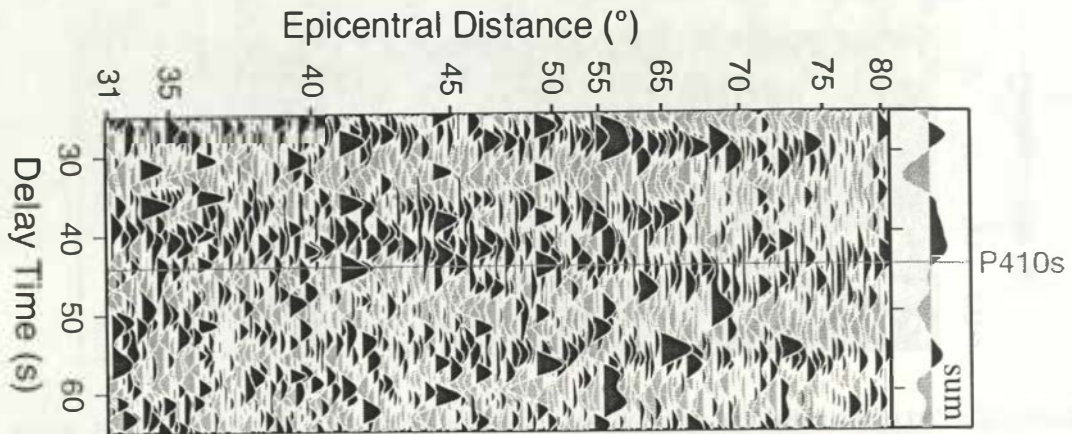
In Fig. 4.19, the major energy of the 660 phase does not show large topographic changes, but there is some weak energy in the two southern profiles at about 73 sec, which seems agree with the measurements of Castle and Creager (1998), implying the possibility of a largely depressed 660 discontinuity further south.

The 410

The stations JIZ, KIS and ISI in southern Japan are located behind, right above and in front of the intersection of the slab with the 410 (Fig. 4.2). Part of the individual receiver functions (back azimuths between 90° – 270°) from these stations are shown in Fig. 4.20, 4.21 and 4.22. These traces have been moveout corrected for Ps or Pps, respectively, and sorted by their epicentral distances. The “sum” trace on the right side of each figure is the summation of all the individual

KIS

a) Ps-moveout



b) Pps-moveout

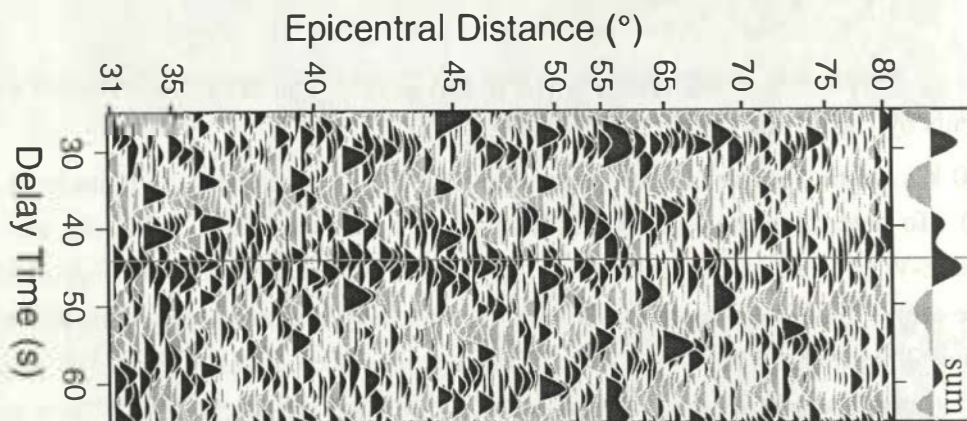


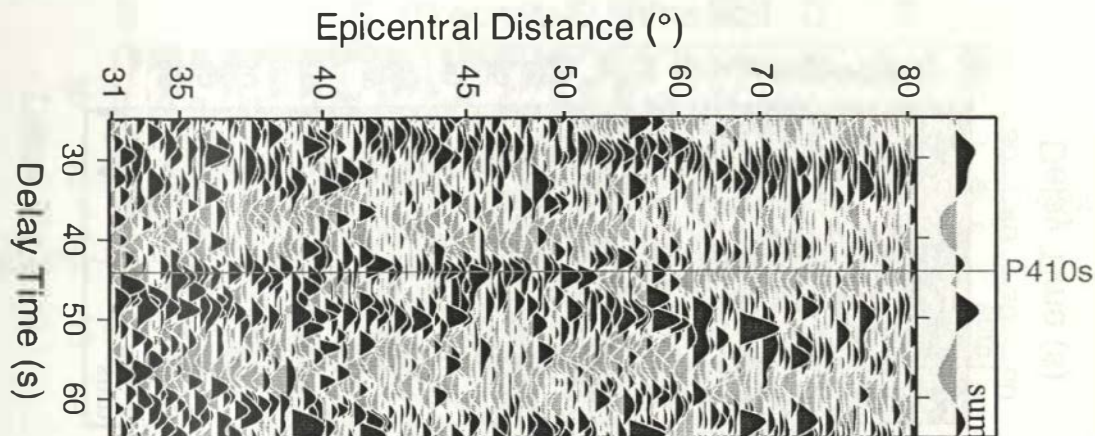
Figure 4.21: Part of the individual receiver functions (back azimuths between 90° – 270°) from the station KIS. They are Ps (on the top) and Pps (on the bottom) moveout corrected and sorted by their epicentral distances. The “sum” traces are the summations of all the individual receiver functions after the associated moveout corrections.

receiver functions from each station.

Receiver functions from JIZ show clearly the 410 phase in the individual traces as well as in the summation trace (Fig. 4.20). The delay time is 44.5 sec (corresponding to 415 km depth) in the summation trace. In the receiver functions from KIS (Fig. 4.21) there is no 410 phase. The phase with 40–50 sec delay time is more likely to be a multiple from another discontinuity at shallower depth other than a direct conversion, since it has a better coherence after a moveout correction for multiples. Station ISI is located at about 90 km west of the intersection of the

ISI

a) Ps-moveout



b) Pps-moveout

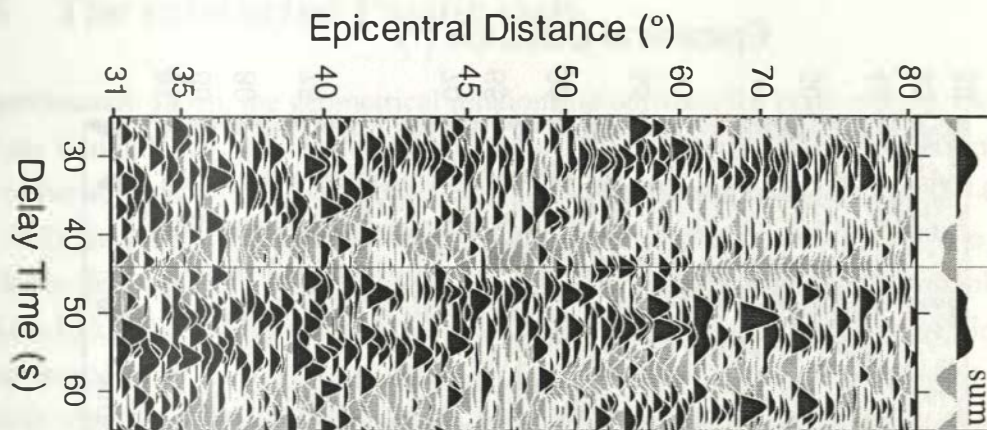


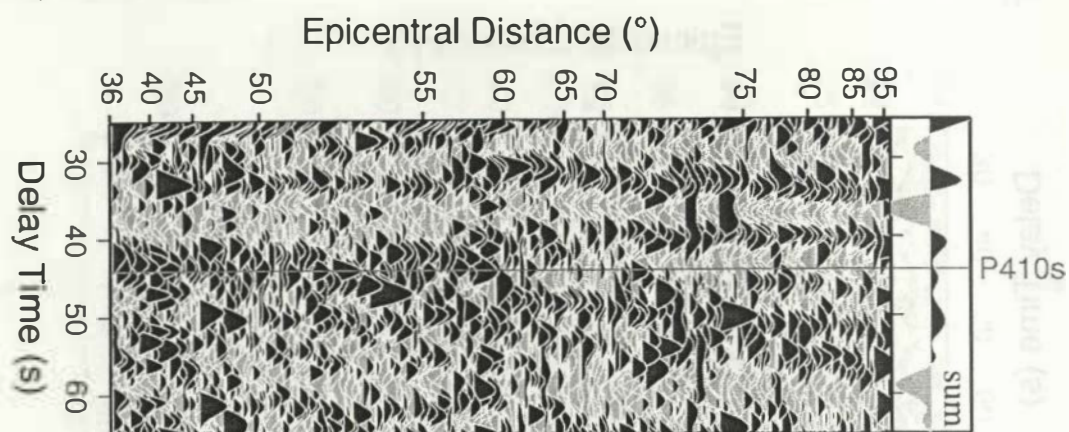
Figure 4.22: Like the case in Fig. 4.21, but for the station ISI.

slab with the 410. The P410s at this station is very weak (Fig. 4.22). On the other hand, there is a phase at 48.5 sec, and it becomes inclined when a multiple moveout correction is applied. Thus, this phase appears to be a direct conversion from a discontinuity at 455 km depth and exists beneath 133.8°E – 135.5°E .

Similarly, receiver functions from the stations in the northern Japan show also variations of the 410. Beneath the station YSS in Sakhalin, the Pacific slab should reach about 400 km depth (Fig. 4.2). Like the case of station KIS, no 410 phase is observed in the receiver functions from this station (Fig. 4.23). However, it is observed in the receiver functions from the station TMR which is located south to YSS. Its delay time is about 42.5 sec corresponding to a conversion from 395 km depth (Fig. 4.24).

YSS

a) Ps-moveout



b) Pps-moveout

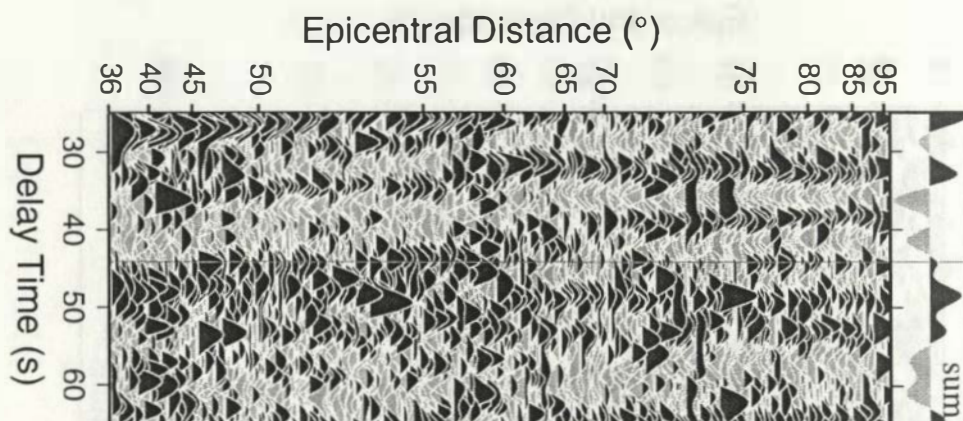


Figure 4.23: Like the case in Fig. 4.21, but for the station YSS.

Table 4.6: The 410 beneath JIZ, KIS, ISI, YSS and TMR

station	t_{410} (sec)	the 410 depth (km)
JIZ	44.5	415
KIS	-	-
ISI	48.5	455
YSS	-	-
TMR	42.5	395

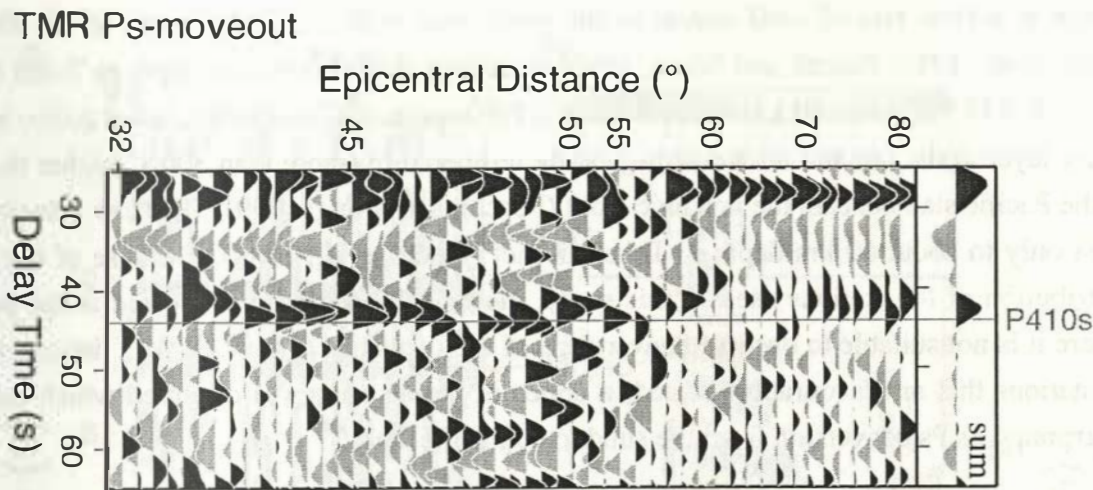


Figure 4.24: Like the case in Fig. 4.20, but for the station TMR.

4.5 The subducted Pacific slab

In northeastern Japan, the geometrical relationship between the plate motion, the Japan trench and arc is simple, i.e., the Pacific plate subducts nearly perpendicular to the Japan trench and the active volcanic front. Beneath Tohoku in northern Honshu (38–40°N and 140–142°E, see Fig. 4.2), the Pacific slab is at 50 km depth under the Pacific coast and at 150 km depth under the Japan Sea coast. The strike is NNE. The upper part of the subducted Pacific plate contains a thin (5–10 km) low-velocity layer (6% lower velocities than the overlying mantle wedge). The upper boundary of the LVZ is sharp and it is located just above the upper part of the double seismic zone (Okada, 1979; Nakanishi, 1980; Hasegawa et al., 1994). The lower part of the slab has a slightly higher V_p of ~ 7.5 km/s (Matsuzawa et al., 1986; Hasegawa et al., 1994).

South of central Honshu, south Kanto to Chubu (34–37°N and 137–141°E, see Fig. 4.1), the strike of Pacific slab changes to NW-SE and the dipping angle to 30°–40° shown by the seismicity and the changing of the direction of the volcanic front (Zhao et al., 1997a). The Philippine Sea plate is underthrust by the Pacific plate. It subducts with small dipping angle, beginning from the Sagami and the Suruga troughs (Fig. 4.1). Beneath Chubu (36°N, 138°E), the configuration of the Philippine Sea plate could not be delineated from hypocentral data because of the lack of seismicity (Ishida and Hasemi, 1988). Strong 3-D effect of the upper mantle structure complicates the observations of the shallow structure. The top of the Pacific slab is not sharp in this region and its surface could be tortuous. A strong low velocity zone in the mantle above the subducting slab is observed beneath the active volcanoes at 100–200 km depth (Hirahara et al., 1989; Zhao et al., 1994).

Beneath southwestern Japan, the Philippine Sea plate is subducting along the Nankai

trough at a slow rate of ~ 40 mm/yr to the north-west with a dipping angle of $10\text{--}30^\circ$ (e.g. Fukao et al., 1983; Peacock and Wang, 1999), reaching about 50–60 km depth in Tokai district (35.5°N , 137.5°E), and 80 km beneath the Kii Peninsular (34°N , 135°E). It has a thin low velocity layer at the top and a relative high plate temperature (more than 300°C higher than that of the Pacific slab beneath the volcanic front (Peacock and Wang, 1999)). The low velocity zone exist only to about 60 km depth in Tokai district (Fukao et al., 1983). Because of the sparse distribution of the stations used in this study, most of the stations are located at the position where it is not suitable to observe conversions of the two slabs (Fig. 4.2). At a limited number of stations that are favourably located, a coherent strong energy is observed which could be interpreted as Ps conversion from the subducted Pacific slab.

4.5.1 North Honshu (station TMR)

Station TMR is located in northernmost Honshu (41.09°N , 141.38°E , see Table 4.2 and Fig. 4.2). There are 62 useful receiver functions at this station, 52 of them have back azimuths between 90° and 270° (Fig. 4.25). These 52 broadband receiver functions are sorted by their piercing points at 80 km depth and stacked within 0.02° longitude bins to form an E-W profile (Fig. 4.25a).

Three phases are seen at shallow depth. The first two have delay times of about 1 and 3.7 sec, corresponding to conversion energy from a very shallow depth and from the Moho, respectively. The Moho (at a depth of about 23 km) is inclined to the east. The third phase has a delay time of 8–11 sec and is inclined to the west. This phase can not be explained as multiples from the two shallow discontinuities, since the first one is too shallow to produce a multiple phase with such a delay time and the multiples from Moho should incline contrary to this phase. Therefore, this phase denotes a real boundary which is inclined to the west.

These receiver functions are migrated from time domain into space domain. To correct the bias of dipping structures, the migration is applied to inclined discontinuities with a 25° dipping angle (Fig. 4.25b). After the migration, the position of this phase is consistent with the hypocenters which are shown by the black dots. Thus, this phase could be explained as the subducted Pacific Moho and the hypocenters seem to be in the mantle part of the oceanic lithosphere.

4.5.2 Central Honshu (stations FUJ, KFU and SGN)

A similar inclined phase can be observed with broadband receiver functions from stations SGN, KFU and FUJ in south Chubu. The locations of the stations are found in Table 4.2 and Fig. 4.2. Fig. 4.26 is produced with the same procedure as for station TMR (Fig. 4.25). The receiver

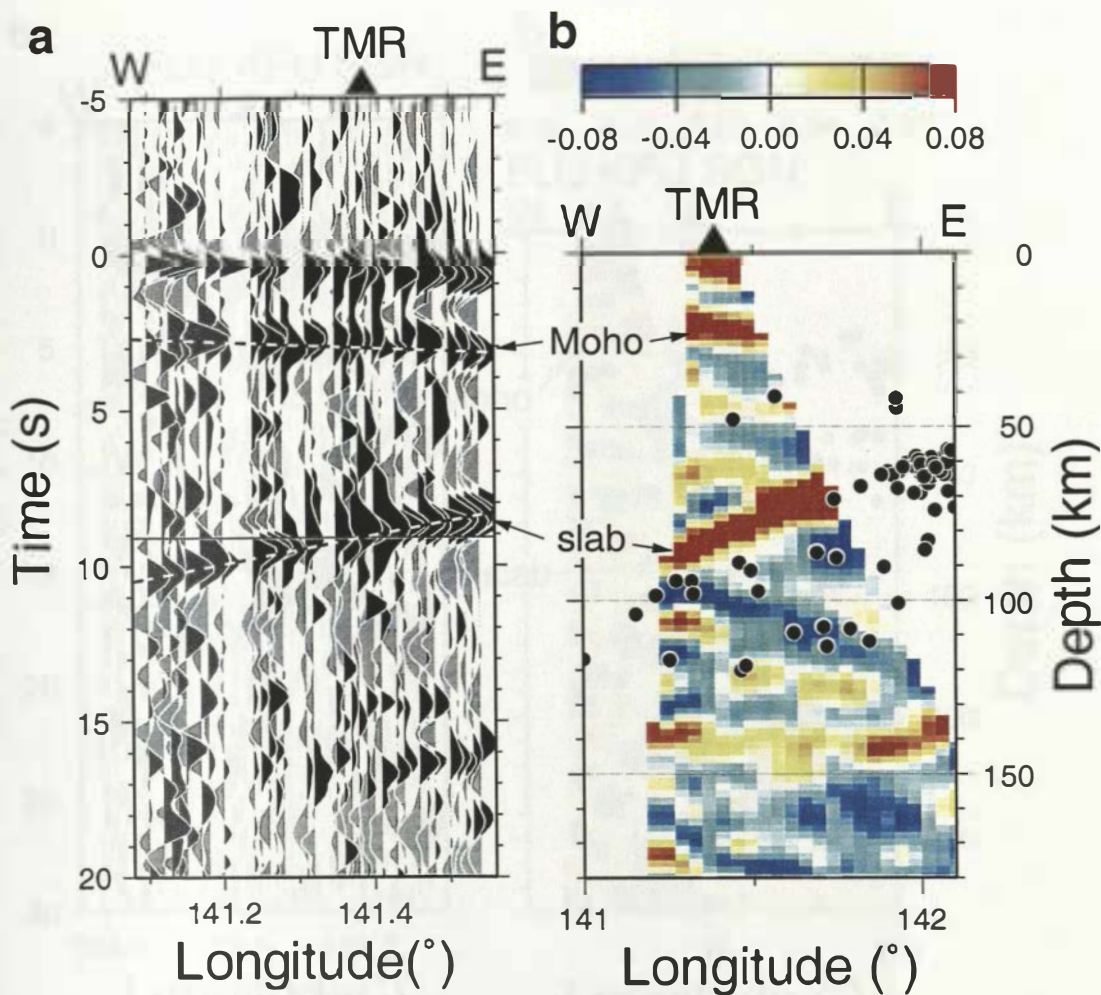


Figure 4.25: a) Broadband receiver functions from the station TMR. They are moveout corrected and sorted by the E-W projection of their conversion points at 80 km depth. Traces within 0.02° longitude bins are stacked. The solid line at about 9.1 sec denotes the delay time of conversions at 80 km depth, calculated with the IASP91 model. The two dashed lines denote the Moho and the slab phases. b) Migration of the receiver functions in a). The migration is applied to inclined discontinuities with a dipping angle of 25° . Black dots denote the hypocenters.

functions are also selected with back azimuths between 90° and 270° , but in Fig. 4.26a the piercing points are calculated at 150 km depth. In Fig. 4.26b, the Moho is at about 40 km depth, the slab phase is consistent with the hypocenters and again the hypocenters seem to be in the subducted Pacific mantle.

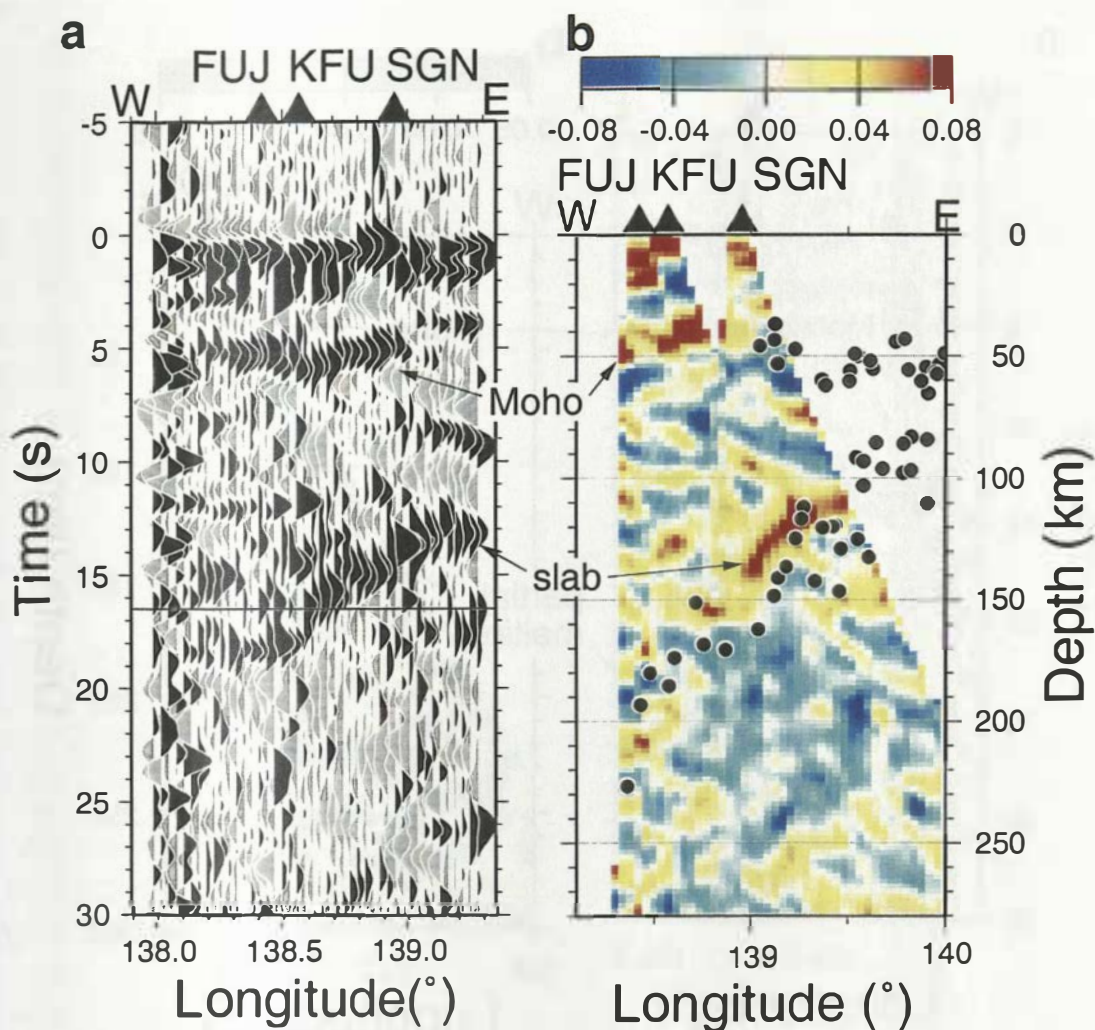


Figure 4.26: Similar to Fig. 4.25, but the receiver functions are from three stations SGN, KFU and FUJ, and in a) the piercing points are at 150 km depth and in b) the dipping angle of the inclined discontinuity model used in the migration is 30° .

4.5.3 The low velocity zone beneath MAJO

According to the slab contour lines (Fig. 4.2), beneath the station MAJO the slab should reach the depth which is similar to that beneath KFU. However, the receiver functions from MAJO do not show a slab phase similar to that observed at KFU. Instead, a strong negative phase appears at 15–25 sec dipping steeply to the east (Fig. 4.27a). This phase could not be the multiple from the Moho (at ~ 40 km depth) because of its large dipping angle. It could not be the multiple from a possible phase which appears at about 8 sec, too, since the multiple of this phase should appear later (at 26 sec).

Receiver functions in Fig. 4.27a are migrated using a model with 40° dipping structure.

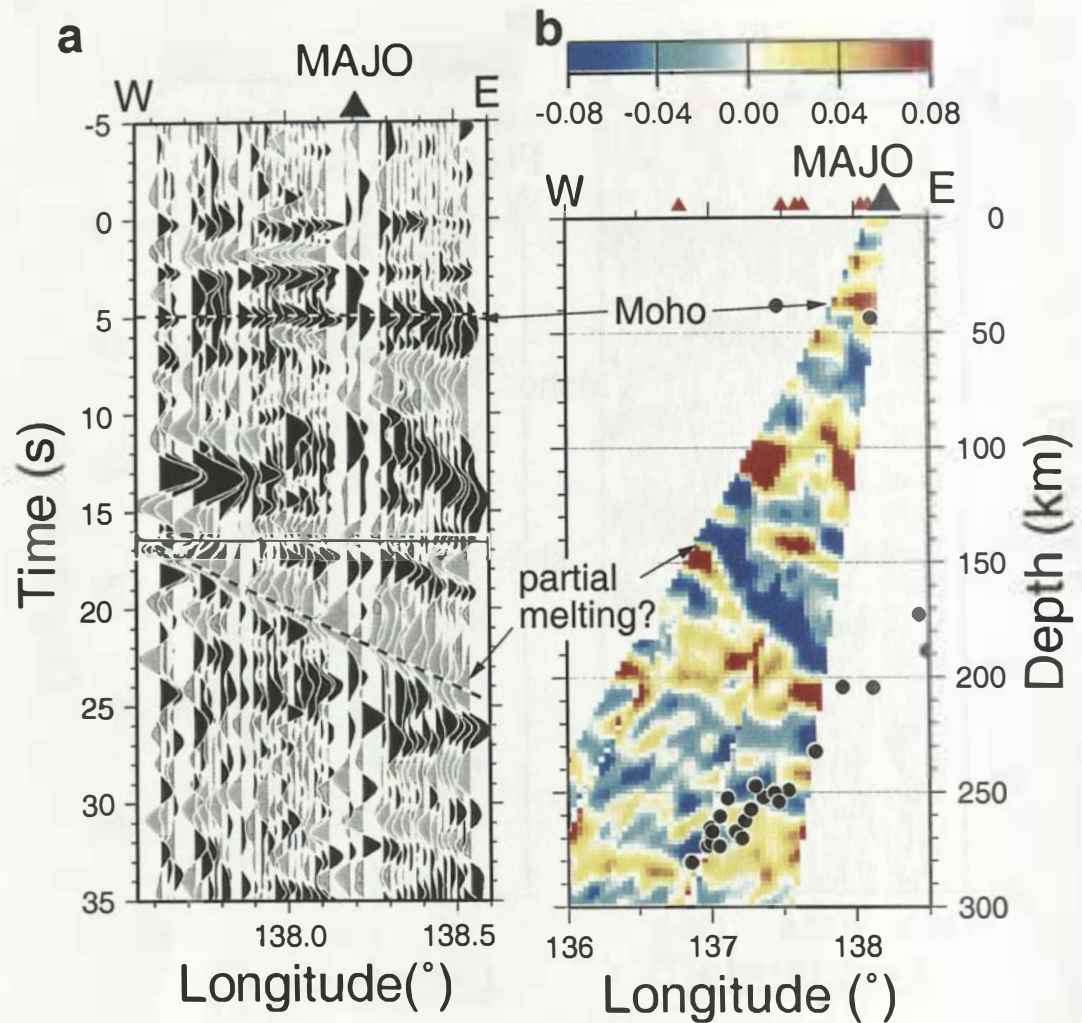


Figure 4.27: Similar to Fig. 4.26, but the dipping of the discontinuity model in the migration is to the east and the angle value is 40° .

After the migration, the negative phase is located right above the subducting slab implied by the hypocenters (Fig. 4.27b). Thus this phase could be related to the partial melting associated with the subduction process.

The following text is extremely faint and largely illegible. It appears to be a multi-paragraph section of a scientific paper or book, likely discussing geological or geophysical aspects of the Northwest Pacific Subduction Zone. The text is oriented vertically on the page, suggesting it may be a scan of a page that was rotated or oriented incorrectly during the scanning process.

Chapter 5

The Hawaiian mantle plume

The Hawaii–Emperor chain consists of approximately 100 volcanic islands, atolls, and seamounts extending from the active volcanic island of Hawaii ~6000 km northwest to the 75–80 Myr old Emperor seamounts near the Aleutian Trench. The younger southeastern part of the chain is situated on the Hawaiian swell, a ~1200 km broad, anomalously shallow region of the ocean floor, extending from the island of Hawaii to the Midway Atoll (~2100 km long) and with a pronounced associated geoid anomaly. The maximum of both the topography and geoid anomaly occurs around the youngest island and both decrease to the northwest.

The volcanic edifice of the Hawaiian islands and seamounts, as well as the surrounding area of shallow sea floor (the Hawaiian swell), are believed to result from the passage of the oceanic lithosphere over a mantle hotspot (Wilson, 1963; Morgan, 1971; Morgan et al., 1995). The Hawaiian plume is proposed to originate from lower mantle (Morgan, 1971; Ji and Nataf, 1998), or even above the core-mantle boundary (Russell et al., 1998). Hot material would rise from the root, move up within a narrow stem (conduit) of the mushroom form of a plume through the upper mantle (Nataf, 2000). The radius of the conduit could be only 100–200 km, and the excess temperature within the plume is expected to be ~200°C. At shallow depth (<200 km), plume material may spread laterally over more than 1000 km, yielding a low velocity anomaly.

This model predicts a topographic anomaly of the 410 and 660 in the immediate vicinity of the plume conduit, with scales of a few hundred kilometers. The magnitudes of the anomaly should be determined by the thermal nature of the phase boundaries and the excess temperature of the plume, i.e. for a 200°C excess temperature the 410 would be depressed by less than 10 km (Akaogi et al., 1989) and the 660 would be uplifted by 10–20 km (Shearer and Masters, 1992). Overall, the transition zone would be 20–30 km thinner.

However, in layered mantle convection models, plumes may arise from regions above the base of the upper mantle. In this scenario, heating of the 660 by the underlying lower mantle (Kellogg, 1991) could effect a large horizontal extension of the boundary layer (the 660) much

exceeding the diameter of the mantle conduit. Thus, the reduction of the 660 depth would occur over a broad region. Since the 410 depression should be narrow and small, a broad transition zone thinning would be caused mainly by the 660 uplift. If the mantle convection is strongly layered, plumes arise from the instabilities in a global thermal boundary layer at the base of the upper mantle (Nakakuki et al., 1994), the lateral excess temperature at the base of the 660 boundary layer would be generally less than the excess temperature of the plume (Richter and McKenzie, 1981; Nakakuki et al., 1994). The 660 depth would thus be nearly constant. In this case, the transition zone thickness would remain constant in most of the region, except within the plume conduit where it could be reduced because of the deepening of the 410.

The topography of the 410 and 660 beneath Iceland in the vicinity of a mantle plume was studied with receiver functions (Shen et al., 1998b). Beneath northern Iceland, both the P410s and P660s are delayed relative to IASP91 because of the velocity reduction at depths shallower than 410 km. Beneath central to southern Iceland their differential delay time is reduced by as much as 2.2 sec, corresponding to a ~ 20 km thinning of the transition zone. The temperature anomaly is suggested to be 150°C within 200 km radius centered beneath central and southern Iceland, indicating the existence of a thermal upwelling originating from the lower mantle.

Another receiver function study (Dueker and Sheehan, 1997) shows that beneath the Yellowstone hotspot, a 20–30 km reduction of the transition zone thickness occurs over a width of 200–300 km, which could result from a lateral temperature increase of 250°C . The warmest mantle resides not beneath the Yellowstone hotspot track, but 150 km to the southeast along the easternmost edge of the active Basin and Range faulting.

The existence of a thermal mantle plume beneath Hawaii is indicated by geochemical and gravity observations (Hofmann, 1997; Watson and McKenzie, 1991; Ribe and Christensen, 1994). Direct seismic observations of the 410 and 660 topography are, however, few. With observations of long-period SS precursors, Shearer (1991, 1996) indicate that the thickness of the mantle transition zone in most of oceanic areas is unlikely to vary significantly, Gossler (1995) observed an about 10 km reduction of the transition zone thickness beneath central Pacific ocean. However, the long-period data they used could not resolve well the topographic anomaly of the 410 and 660 around a plume because of the expected small-scale signature of the both discontinuities (less than a few hundreds of kilometers broad) (Chaljub and Tarantola, 1997). There are no deep earthquakes beneath Hawaii to support any works of high-frequency near-source conversions.

Tomographic studies have been applied to detect velocity anomalies in the mantle which might be related to the Hawaiian plume, but because of the scarcity of local seismic stations, the resolution is generally poor. The resolution of a S-wave tomographic model by Grand (1994) is larger than 1000 km at transition zone depth, this model is thus not appropriate for imaging a plume structure. In the lower mantle, the resolution power of global tomographic work (e.g.

Grand, 1994; Bijwaard et al., 1998) is limited and becomes worse for slow and cylindrical objects such as plumes and the lower mantle beneath Hawaii is not resolved at all down to a depth of about 2000 km (van der Hilst et al., 1997). However, in a recent work of diffraction tomography, Ji and Nataf (1998) found that in the Pacific Ocean a high level of scattered energy seems to come mostly from a spot situated a few degrees northwest of Hawaii. Also, in the lowermost mantle evidence has recently been given that immediately above the core-mantle boundary southwest to Hawaii, there are strong lateral gradients in shear-wave velocity and anisotropic shear-wave polarization direction over distances of only several hundred kilometers, indicating an origin of the Hawaiian plume (Russell et al., 1998).

In the uppermost mantle, a global 3-D tomographic model of shear-waves (Ekström and Dziewonski, 1998) shows that beneath the central Pacific Ocean there is a complicated structure with large anisotropy centered near Hawaii. Lithospheric thickness is estimated to be ~ 70 km beneath the island of Oahu from converted body waves (Bock, 1991), and 85–100 km from Rayleigh wave dispersion to the northwest of Oahu (Woods et al., 1991; Woods and Okal, 1996) and between the islands of Hawaii and Oahu (Priestley and Tilmann, 1999). This lithospheric thickness differs little from the thickness of 80–90 Myr undisturbed oceanic lithosphere (Nishimura and Forsyth, 1988). The velocities are estimated to be 4.5–4.6 km/sec in the lithosphere and to be 4.0–4.1 km/sec in the low velocity zone (Bock, 1991; Woods et al., 1991; Woods and Okal, 1996; Priestley and Tilmann, 1999). In a pilot experiment southwest of the Hawaii island, surface waves recorded by an ocean-bottom seismic array show strong lateral velocity variations across the array. Within roughly 300 km of the island chain there is a significant velocity reduction in the asthenosphere below 130 km (Laske et al., 1999).

5.1 Data

In this chapter, the receiver function technique is used to derive the upper mantle structure beneath the islands of Oahu and Hawaii (Fig. 5.7). On Hawaii, data are collected from a network of 6 temporary broadband stations deployed in 1995 and 1996, which were operated jointly by the University of Cambridge and the US Geological Survey (Priestley and Tilmann, 1999). Each station has a Guralp CMG-3T sensor. The seismic signals are telemetered to the Hawaiian Volcano Observatory where the data are recorded. There are 151 available receiver functions from 36 earthquakes recorded at 6 stations. Records of each event from the stations are summed since these stations are separated by less than 10 km, and therefore the summation trace is considered to be a record of a single pseudo-station which is referred as HIBSN (Hawaiian Island Broadband Seismic Network). The locations of these stations are listed in Table 5.1. The 36 earthquakes are plotted in Fig. 5.1. The distributions of their back azimuths and epicentral distances and histograms of the focal depths and magnitudes are shown in Fig. 5.2.

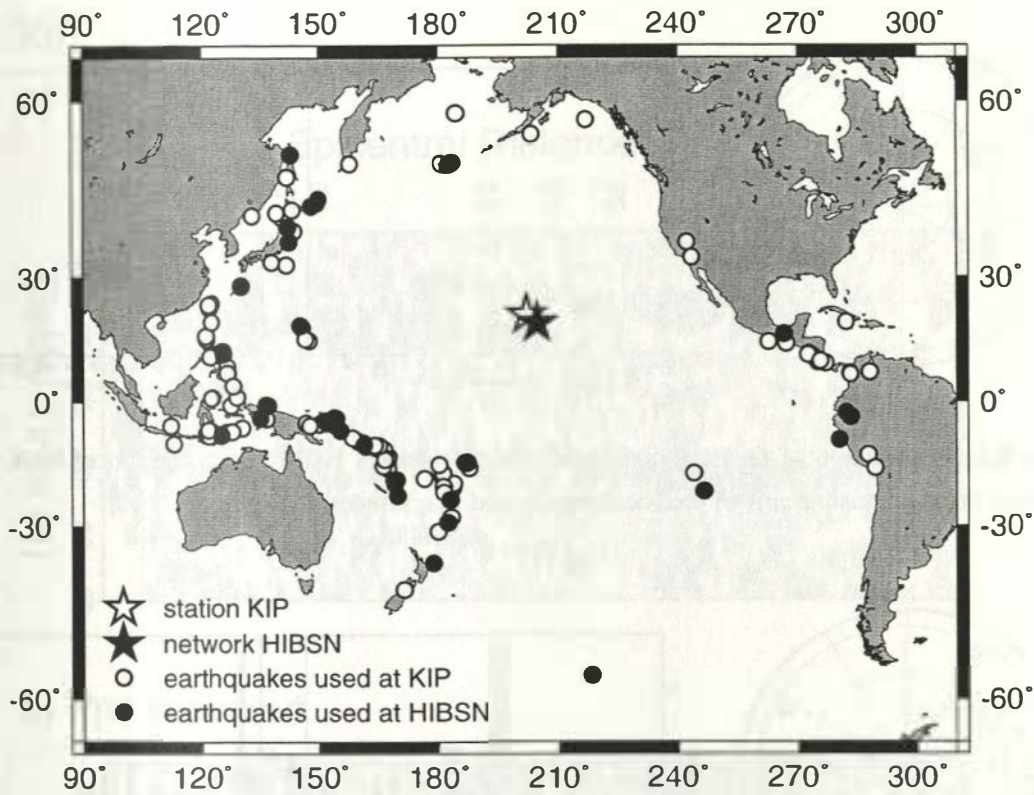


Figure 5.1: Teleseismic earthquakes used for station KIP and the temporary network HIBSN

The IRIS/GEOSCOPE broadband station KIP is located on the island of Oahu. Receiver functions from 104 teleseismic earthquake recordings (plotted in Fig. 5.1) are used. The information about these earthquakes are shown in Fig. 5.3

Table 5.1: Hawaii temporary broadband Stations

Code	latitude (°)	longitude (°)	number of RFs
GU2	19.406	-155.332	34
GU3	19.427	-155.258	14
GU4	19.440	-155.310	24
GU5	19.406	-155.332	30
GU7	19.364	-155.317	19
GU9	19.398	-155.266	25
HIBSN	19.41	-155.29	36

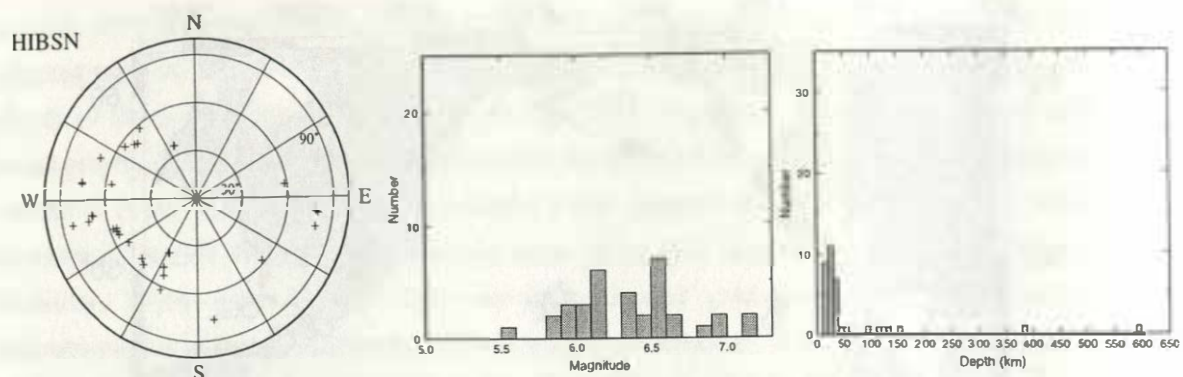


Figure 5.2: Information of the earthquakes used at the station HIBSN: distribution of back azimuth-epicentral distance; histograms of the focal depths and magnitudes.

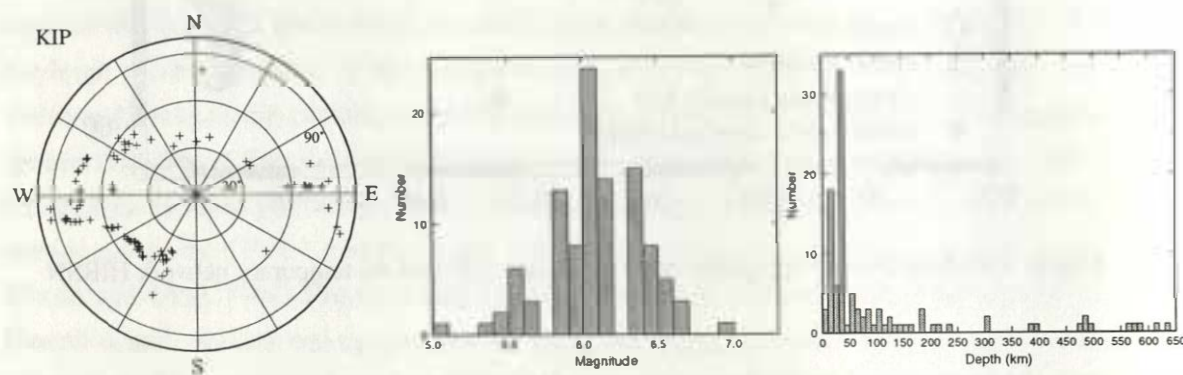


Figure 5.3: Information of the earthquakes used at the station KIP: distribution of back azimuth-epicentral distance; histograms of the focal depths and magnitudes.

5.2 Topography of the 410 and 660

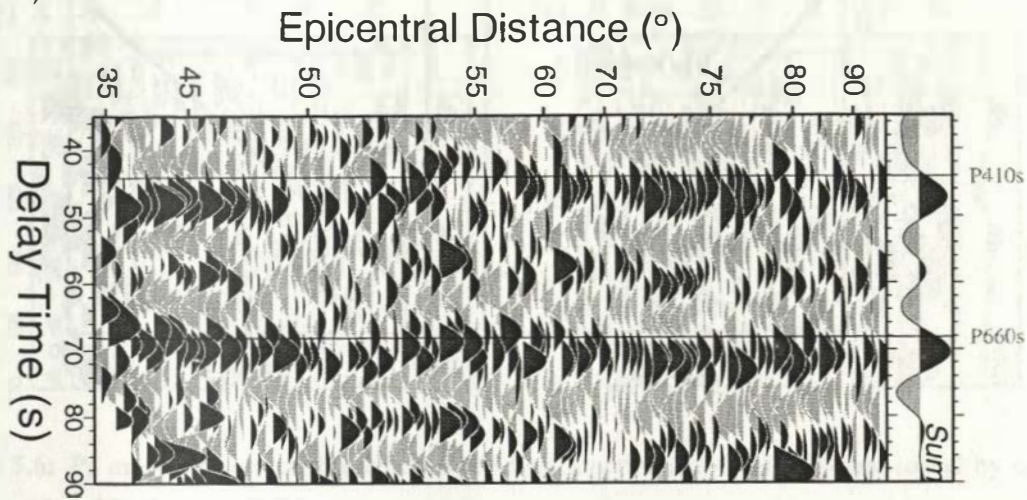
5.2.1 Beneath the island of Oahu

Individual receiver functions from station KIP are shown in Fig. 5.4 (after 10 sec low pass filter). They are moveout corrected for Ps (a) and multiples (b) respectively, and sorted by epicentral distance. The phases at times of 47.2 and 70.4 sec in the summation trace in Fig. 5.4a are direct conversions at the 410 and 660, since they become inclined after a moveout correction for multiples (Fig. 5.4b). Both phases are later than the global averages (44.1 and 68.1 sec for IASP91, at 67° epicentral distance). Their differential time is 23.2 sec (23.9 sec is obtained by Vinnik et al. (1997)), suggesting that the transition zone thickness is only slightly less than the global average (24 sec in IASP91).

Similar to the observations in northern Iceland (Shen et al., 1998b), both delayed P660s

KIP

a) Ps-moveout



b) Pps-moveout

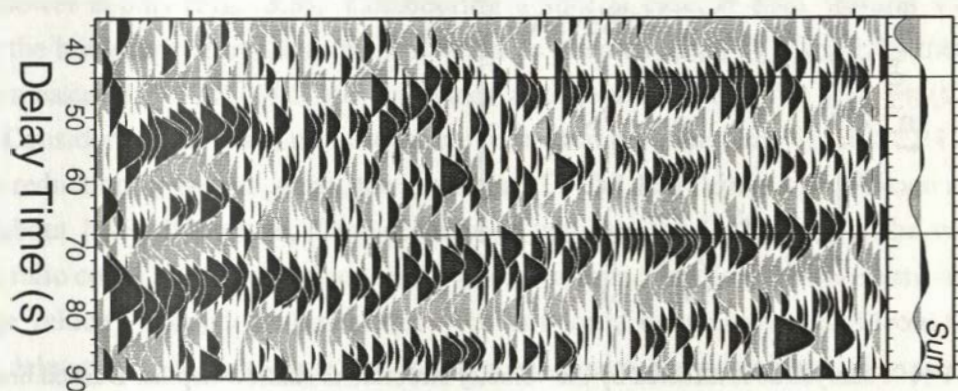


Figure 5.4: Individual receiver functions from KIP have been moveout corrected according to phases of Ps (a) and Pps (b), respectively, and sorted by the epicentral distance. The “sum” traces are the summations of the individual traces. Thin lines mark the times of Ps phases calculated for the IASP91 model.

and P410s phases observed at KIP could be caused by the low velocity anomalies at shallow depth (less than 410 km), since the transition zone thickness is almost not influenced. Modeling of melting parameter of the Hawaiian plume (Ribe and Christensen, 1999) shows that due to the motion of the Pacific plate, the thermal anomaly could have a large extension along the axis of the swell to the northwest. Beneath KIP, which is about 600 km away from the assumed plume center around the island of Hawaii, the hot material ($>1400^{\circ}\text{C}$) could exist to a depth of more than 140 km and at 100 km depth its lateral extension could be more than 800 km across the

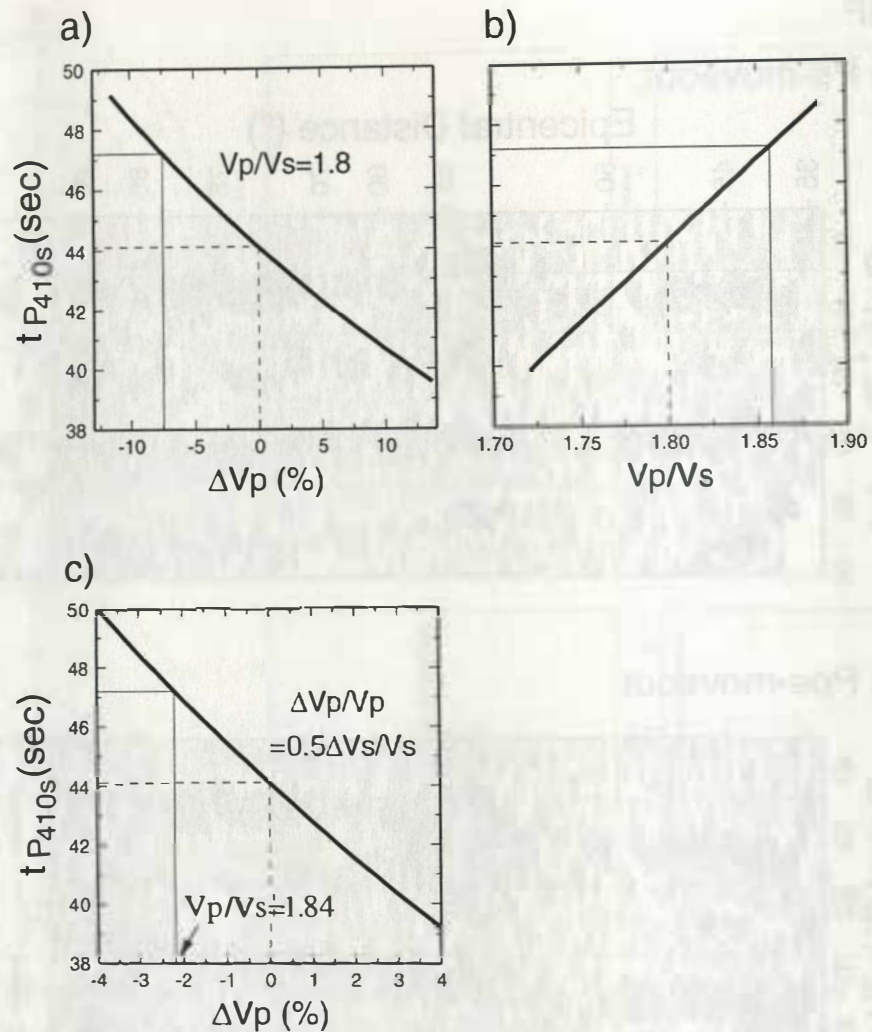


Figure 5.5: P410s delay time is affected by the velocity structure at shallow depths. Dashed lines indicate the values for the IASP91 model. Thin lines indicate the measured values from receiver functions on the station KIP. a). Both the Vp and Vs vary but the Vp/Vs ratio keeps constant (1.8); b). The Vp/Vs ratio varies because of the changing of the Vs ; c). For hot material, the reduction of the Vs is supposed to be two times larger than that of the Vp . To cause the delayed P410s measured at KIP, the reduction of the Vs should be more than 2% with $Vp/Vs = 1.84$.

swell. The hot material at shallow depths could reduce the Vp and Vs significantly, causing in both delayed 410 and 660 phases. If the mantle plume has a mushroom form (Nataf, 2000), at the transition zone depths, the lateral temperature anomaly will be limited in the immediate vicinity around the plume conduit. The topography of the thermal discontinuities (the 410 and 660) as well as the transition zone thickness will not be affected in the area outside this region.

The delayed P410s and P660s times could be used to discuss the reduced average velocities

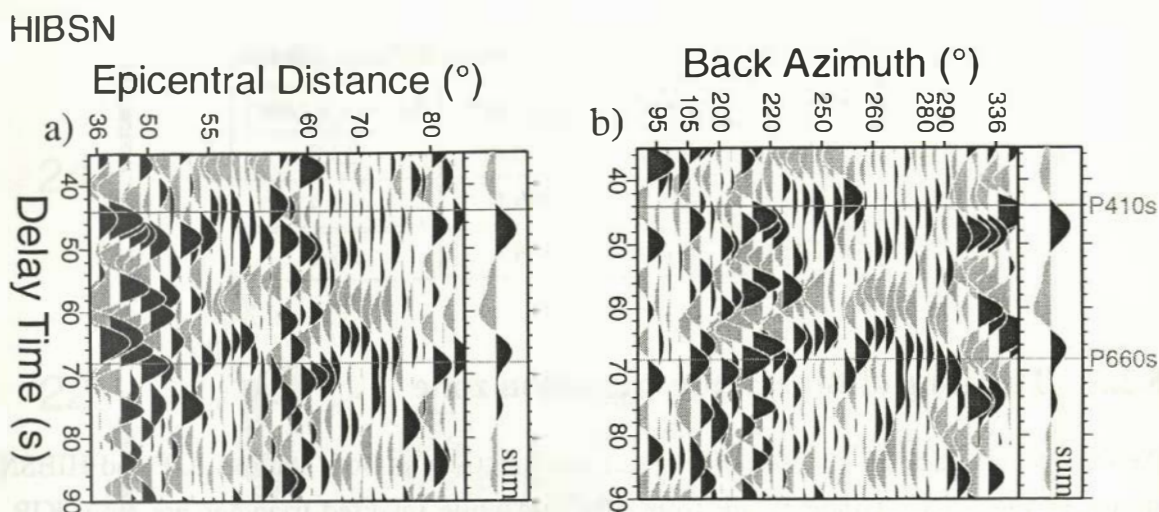


Figure 5.6: Ps moveout corrected individual receiver functions from HIBSN are sorted by epicentral distance (a) and back azimuth (b).

at shallower depths (Fig. 5.5). Considering a special case, if both V_p and V_s are reduced due to the hot temperatures, but the V_p/V_s ratios keep constant ($V_p/V_s=1.8$), then the delayed P410s measured at KIP (47.2 sec) indicates a large decrease of V_p and V_s (to 7.5%) (Fig. 5.5a); Considering that V_s is more sensitive to the temperature than V_p , if the P410s is delayed by the reduction of the V_s alone, the measured P410s delay time will indicate a large V_p/V_s ratio (about 1.86). Therefore, if the correlation between the V_p and V_s or the variation of the V_p/V_s ratio could be further constrained by, for example, petrological observations, the reduced average velocity at depth shallower than 410 km could be well estimated from the P410s and P660s delay times. If we assume that in the hot material, the percentage reduction of V_s is two times larger than that of V_p (Sobolev, personal communication), then the 47.2 sec delay time of the P410s which is observed at KIP, could result from about 2% reduction of V_p , 4% reduction of V_s and the V_p/V_s ratio could reach 1.84 (Fig. 5.5c).

5.2.2 Beneath the island of Hawaii

The 36 individual receiver functions from HIBSN (after 10 sec low pass filter) are moveout corrected and sorted by epicentral distance (Fig. 5.6a) and back azimuth (Fig. 5.6b). In the individual traces, both the 410 and 660 phases are weak and scattered. The P660s is earlier on the traces with back azimuths of about 260° (Fig. 5.6b). In the summation trace the two phases are clear and their delay times are 47.2 sec and 66.6 sec. Unlike the case at KIP, the P660s at HIBSN is earlier than predicted by IASP91. The differential time of the P660s and P410s is 19.4 sec, indicating a thinning of the mantle transition zone at HIBSN.

Table 5.2: The 410 and 660 beneath KIP and HIBSN

station	t_{410} (sec)	t_{660} (sec)	$t_{660}-t_{410}$ (sec)
KIP	47.2	70.4	23.2
HIBSN	47.2	66.6	19.4
IASP91	44.1	68.1	25.0

5.2.3 Thinning of the mantle transition zone

Piercing points at 660 km depth of the receiver functions at both stations KIP and HIBSN are shown in Fig. 5.7. Triangles are from HIBSN, while inverted triangles are from KIP. The color code and size of the symbols indicate the observed differential delay times between P660s and P410s, measured from the individual receiver functions of these two stations. Where both phases have been observed and differential times could be measured in individual traces, these times are indicated in Fig. 5.7. Yellow piercing points indicate a thinner (hotter), and blue ones a thicker (cooler) transition zone, respectively, than the average KIP value of 23.2 sec. A concentration of yellow piercing points (hot material) is found within a radius of 200 km (green circle) from a center (-157.4°E, 18.6°N). This observation is robust since the traces within the circle are obtained at two different stations with different ray paths in the upper mantle.

All receiver functions from HIBSN and KIP are sorted again by the radial distance of their piercing points at 660 km depth from this center, and plotted in Fig. 5.8. The P660s in these receiver functions, which have the piercing points within the green circle in Fig. 5.7, are marked green, indicating an updoming of the 660.

This center is assumed to be the plume center at that depth, but due to the lack of data right beneath and to the southeast of HIBSN, the size of the plume is not well constraint. Within the green circle the differential delay time of the P660s and P410s is averaged to be 3–5 sec smaller than the global average (24 sec at 67° reference epicentral distance for IASP91). The corresponding 30–50 km thinning of the transition zone could be caused by 200–350°C higher temperature than the surrounding mantle (Fig. 5.7). In Fig. 5.8, the differential times of P660s and P410s in the summation traces are 4 sec smaller at HIBSN than at KIP, implying an excess temperature of about 300°C within the transition zone beneath HIBSN. This temperature anomaly could be caused by the Hawaiian plume at the mantle transition zone depth.

From receiver function data, the largest temperature anomaly at mantle transition zone depth is suggested to be located several hundred kilometers to the south-southwest of the Hawaiian island (see the green circle in Fig. 5.7). Similar observations have been made in Yellowstone hotspot area and Iceland, in which the largest transition zone thinning was reported to occur 150 km southeast to the Yellowstone hotspot track (Dueker and Sheehan, 1997) and be-

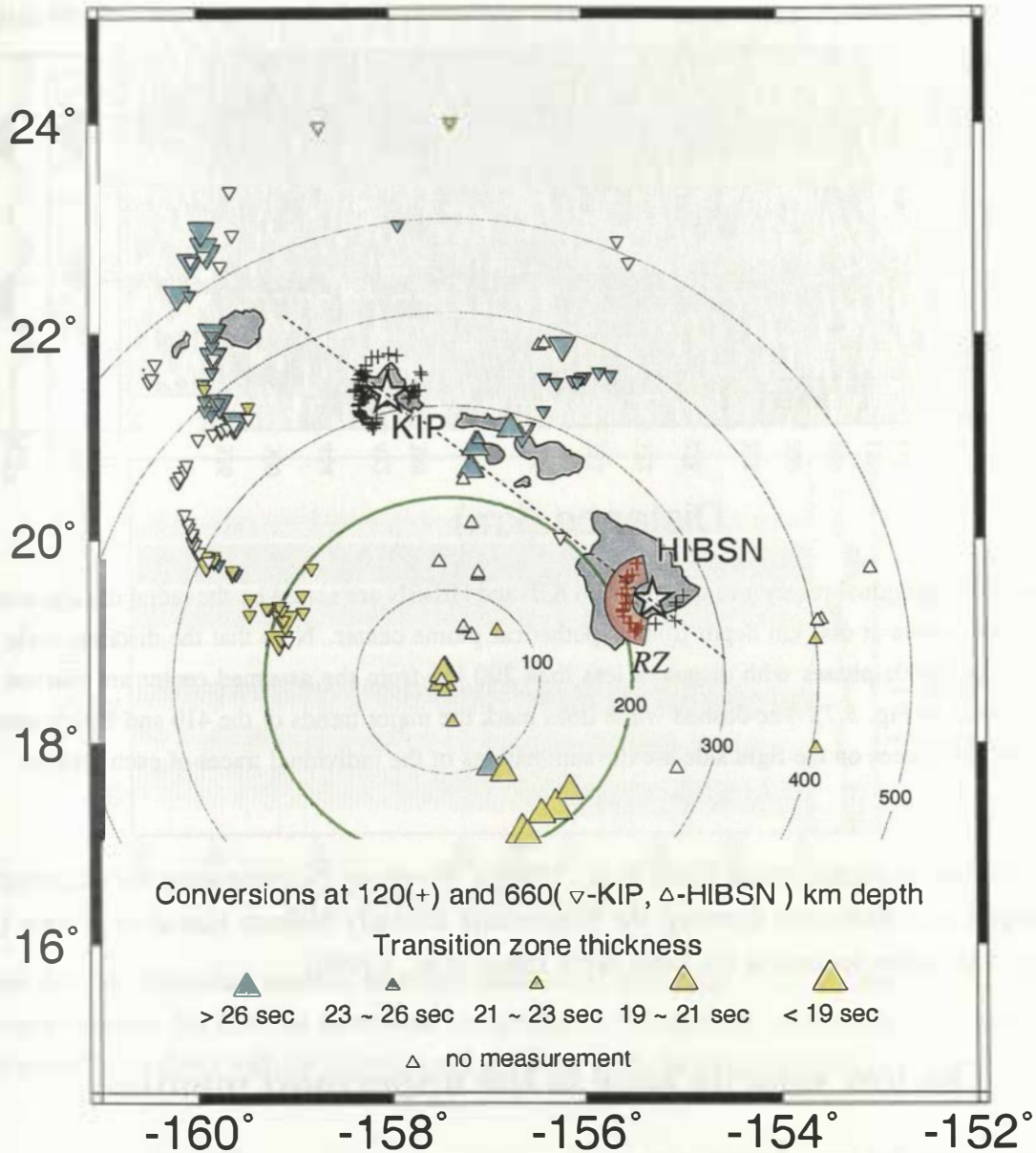


Figure 5.7: Location map of the broadband seismic stations KIP on Oahu and HIBSN on Hawaii and of the piercing points of Ps converted seismic phases at 120 and 660 km depth. The color code and size of the 660 piercing points indicate the observed differential times between P660s and P410s measured from the individual receiver functions which are Ps moveout corrected (Fig. 5.4 and 5.6). Yellow piercing points indicate a thinner (hotter) and blue ones a thicker (cooler) transition zone than the average KIP value of 23.2 sec (Vinnik et al. (1997) obtained 23.9 sec). A concentration of yellow piercing points (hotter material) is found south to southwest of HIBSN with a diameter of about 400 km. Within this region, the green marks a confined region of clear updoming of the 660 (see Fig. 5.8). The red zone in the center of Hawaii marks a region in the asthenosphere between about 130 and 170 km depth where Vs is strongly reduced (see Fig. 5.11 in next section).

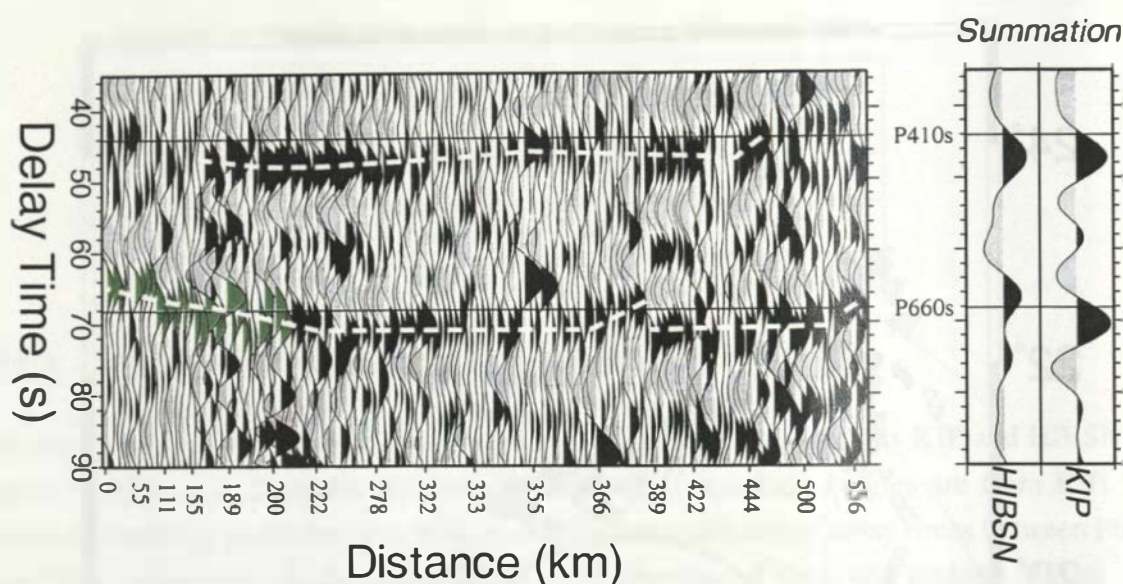


Figure 5.8: Individual receiver functions from KIP and HIBSN are sorted by the radial distances of their conversion points at 660 km depth from hypothetical plume center. Note that the distance scale is not linear. The P660s phases with distances less than 200 km from the assumed center are marked green (green circle in Fig. 5.7). The dashed white lines mark the major trends of the 410 and 660 phases. The “summation” traces on the right side are the summations of the individual traces of each station.

neath central to south Iceland (Shen et al., 1998b). However, by comparing the magnitudes of the largest transition zone thinning, the temperature anomaly beneath Hawaii is at least 100°C higher than below Iceland at the same depth (Shen et al., 1998b).

5.3 The low velocity zone in the uppermost mantle

In this section I’ll concentrate on the structure in the uppermost mantle. The structure in the crust is not discussed because of strong scattering in the data. To get a stable waveform for the signals from the uppermost mantle, a 5 sec low pass filter is applied to the receiver functions.

5.3.1 Island of Oahu

Individual receiver functions from station KIP are sorted by epicentral distance (Fig. 5.9a). To study the velocity structures at depths shallower than 200 km, receiver functions are shown within 35 sec delay times. In Fig. 5.9a, the Moho phase is clearly seen at about 2.5 sec in both the individual and summation traces and it is followed by a negative phase at about 8 sec (marked by “LVZ”). This negative phase can be reasonably interpreted as boundary of litho-

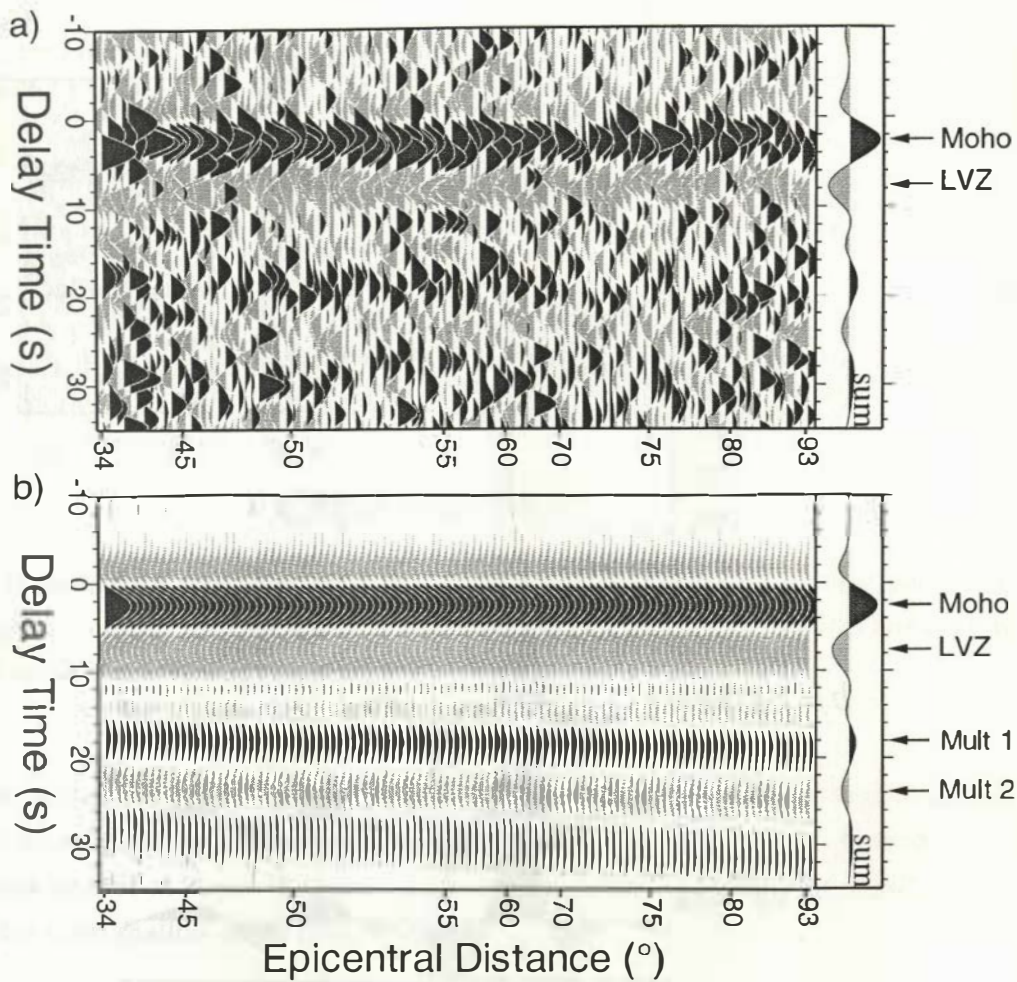


Figure 5.9: a). Individual receiver functions observed at KIP (after 5 sec low pass filter), sorted by epicentral distance. No moveout corrections are applied; b). Comparable synthetic receiver functions of “KIP model”, calculated with the slowness and incidence angle values of the data.

sphere and asthenosphere at a depth of about 60–70 km, corresponding well to the previous results (Bock, 1991; Woods et al., 1991; Woods and Okal, 1996; Priestley and Tilmann, 1999). The summation trace of these receiver functions (the “sum” trace on the right side of Fig. 5.9a) is also shown as “KIP data” in Fig. 5.10b. This trace is put into the inversion process (Kind et al., 1995) to get a 1-D velocity structure beneath KIP.

Fig. 5.10a shows two models of V_s structure beneath KIP. The model “P&T99”, which results from a surface wave study (Priestley and Tilmann, 1999), is used as starting model. “KIP model” is the inversion result. Synthetic receiver functions from these two models, which are calculated with the slowness and incident angle values averaged from the observed data at KIP, are shown as “P&T99 syn” and “KIP model syn” traces in Fig. 5.10b. While the “P&T99 syn” trace fits “KIP data” at time 0–10 sec, “KIP model syn” fits well the entire “KIP data”. However,

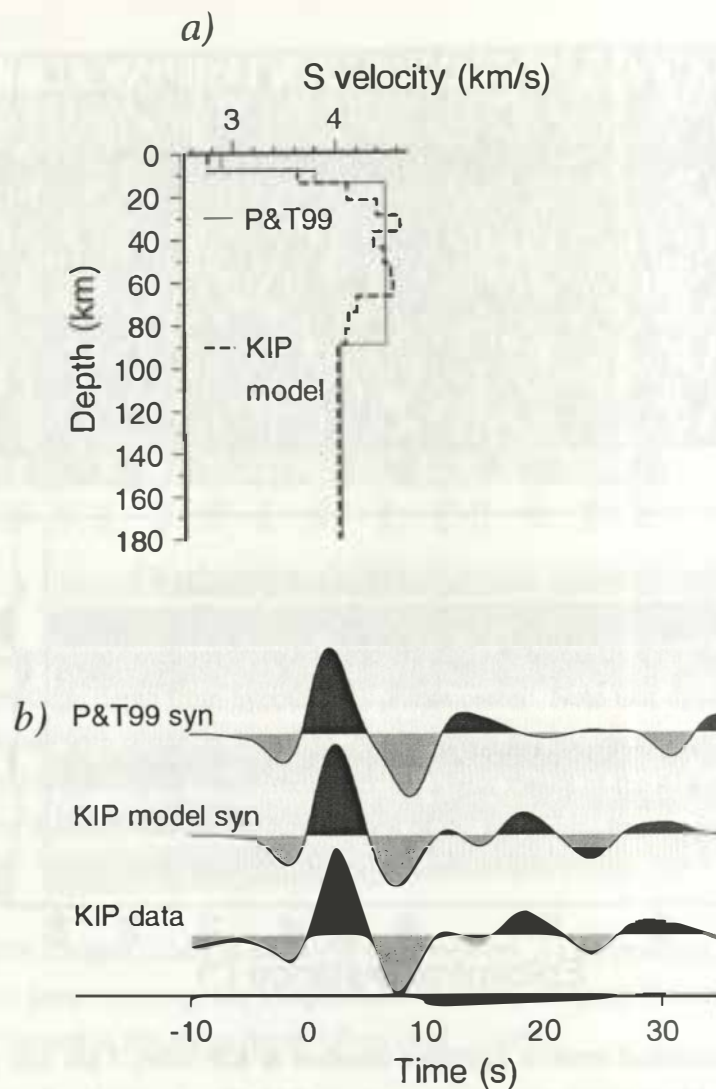


Figure 5.10: a). V_s models of the structure beneath KIP. “P&T99” results from surface wave (Priestley and Tilmann, 1999). “KIP model” is the inversion result starting with the “P&T99” model. b). Synthetic receiver functions of “P&T99” and “KIP model”. They are calculated with the slowness and incidence angle values averaged from the data at KIP. The trace “KIP data” is the summation trace of the individual receiver functions in Fig. 5.9a.

the difference between “P&T99” and “KIP model” is not very large (Fig. 5.9a). “KIP model” is similar to “P&T99” with some noise added, and the lithosphere-asthenosphere boundary is lifted up to about 65 km. This thinner lithosphere (in “KIP model”) is consistent with the result from S-to-P conversion (Bock, 1991).

Furthermore, synthetic receiver functions are calculated for the “KIP model” with the epicentral distance and incident angle values of all observed data. These synthetic receiver func-

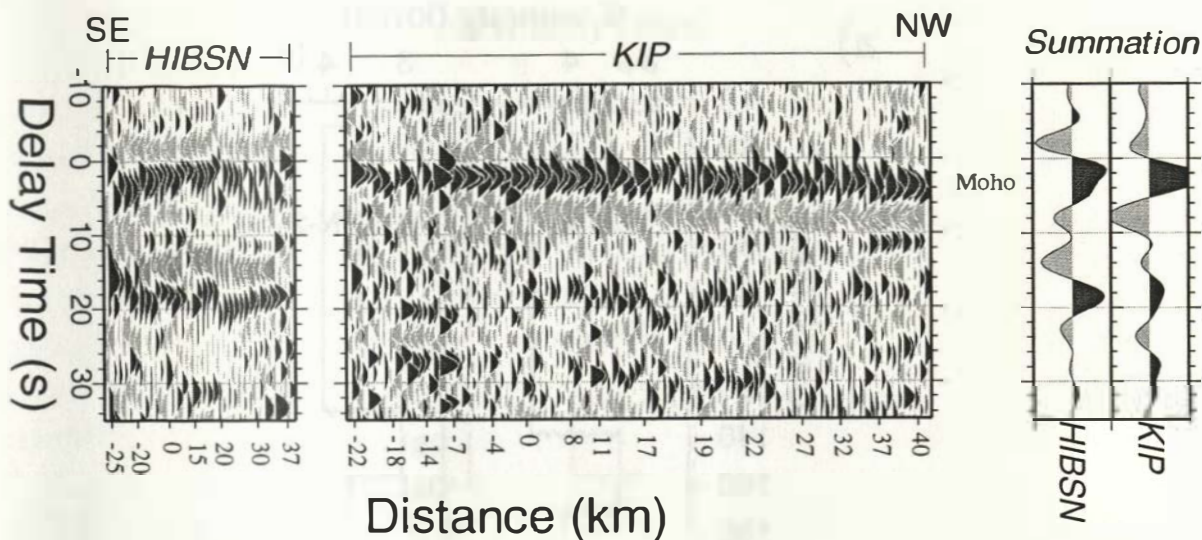


Figure 5.11: Individual receiver functions from HIBSN and KIP (after 5 sec low pass filter), sorted by the projection of their piercing points at 120 km depth on a line connecting KIP and HIBSN, which is parallel to the island chain (dashed line in Fig. 5.7).

tions are sorted also by the epicentral distance and shown in Fig. 5.9b. Comparing Fig. 5.9a and b, the observed Moho and the following negative phases (LVZ) are well modeled. The other two weak phases at about 18 (Mult 1) and 30 sec (Mult 2) in the data could be explained as multiples from shallow depth (Fig. 5.9a).

5.3.2 Island of Hawaii

Waveforms of the receiver functions at HIBSN in the first 35 sec delay time are different from those at KIP. Individual receiver functions from both stations are sorted again by the projection of their piercing points at 120 km depth onto a line connecting HIBSN and KIP, which is parallel to the island chain (dashed line in Fig. 5.7) and plotted in Fig. 5.11. These piercing points are plotted as crosses in Fig. 5.7.

At KIP, the large negative phase at 6–8 sec (labeled LVZ in Fig. 5.9) which follows the Moho can be modeled by a discontinuity atop of the asthenosphere at 65 km depth (“KIP model” in Fig. 5.10a). However, at HIBSN, a significant negative phase appears at about 14 sec and it is followed by a positive phase at ~18 sec (see the summation traces of the two stations in Fig. 5.11). The piercing points of this negative phase are marked in red in Fig. 5.7. These two phases are not predicted by “P&T99” and “KIP model” (Fig. 5.10) and can be well matched by models with a low velocity zone at a larger depth (> 100 km) (Fig. 5.12).

Because of the trade-off between velocity and discontinuity depth, the depth of the LVZ

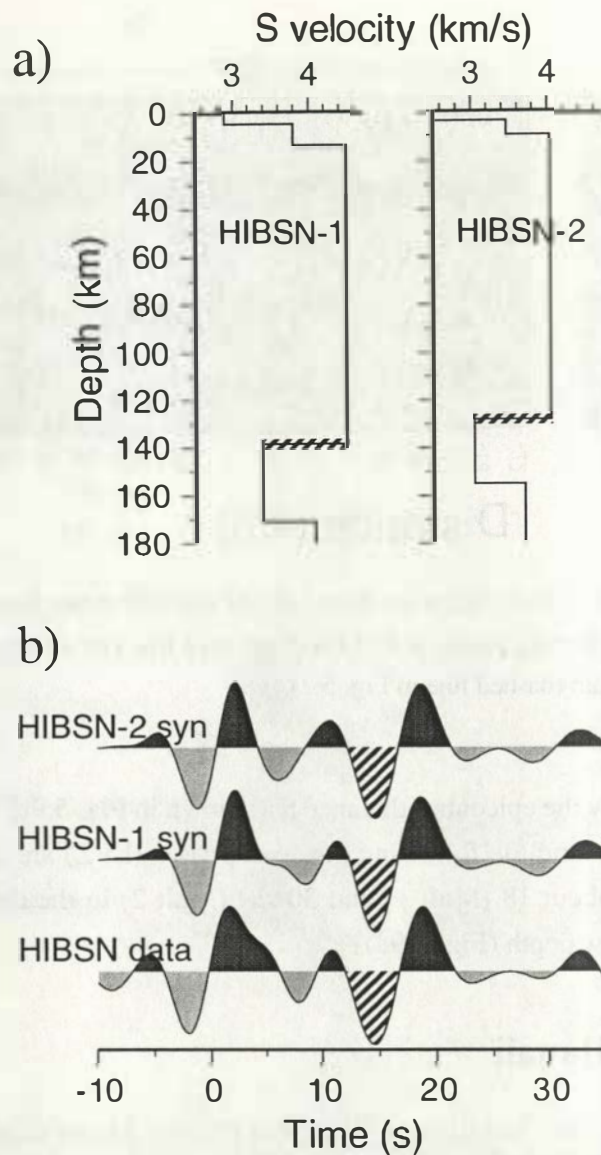


Figure 5.12: a). LVZ models of “HIBSN-1” and “HIBSN-2”, with low velocity zone at more than 100 km depth. The velocities in “HIBSN-1” at shallow depth are the same as in “P&T99”. “HIBSN-2” is similar to “HIBSN-1” but with an extreme low velocity in the lithosphere. b). “HIBSN data” (summation trace of receiver functions at HIBSN shown in Fig. 5.11) are fitted by synthetic receiver functions from “HIBSN-1” and “HIBSN-2”. The synthetic traces are calculated with the average slowness and incident angle of the observed data at HIBSN.

could be shallower if the velocity at shallower depth is smaller. In Fig. 5.12, two models are tested to constrain the depth of the LVZ. The model “HIBSN-1” in Fig. 5.12a has the same lithospheric velocities as the “P&T99”, but the top of the LVZ is put at 140 km depth. The average V_s in the lithosphere in model “HIBSN-2” is low (4 km/sec), and the top of the LVZ

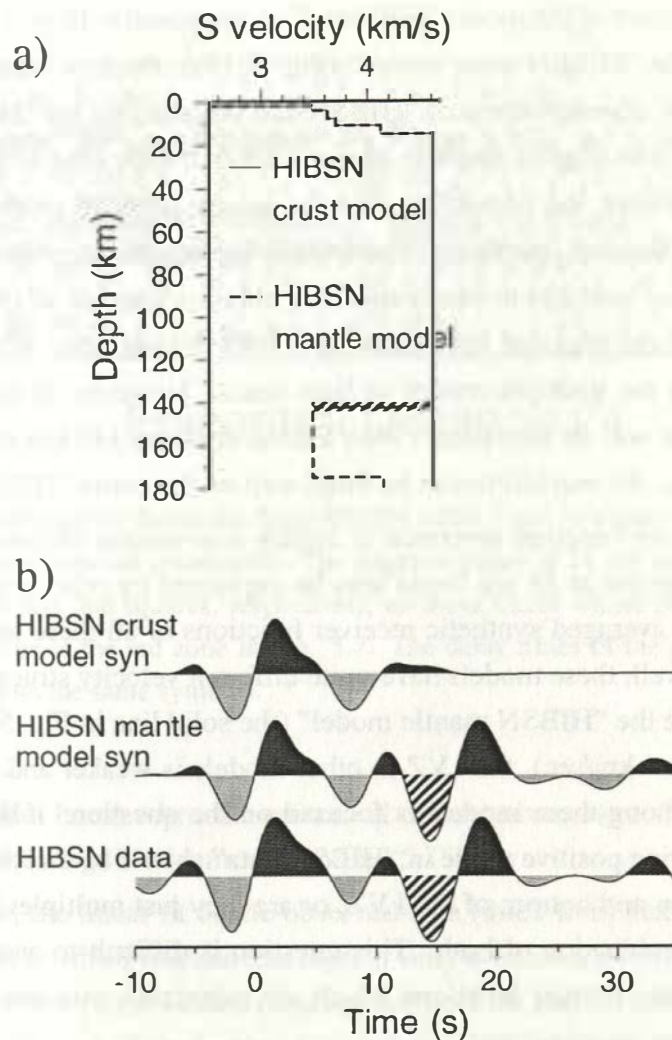


Figure 5.13: a). “HIBSN crust model” is improved “HIBSN-1” model at crust depth, underlain by a homogeneous mantle. “HIBSN mantle model” results from the inversion process (Kind et al., 1995) with “HIBSN crust model” as starting model; b). Synthetic receiver function from “HIBSN crust model” has a better fit to “HIBSN data” at times less than 5 sec. It shows that the energy from the crust is limited within 10 sec and can not contribute to the strong negative phase at 14 sec in “HIBSN data”. A LVZ which is at below 100 km depth (“HIBSN mantle model”) enables a good fitting of the whole data (“HIBSN mantle model syn”).

is put at 130 km depth. Waveforms of these models (“HIBSN-1 syn” and “HIBSN-2 syn”) are calculated with the average slowness and incident angle of the observed data. Both models fit the negative phase in “HIBSN data” very well. Therefore the depth of the LVZ beneath Hawaii should be between 130–140 km, well below the expected depth of the lithosphere-asthenosphere boundary beneath Hawaii, which is thought to be similar to that below KIP (less than 100 km) (Bock, 1991; Priestley and Tilmann, 1999).

The crustal structure of the model "HIBSN-1" is improved to fit the "HIBSN data" at times less than 5 sec. In the "HIBSN crust model" (Fig. 5.13a), the layered crust is underlain by a homogeneous mantle. The waveform of "HIBSN crust model" fits the "HIBSN data" till 10 sec (Fig. 5.13b), i.e. the first smaller negative phase at about 7 sec could be explained as multiples from the crust. However, the possibility that the strong negative phase in "HIBSN data" at 14 sec comes from the crust can be ruled out, since the main energy from the crust is limited within 10 sec. It is not possible to simultaneously obtain a good fit of the Moho conversion at HIBSN and produce the required strong multiple later than 10 sec. If the crust is thickened, it is possible to shift the multiple energy to later times. However, at the same time the fit of the Moho conversion will be degraded. With a LVZ at about 140 km depth ("HIBSN mantle model" in Fig. 5.13a), the waveform can be fitted well on the entire "HIBSN data" (Fig. 5.13b).

However, receiver function inversion is highly non-unique (Ammon et al., 1990). The significant negative phase at 14 sec could also be explained by other models as shown in Fig. 5.15a. Although the averaged synthetic receiver functions of all these models fit the data "HIBSN data" equally well, these models have quite different velocity structures, especially below 140 km depth. While the "HIBSN mantle model" (the solid line in Fig. 5.15a) has a significant LVZ (V_s is less than 4 km/sec), the LVZ in other models is weaker and even fades away. The critical difference among these models is focused on the question: if the significant negative phase and the following positive phase in "HIBSN data" should be direct conversions from discontinuities at the top and bottom of the LVZ, or are they just multiples from structures below the Moho, or the combination of both. This question is difficult to answer by only checking the averaged synthetic receiver functions which are calculated with the average slowness and incidence angle of the observed data.

Checking the variations of the phases in the individual receiver functions may provide a chance to distinguish these models. As shown in Fig. 5.14, all individual receiver functions from HIBSN are sorted by epicentral distance. The negative phase (at ~ 14 sec) and the following positive phase are clear on most of the individual traces. The piercing points (at 120 km depth) of these traces are within the red zone in Fig. 5.7. The two phases on these traces are labeled and their delay times are measured for each trace and plotted in Fig. 5.15b with dots and squares. The linear fittings of the measurements are shown by the two thick lines in Fig. 5.15b.

For each model in Fig. 5.15a, synthetic receiver functions are calculated with all slowness and incident angle values of the data, similar to the process in Fig. 5.9b. The delay times of the two phases are measured and plotted in Fig. 5.15b with the same line pattern as the model in Fig. 5.15a.

In Fig. 5.15b, the moveout curves of direct conversions and of multiples are different: The delay time of a direct conversion (the thin lines) decreases more rapidly than that of a multi-

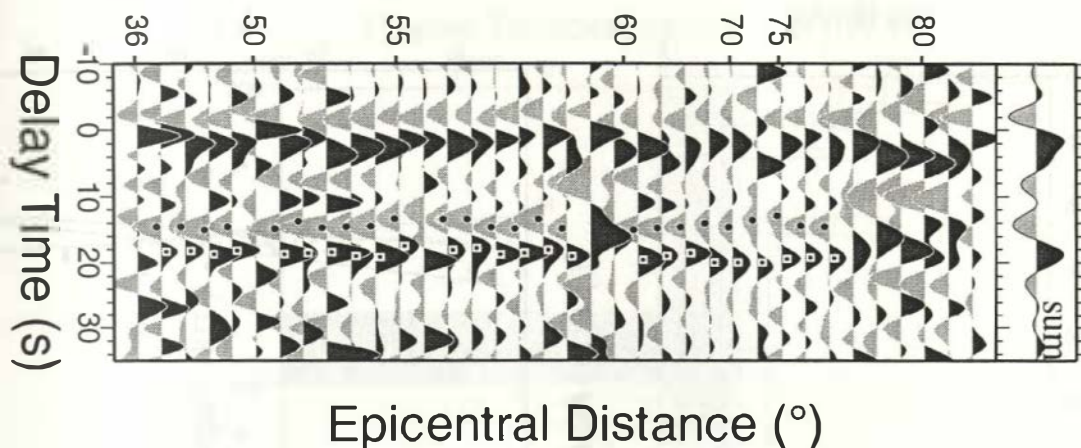


Figure 5.14: Individual receiver functions from HIBSN (after 5 sec low pass filter) are sorted by epicentral distance (without moveout correction). The negative phase at 14 sec and the following positive phase are labeled with dots and squares, respectively, on those traces whose piercing points at 120 km depth are identified to be in the red zone in Fig. 5.7. The delay times of the phases on each trace are plotted in Fig. 5.15b with the same symbols.

ple phase (the dash-dot lines) when the epicentral distance increases. This difference provide further constrains to distinguish the models in Fig. 5.15b.

At about 18 sec, the linear fit of the observed data (thick line) has the similar inclination like the moveout curves which implies that there is only a weak or even no discontinuity at that depths. Thus this positive phase in data (squares in Fig. 5.14 and 5.15b) should contain energy mainly of multiples from shallow depths, although the direct conversions from these possible discontinuities which are predicted to appear at times of around 5 sec are absent in data (Fig. 5.14).

At about 14 sec, the linear fit of the observed negative phase (thick lines and dots in Fig. 5.15b) is nearly parallel to the thin solid line and the dotted line, which indicates a discontinuity at 140–150 km depth (Fig. 5.15a). Thus, this negative phase in the data could be explained by a direct conversion at a discontinuity atop of a LVZ.

5.4 Implication for the Hawaiian mantle plume conduit

The existence of a pronounced LVZ at more than 100 km depth is a robust observation of the receiver functions at HIBSN, although the bottom of the LVZ could not be well constrained. A very low shear-wave velocity (less than 4 km/sec) in the ultra-mafic mantle at depths larger than 100 km can not be explained without the presence of significant partial melt even if the effect of anelasticity on seismic velocity is considered (Sobolev et al., 1996) and the water content of

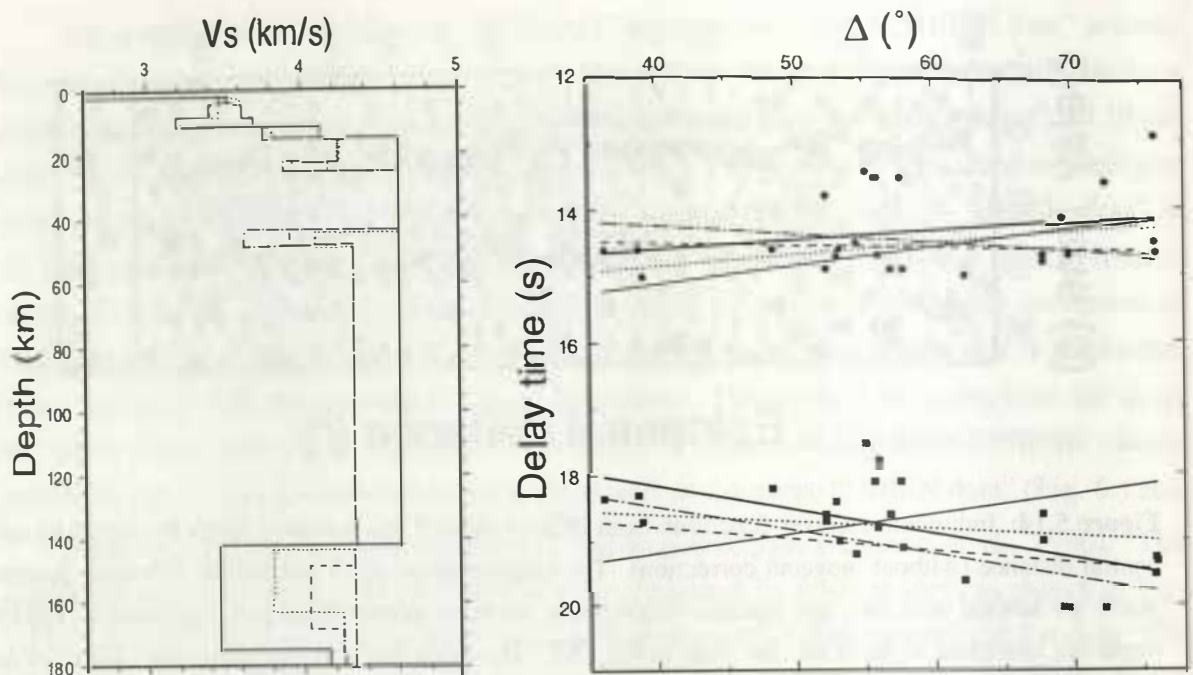


Figure 5.15: a). Some HIBSN models with fine structures right below the Moho; b). Delay times of the negative and positive phases measured from the synthetic receiver functions of the models in a) are plotted by the lines with the associated patterns as in a). Measurements from the data (Fig. 5.14) are shown with dots and squares, the two thick lines are their linear fits.

olivine and pyroxene is assumed to be high (Karato and Jung, 1998). This observed depth of the LVZ is consistent with the estimate of the depth and extent of the melt production region within the plume (~ 90 – 150 km depth) found by modeling the total melt production, residual depth anomaly, and geoid anomaly (Watson and McKenzie, 1991). It also agrees with the depth of the deepest region of intensive partial melting below Hawaii (100 – 130 km) suggested by the investigation of the primary melt inclusions in olivine crystals (Sobolev and Nikogosian, 1994). The deepest location of partial melting can be expected within the plume conduit where the temperature and water content of the minerals are highest. Therefore, the red zone in Fig. 5.7 should indicate the central part of the Hawaiian plume conduit. A few percent of partial melting is achieved below 130 – 140 km depth, and this, together with the high temperature and high water content of the plume material results in the very low observed shear wave velocity.

At shallower depth within the conduit, the degree of partial melting increases. Melt becomes mobile and leaves the root zone, causing de-watering of the olivine and pyroxene in the root zone. This in turn results in a seismic velocity increase (Karato and Jung, 1998; Hirth and Kohlstedt, 1996). The olivine de-watering becomes most important at a depth where the mantle temperature exceeds the peridotite dry solidus (Karato and Jung, 1998). This depth is close to

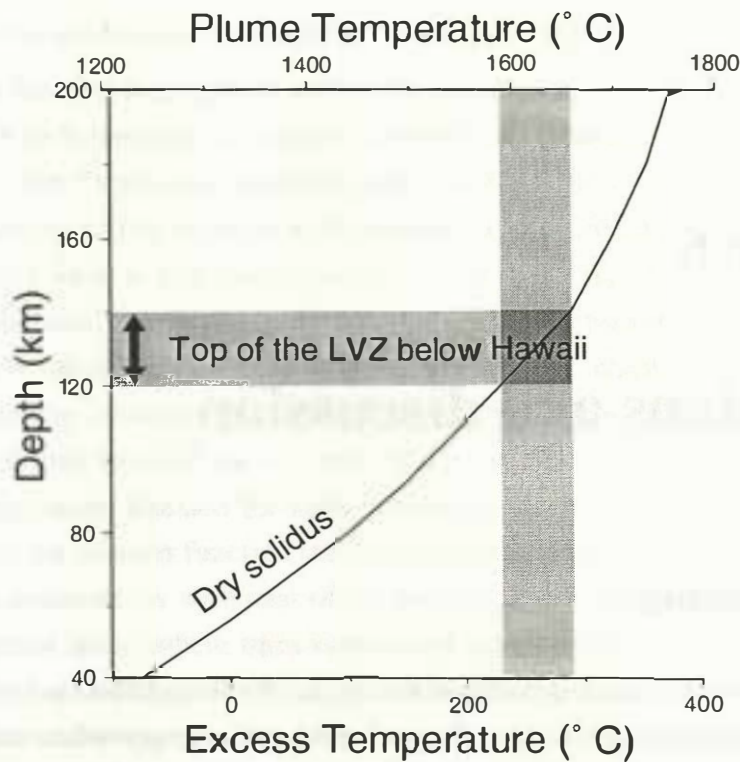


Figure 5.16: Relationship between the depth of the top of the low velocity zone and plume temperature. The top of the LVZ is associated with the peridotite de-watering effect, which is most pronounced shallower than the depth where the dry peridotite solidus is achieved (Karato and Jung, 1998). The location of the top of the LVZ at 120–140 km below Hawaii corresponds to a plume temperature higher than 1600–1650°C (250–300°C excess temperature).

60–80 km for the normal asthenospheric temperature, thus providing a possible explanation for the seismic velocity drop observed at this depth beneath the oceans (Karato and Jung, 1998; Hirth and Kohlstedt, 1996). Due to the higher temperature, the dry solidus temperature is exceeded at a much larger depth within the plume and thus a deeper location of the LVZ can be expected there. The depth to the top of LVZ in this model depends on the plume temperature and can therefore be used to estimate that temperature (Fig. 5.16). Using the depth dependence of the peridotite dry solidus temperature (McKenzie and Bickle, 1988) and the depth of the top of LVZ at 120–140 km, the temperature within the Hawaiian plume conduit could be estimated to be higher than 1600–1650°C (250–300°C excess temperature). This temperature agrees remarkably well with the petrological estimation of the highest temperature of the Hawaiian primary melts (1650°C) (Sobolev and Nikogosian, 1994) and with the temperature estimated by geochemical and geophysical modeling (Watson and McKenzie, 1991; Ribe and Christensen, 1994). It also agrees with the excess temperature estimation of the Hawaiian plume in the mantle transition zone (see previous section).

Chapter 6

Conclusions and discussion

6.1 Conclusions

The global upper mantle discontinuities at the depths of 410 and 660 km are widely accepted as mineral phase boundaries of olivine to β -spinel and γ -spinel to perovskite and magnesiowüstite, respectively. Thermodynamic principles govern phase transformations, making them sensitive to changes in the mantle's ambient pressure-temperature conditions. Changes in mantle temperature cause these phase transformations to occur at different pressures, therefore creating depth changes of the discontinuities. The topography of the upper mantle discontinuities is therefore a robust prospecting tool for the mantle temperature and provides important constraints on the dynamics of mantle convection.

The upper mantle shows the largest temperature anomalies in the regions of subduction zones and around mantle plumes. The 410 and 660 are expected to adjust their equilibrium positions in accordance with the ambient temperature anomalies. According to the phase transformation hypothesis, the transition zone thickness marked by the depth interval between the actual positions of the 410 and 660 has to be larger in the vicinity of the cold subducted oceanic lithosphere and smaller around the upwelling of the warm mantle plume material. In subduction zones, the lateral scale as well as the amplitude of the topographic anomaly of the discontinuities place important constraints on the behavior and geometry of subducted slabs, while in hot spot regions they may allow to map the trace of the plume within the mantle transition zone.

In the northwest Pacific, the old Pacific plate is subducting beneath the Eurasian plate and reaches about 600 km depth. In the Hawaiian hot spot area, the mantle plume is supposed to originate from the lower mantle or even at the core-mantle boundary. In these two tectonically different areas, cold or warm material penetrates the 410 and probably also the 660, possibly causing large temperature anomalies at transition zone depths. In this work, the receiver function technique has been used to detect the upper mantle discontinuities of the 410 and 660 in

the northwest Pacific subduction zone and the Hawaiian hotspot area.

The receiver function technique is a powerful tool to detect major discontinuities beneath seismic stations. P-to-S converted waves are contained predominately on the component which is perpendicular to the P wave and, therefore, can be isolated from the P wave by a rotation and deconvolution technique. The depth of a discontinuity can be obtained by measuring the time lag of the converted wave at that discontinuity relative to the direct P wave. The conversion amplitude depends mainly on the velocity contrast across the boundary. The accuracy of the depth estimation is limited by the knowledge of the velocity structure at the shallow depths above the discontinuity. However, the transition zone thickness, which is estimated by measuring the differential time between the 410 and 660, is less biased and provides a robust probe of the mantle temperature. Because the main conversion energy is typically within a frequency range of 0.1–1 Hz, the receiver function method provides a reasonably sufficient resolution for the upper mantle structure. A weakness of the method is that its application is so far limited mainly to continental areas, where three-component seismic stations are available. Yet, with the increasing number of the globally deployed seismic stations and the use of ocean bottom seismographs, receiver function studies will cover more and more areas on the Earth.

From P-to-S converted waves, the 410 and 660 upper mantle discontinuities have been observed in the two study areas. The topography of the discontinuities shows obviously a relationship with the subduction process and a mantle plume, and supports the mineral phase transformation hypothesis of the upper mantle discontinuities. The largest topographic variations of the 410 and the 660 are observed to be less than 40 km. Neither the 520 discontinuity nor discontinuities deeper than 660 km in the upper part of the lower mantle have been observed. At shallow depths, direct evidence has been found for the subducted Pacific slab and the Hawaiian plume conduit.

(1) Northwest Pacific subduction zone

In the northwest Pacific, the 410, although weak, is generally observed with small topography (less than 10 km). In the region where the slab is indicated by the seismicity to interact with the 410, the 410 is not observed. The local absence of the 410 could be attributed to a large lateral heterogeneity associated with the dynamically delayed phase transformation within the subducted slab. As an alternative explanation, a broadening of the olivine $\alpha \rightarrow \beta$ phase transformation at a low temperature may also be possible.

By comparison with the tomographic images, significant depression of the 660 is observed up to 30–40 km in the region where the slab is expected to reach the 660. However, no large lateral extension of the 660 deepening is observed by receiver functions, which does not support the flat-lying slab model suggested by some tomographic studies.

The significant thickening of the mantle transition zone (~ 30 km) lies within a limited

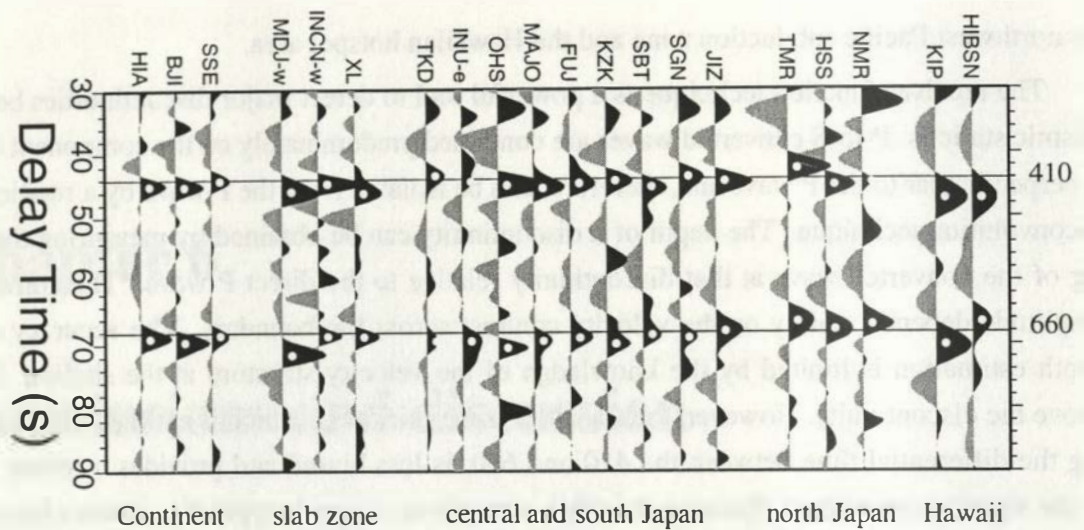


Figure 6.1: Stacked receiver functions of 20 stations which contain both the 410 and the 660 conversion phases. The two horizontal lines indicate delay times of the 410 and 660 for the IASP91 model

region of high velocities seen in tomographic images, implying that the subducted Pacific slab penetrates the 660 into the lower mantle.

At shallower depths, P-to-S converted waves from the subducted slab are also directly observed at some stations (FUJ, KFJ, SGN and TMR) which are located favorably for observing the slab. With more data available, the entire slab could probably be mapped.

(2) Hawaii hotspot area

In Hawaii, the upper mantle transition zone is thinner by up to 40–50 km in the area to the south-southwest of the island of Hawaii. This area is limited within a radius of about 200 km. It probably indicates the Hawaiian plume in the mantle transition zone with excess temperatures of about 300 °C. Large variations in the transition-zone thickness suggest a lower-mantle origin of the Hawaiian plume.

Right beneath the island of Hawaii, a low velocity zone is observed starting at 130–140 km depth and extending deep into the upper mantle. The phase is interpreted as an evidence of the plume conduit and could be caused by de-watering of the molten material within the plume. The depth of the low velocity zone corresponds to a plume excess temperature which agrees with the estimation from the thickness anomaly of the mantle transition zone.

6.2 Short discussion of global receiver functions

To compare the observations of the 410 and 660 discontinuities with other globally obtained receiver function studies, receiver functions in this work have been stacked for each individual station. Prior to stacking, each single receiver function has been move-out corrected for Ps conversions. Only the stacked receiver functions which contain clearly both the 410 and 660 conversion phases have been selected and plotted in Fig. 6.1. For stations MDJ, INCN and INU, there are large azimuthal variations of the 410 and 660 on their receiver functions. At MDJ and INCN, receiver functions with back-azimuth between 0° – 170° do not show the 410 (see Fig. 4.15 and 4.16), while at INU the 410 is absent on traces with back-azimuth between 180° – 360° . This azimuthal difference could be related to the complicated subducting process.

Table 6.1: The 410 and 660 beneath 20 stations

station	t_{410} (sec)	t_{660} (sec)	$t_{660}-t_{410}$ (sec)
HIA	45.0	69.0	24.0
BJI	45.1	69.6	24.5
SSE	44.2	68.6	24.4
MDJ-w	46.2	71.5	25.3
INCN-w	44.8	68.7	23.9
XL	46.2	68.8	22.6
TKD	43.5	69.5	26.0
INU-e	44.5	69.5	25.0
OHS	45.0	70.6	25.6
MAJO	45.5	69.5	24.0
FUJ	44.8	69.0	24.2
KZK	44.4	70.0	25.6
SBT	45.4	68.6	23.2
SGN	43.8	69.0	25.2
JIZ	44.5	67.8	23.3
TMR	42.5	66.0	23.5
HSS	45.0	67.8	22.8
NMR	44.6	67.0	22.4
KIP	47.2	70.4	23.2
HIBSN	47.2	66.6	19.4
IASP91	44.1	68.1	25.0

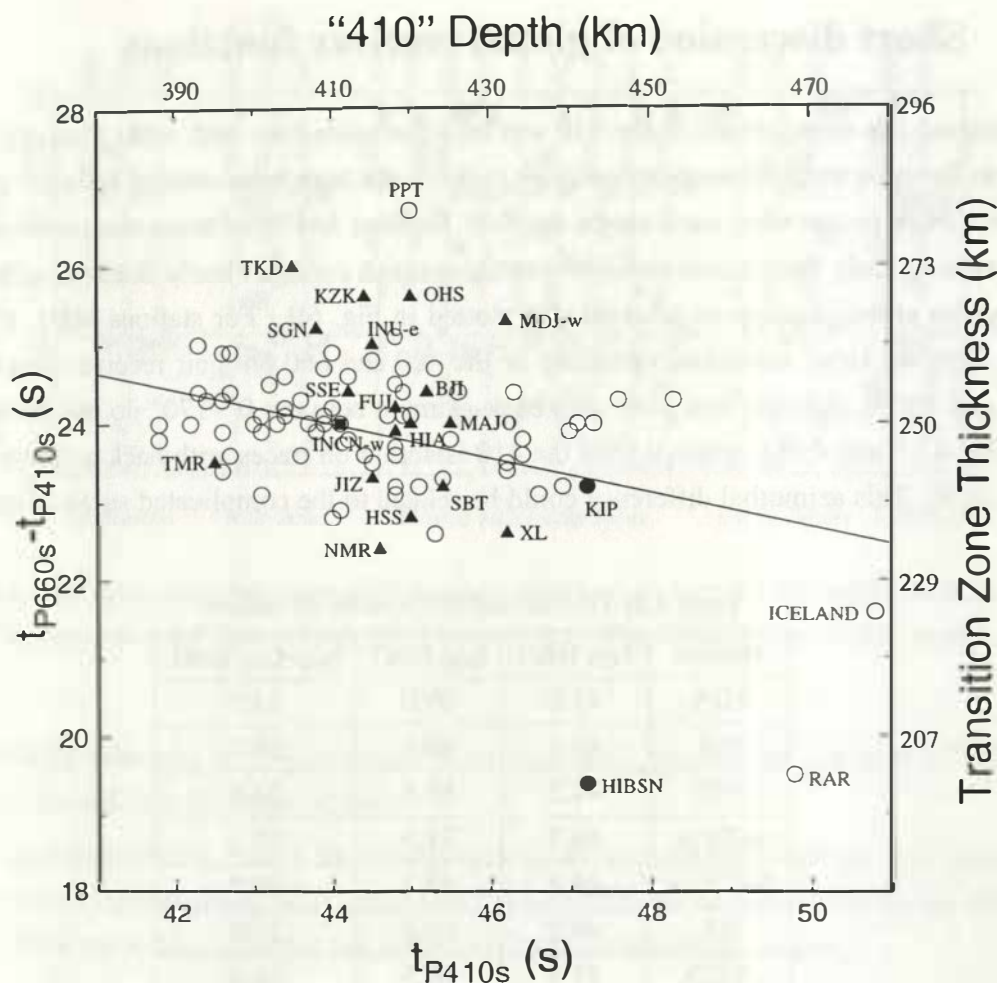


Figure 6.2: Delay times of the 410 and 660 phases in the receiver functions shown in Fig. 6.1 are measured and plotted with triangles (for the northwest Pacific stations) and dots (for KIP and HIBSN stations). The black square is calculated for the IASP91 model. Open circles are measurements from other receiver function studies (Bostock, 1996; Chen et al., 1994; Chevrot et al., 1999; Dricker et al., 1996; Kosarev et al., 1996; Shen et al., 1996; Stammer et al., 1992b; Vinnik et al., 1996a,b, 1997; Yuan et al., 1997); the thin line is their linear fitting (without RAR and PPT).

To measure the 410 and 660 delay times beneath these stations, receiver functions have been stacked with back-azimuth between 170° – 360° for stations MDJ and INCI (MDJ-w, INCI-w), and between 0° – 180° for station INU (INU-e).

The 410 and 660 discontinuities are dominant phases in the stacked receiver functions in Fig. 6.1. The measured delay times of the maximal amplitudes are listed in Table 6.1 and plotted in Fig. 6.2. Available previous receiver function results of the 410 and 660 from other sources are also plotted as open circles in Fig. 6.2 (Bostock, 1996; Chen et al., 1994; Chevrot et al., 1999; Dricker et al., 1996; Kosarev et al., 1996; Shen et al., 1996; Stammer et al., 1992b; Vinnik et

al., 1996a,b, 1997; Yuan et al., 1997). These studies have been applied in different tectonic areas of the Earth. The fitting line to these observations (the solid line in Fig. 6.2), obtained without the two extreme values published for RAR and PPT located in the South Pacific, shows a slightly negative trend with increasing value of t_{P410} . This is in general agreement with an anti-correlation of the 410 and 660 discontinuities and, therefore, supports the idea of the mineral phase transformation of the discontinuities. As a reference, the value of IASP91 model is also shown in Fig. 6.2 (black square). Comparing with other results, the measurements of the northwest Pacific area shows stronger scattering from the general trend (the solid line), which could be related to the complicated subduction process.

For the Hawaii stations, the transition zone thickness at KIP does not deviate largely from the linear fitting in Fig. 6.2, indicating the normal mantle temperature beneath the island of Oahu. However, HIBSN is remarkably below the solid line, suggesting an extreme high temperature beneath the island of Hawaii. Compared to the Iceland mantle plume, the Hawaiian plume should have a larger temperature anomaly in the transition zone.

Zusammenfassung

Die beiden global beobachteten seismischen Manteldiskontinuitäten in 410 und 660 km Tiefe markieren nach gängiger Meinung Phasentübergänge im Olivin, dem häufigsten Mineral in Mantelgestein. Diese Phasentübergänge resultieren aus der Zunahme des Druckes und der Temperatur mit der Tiefe. Aus petrologischen Laborexperimenten weiß man, daß sich die Kristallstruktur des Olivins zu der des β -Spinells bzw. die von γ -Spinell zu der von Perovskit und Magnesiumwüstit unter den Drücken und Temperaturen, die in diesen Tiefen herrschen, umwandelt. Dabei nehmen die seismologischen Geschwindigkeiten und die Dichte zu. Die sogenannte "Clapeyron Slope" beschreibt die Druck-Temperatur Abhängigkeit der Phasentransformationen. Der positive Wert für den Phasentübergang von Olivin zur β -Phase bedeutet, daß die Tiefe der 410-km Diskontinuität sich im gleichen Sinne mit der Temperatur ändert, d.h. bei Temperaturerhöhung zunimmt und bei Abkühlung abnimmt. Der Clapeyron Slope des Phasentübergangs bei 660 km Tiefe ist dagegen negativ und beschreibt einen inversen Zusammenhang zwischen Tiefen- und Temperaturänderung. Wenn es gelingt, lokale Variationen der Tiefe der beiden Diskontinuitäten seismisch zu beobachten, können daraus Rückschlüsse auf in dieser Tiefe herrschenden Temperaturen gezogen werden.

Im Nordwesten des pazifischen Subduktionszone erreicht die abtauchende pazifische Platte mehr als 600 km Tiefe (abgeleitet aus den tiefsten Erdbeben) und verursacht dort eine Abkühlung des Erdmantels. Wenn die Platte die 660-km Diskontinuität durchstößt, erwartet man eine schmale, dem Streichen der abtauchenden Platte folgende Absenkung der 660-km Diskontinuität. Falls die abtauchende Platte von der 660-km Diskontinuität abgelenkt wird, sollte eine breitere Anomalie der Topographie der 660-km Diskontinuität, eventuell auch eine Verdickung der gesamten Übergangszone beobachtet werden. Falls der Hawaii-Plume aus dem unteren Mantel stammt, sollte sich das heiße Plume-Material durch beide Manteldiskontinuitäten aufwärts bewegen und dabei eine deutliche Temperaturerhöhung innerhalb eines lateral kleinen Gebietes verursachen. Das sollte zu einer Aufwölbung der 660-km Diskontinuität und zu einer Absenkung der 410-km Diskontinuität, und damit zu einer Verdünnung der Übergangszone innerhalb der Aufstiegszone des Plumes führen. Deshalb kann die Art und Weise einer beobachteten Anomalie der 660-km Diskontinuität, der 410-km Diskontinuität oder der Mächtigkeit der Übergangszone Hinweise auf die Mantelkonvektion liefern.

Die Topographie der Diskontinuitäten im oberen Mantel kann mit Hilfe langperiodischer SS-Vorläufer oder kurzperiodischen quell- oder empfangernaher konvertierter Wellen untersucht werden. Die langperiodischen SS-Daten können zwar für Gebiete der Erde benutzt werden, in denen es keine Stationen oder Quellen gibt, ihre räumliche Auflösung ist jedoch mit mehr als 10° (Shearer, 1991) sehr gering. In der nordwestlichen pazifischen Subduktionszone, wo der Einfluß die abtauchenden pazifischen Platte relativ groß ist, zeigen die langperiodischen SS-Daten eine großräumig vertiefte 660-km Diskontinuität, begleitet von einer geringeren Topographie der 410-km Diskontinuität. In Hawaii können die kleinräumigen Plume-Strukturen des Erdmantels nicht mehr von den SS-Daten aufgelöst werden. Die SS-Vorläufer Methode ist besser geeignet für die Untersuchungen großräumiger Strukturen aber weniger geeignet für lokale Strukturen. Kurzperiodische quellnahe Konversionen dagegen sind besser geeignet, die lokale Topographie der 410- und 660-km Diskontinuität aufzulösen. Bisherige Ergebnisse zeigen in der Izu-Bonin Region eine deutliche kleinräumige Vertiefung der 660-km Diskontinuität, die auf einen abgesenkten Slab hinweisen könnte (Castle and Creager, 1998). Im Norden von Izu-Bonin erscheint eine breitere Vertiefung der 660-km Diskontinuität (Collier and Helfrich, 1997; Castle and Creager, 1998), die dadurch erklärt wird, daß die abtauchende Platte an der 660-km Diskontinuität subhorizontal abgelenkt wird (van der Hilst et al., 1991; Fukao et al., 1992). In Hawaii ist diese hochauflösende Methode wegen fehlender Tiefherdbeben nicht verwendbar. Für die Existenz eines Mantelplumes in Hawaii gab es bis jetzt deshalb keine eindeutigen seismologischen Hinweise. Die Topographie der 410- und 660-km Diskontinuität unter Hawaii wurde bisher noch nicht untersucht.

In dieser Arbeit werden die Diskontinuitäten in 410 und 660 km Tiefe im nordwestlichen Pazifik und unter Hawaii mit der Methode der Receiver Funktionen untersucht. Die Daten im Nordwest-Pazifik stammen von Stationen der Netze CDSN, CSN, GEOSCOPE und FREESIA. Auf den Hawaii Inseln wurden die Breitbanddaten der GEOSCOPE Station auf Oahu und auf der Hauptinsel von Hawaii die Daten eines temperären Netzes der University of Cambridge (England) und des US Geological Survey benutzt. Es wurden 3-Komponenten Registrierung von Beben mit einer Epizentraldistanz von $30-95^\circ$ und einem hohen Signal-Noise Verhältnis ausgewählt. Mit diesen Daten ergeben sich mehr als 5000 Receiver Funktionen für den Nordwest-Pazifik und etwa 200 für Hawaii. Mit den neu entwickelten Methoden der Move-out Korrektur und Migration der Zeitfunktionen, werden die 410- und 660-km Diskontinuität in beiden Gebieten abgebildet.

Im Nordwest-Pazifik sind Tiefenschwankungen der 410-km Diskontinuität gering. Dort, wo diese Diskontinuität von der pazifischen Platte durchgestoßen wird, wird sie in den Receiver Funktionen nicht abgebildet. Dies könnte durch den Einfluß des Subduktionsprozesses verursacht sein. Anders als die großräumige Vertiefung der 660-km Diskontinuität, wie sie in langperiodischen SS Vorläufern und kurzperiodischen quellnahen Konversionen gesehen wird,

zeigen die Receiver Funktionen eine deutliche Vertiefung der 660-km Diskontinuität nur in Gebieten, wo der Slab sie durchdringt. Eine weiträumige, subhorizontale Ablenkung der Platte, wie sie in tomographische Abbildungen erscheint (van der Hilst et al., 1991; Fukao et al., 1992) wird durch die Methode der Receiver Funktionen nicht bestätigt. Diese deuten im Gegenteil darauf hin, daß die Platte in den unteren Mantel eindringt. Im obersten Mantel (bis 250 km) wird die pazifische Platte im Bereich von Nord- und Zentral-Honshu von den Receiver Funktionen einiger Stationen direkt dargestellt.

Südwestlich von Hawaii wird eine kleinräumige, aber deutliche Aufwölbung der 660-km Diskontinuität und eine Verdünnung der Übergangszone (30–50 km gegenüber dem IASP91 Referenzmodell) innerhalb eines Gebietes von ca. 200 km Radius beobachtet. Dieses Ergebnis weist auf die Existenz eines Mantelplumes mit einer positiven Temperaturanomalie von ca. 200–350°C in dieser Tiefe hin. Direkt unterhalb der Hauptinsel von Hawaii zeigen die Receiver Funktionen eine Niedriggeschwindigkeitszone (Low Velocity Zone) in 120–140 km Tiefe. Die Obergrenze dieser Zone könnte durch die Entwässerung des heißen Plumematerials verursacht werden. Die daraus resultierende Temperaturanomalie stimmt mit der Abschätzung aus der Verdünnung der Übergangszone überein.

[The text in this section is extremely faint and illegible. It appears to be a multi-paragraph discussion or list of items, but the specific content cannot be transcribed.]

Bibliography

- Akaogi, M., E. Ito and A. Navrotsky, Olivine-modified spinel-spinel transitions in the system $\text{Mg}_2\text{SiO}_4\text{-Fe}_2\text{SiO}_4$: Calorimetric measurements, thermodynamic calculation, and geophysical application, *J. Geophys. Res.* **94**, 15671–15685, 1989.
- Aki, K. and P. G. Richards, Quantitative Seismology: Theory and Methods, 133–155, W. H. Freeman and Company, San Francisco, 1980.
- Aki, K., A. Christoffersson and E. S. Husebye, Determination of the three-dimensional seismic structure of the lithosphere, *J. Geophys. Res.* **82**, 277–296, 1977.
- Ammon, C. J., G. E. Randall and G. Zandt, On the nonuniqueness of receiver function inversion, *J. Geophys. Res.* **95**, 15303–15318, 1990.
- Anderson, D. L., The deep structure of continents, *J. Geophys. Res.* **84**, 7555–7561, 1979.
- Anderson, D. L. and J. D. Bass, Transition region of the Earth's upper mantle, *Nature* **320**, 321–328, 1986.
- Benz, H. M. and J. E. Vidale, Sharpness of upper-mantle discontinuities determined from high-frequency reflections, *Nature* **365**, 147–150, 1993.
- Bernal, J. D., Geophysical discussion, *Observatory* **59**, 265–269, 1936.
- Bijwaard, H., W. Spakman and E. R. Engdahl, Closing the gap between regional and global travel time tomography, *J. Geophys. Res.* **103**, 30055–30078, 1998.
- Bina, C. R. and G. Helffrich, Phase transition Clapeyron slopes and transition zone seismic discontinuity topography, *J. Geophys. Res.* **99**, 15853–15860, 1994.
- Bina, C. R. and B. J. Wood, Olivine-spinel transitions: Experimental and thermodynamic constraints and implications for the nature of the 400-km seismic discontinuity, *J. Geophys. Res.* **92**, 4853–4866, 1987.

- Birch, F., The velocity of compressional waves in rocks to 10 kilobars, *Part 2. J. Geophys. Res.* **66**, 2199–2224, 1961.
- Bock, G., Long-period S to P converted waves and the onset of partial melting beneath Oahu, Hawaii, *Geophys. Res. Lett.* **18**, 869–872, 1991.
- Bock, G., Synthetic seismogram images of upper mantle structure: No evidence for a 520-km discontinuity, *J. Geophys. Res.* **99**, 15843–15851, 1994.
- Bock, G. and J. Ha, Short-period S-P conversion in the mantle at a depth near 700km, *Geophys. J. R. Astr. Soc.* **77**, 593–615, 1984.
- Bock, G. and R. Kind, A global study of S-to-P and P-to-S conversions from the upper mantle transition zone, *Geophys. J. Int.* **107**, 117–129, 1991
- Bock, G., J. Gossler, W. Hanka, R. Kind, G. Kosarev, N. Petersen, K. Stammer and L. Vinnik, On the seismic discontinuities in the upper mantle, *Phys. Earth Planet. Inter.* **92**, 39–43, 1995.
- Bostock, M. G., Ps conversions from the upper mantle transition zone beneath the Canadian landmass, *J. Geophys. Res.* **101**, 8393–8402, 1996.
- Burdick, L. J. and C. A. Langston, Modeling crust-structure through the use of converted phases in teleseismic body-waveforms, *Bull. Seism. Soc. Am.* **67**, 677–691, 1977.
- Cassidy, J. F., Numerical experiments in broadband receiver function analysis, *Bull. Seism. Soc. Am.* **82**, 1453–1474, 1992.
- Castle, J. C. and K. C. Creager, Seismic evidence against a mantle chemical discontinuity near 660km depth beneath Izu-Bonin, *Geophys. Res. Lett.* **24**, 241–244, 1997.
- Castle, J. C. and K. C. Creager, Topography of the 660-km seismic discontinuity beneath Izu-Bonin: Implications for tectonic history and slab deformation, *J. Geophys. Res.* **103**, 12511–12527, 1998.
- Castle, J. C. and K. C. Creager, Local sharpness and shear wave speed jump across the 660-km discontinuity, *J. Geophys. Res.* **105**, 6191–6200, 2000.
- Chaljub, E. and A. Tarantola, Sensitivity of SS precursors to topography on the upper-mantle 660-km discontinuity, *Geophys. Res. Lett.* **24**, 2613–2616, 1997.
- Chen, Y. H., G. L. Kosarev and S. W. Roecker, The nature of the crustal and upper mantle discontinuities determined from analysis of waveform recorded by broadband arrays in Pakistan and Kirghizstan, *Eos Fall Suppl.* **75**, 464.

- Chevrot, S., L. Vinnik and J. P. Montagner, Global scale analysis of the mantle Pds phases, *J. Geophys. Res.* **104**, 20,203–20,219, 1999.
- Christensen, U. R., The influence of trench migration on the slab penetration into the lower mantle, *Earth Planet. Sci. Lett.* **140**, 27–39, 1996.
- Christensen, U. R. and D. A. Yuen, The interaction of a subducting lithospheric slab with a chemical or phase boundary, *J. Geophys. Res.* **89**, 4389–4402, 1984.
- Collier, J. D., An investigation of the depths and properties of the mantle's seismic discontinuities in subduction zones, doctoral thesis, Fac. of Sci., Dep. of Earth Sci., Univ. of Bristol, Bristol, England, 1999.
- Collier, J. D. and G. R. Helffrich, Topography of the "410" and "660" km seismic discontinuities in the Izu-Bonin subduction zone, *Geophys. Res. Lett.* **24**, 1535–1538, 1997.
- Creager, K. C. and T. H. Jordan, Slab penetration into the lower mantle beneath the Mariana and other island arcs of the northwest Pacific, *J. Geophys. Res.* **91**, 3573–3589, 1986.
- Dässler, R. and D. A. Yuen, The metastable olivine wedge in fast subducting slabs: Constraints from the thermo-kinetic coupling, *Earth Planet. Sci. Lett.* **137**, 109–118, 1996.
- DeMets, C., R. G. Gordon, D. F. Argus and S. Stein, Current plate motions, *Geophys. J. Int.* **101**, 425–478, 1990.
- Dricker, I.G., S. W. Roecker, G. L. Kosarev and L. P. Vinnik, Shear-wave velocity structure of the crust and upper mantle beneath the Kola Peninsula, *Geophys. Res. Lett.* **23**, 3389–3392, 1996.
- Drummond, B. J., K. J. Muirhead and A. L. Hales, Evidence for a seismic discontinuity near 200 km depth under a continental margin, *Geophys. J. R. Astr. Soc.* **70**, 67–77, 1982.
- Dueker, K. G. and A. F. Sheehan, Mantle discontinuity structure from midpoint stacks of converted P to S waves across the Yellowstone hotspot tract, *J. Geophys. Res.* **102**, 8313–8327, 1997.
- Dueker, K. G. and A. F. Sheehan, Mantle discontinuity structure beneath the Colorado Rocky Mountains and High Plains, *J. Geophys. Res.* **103**, 7153–7169, 1998.
- Duffy, T. S. and D. L. Anderson, Seismic velocities in mantle minerals and the mineralogy of the upper mantle, *J. Geophys. Res.* **94**, 1895–1912, 1989.
- Duffy, T. S., C. S. Zha, R. T. Downs, H. K. Mao and J. R. Hemley, Elasticity of forsterite to 15GPa and the composition of the upper mantle, *Nature* **378**, 170–173, 1995.

- Dziewonski, A. M. and D. L. Anderson, Preliminary reference Earth model, *Phys. Earth Planet. Inter.* **25**, 297–356, 1981.
- Ekström, G. and A. M. Dziewonski, The unique anisotropy of the Pacific upper mantle, *Nature* **394**, 168–172, 1998.
- Engdahl, E. R., R. D. van der Hilst, R. Buland, Global teleseismic earthquake relocation with improved travel times and procedures for depth determination, *Bull. Seism. Soc. Am.* **88**, 722–743, 1998.
- Estabrook, C. and R. Kind, The nature of the 660-kilometer upper-mantle seismic discontinuity from precursors to the PP phase, *Science* **274**, 1179–1182, 1996.
- Faber, S. and G. Müller, Converted phases from the mantle transition zone observed at European stations, *J. Geophys.* **54**, 183–194, 1984.
- Flanagan, M. P. and P. M. Shearer, Global mapping of topography on transition zone velocity discontinuities by stacking SS precursors, *J. Geophys. Res.* **103**, 2673–2692, 1998a.
- Flanagan, M. P. and P. M. Shearer, Topography on the 410-km seismic velocity discontinuity near subduction zones from stacking of sS, sP, and pP precursors, *J. Geophys. Res.* **103**, 21165–21182, 1998b.
- Frohlich, C., The nature of deep-focus earthquakes, *Ann. Rev. Earth Planet. Sci.* **17**, 227–254, 1989.
- Fukao, Y., S. Hori and M. Ukawa, A seismological constraint on the depth of basalt-eclogite transition in a subducting oceanic crust, *Nature* **303**, 413–415, 1983.
- Fukao, Y., M. Obayashi, H. Inoue and M. Nenbai, Subducting slabs stagnant in the mantle transition zone *J. Geophys. Res.* **97**, 4809–4822, 1992.
- Gossler, J., Seismische Untersuchung von lateralen Inhomogenitäten in der Überganszone des Erdmantels, *Ph.d thesis at the Freie Universität Berlin*, 1995.
- Gossler, J. and R. Kind, Seismic evidence for very deep roots of continents, *Earth Planet. Sci. Lett.* **138**, 1–13, 1996.
- Grand, S. P., Mantle shear structure beneath the Americas and surrounding oceans, *J. Geophys. Res.* **99**, 11591–11621, 1994.
- Grand, S. P. and D. V. Helmberger, Upper mantle shear structure of north America, *Geophys. J. R. Astr. Soc.* **76**, 399–438, 1984.

- Griffiths, R. W., R. I. Hackney and R. D. van der Hilst, A laboratory investigation of effects of trench migration on the descent of subducted slabs, *Earth Planet. Sci. Lett.* **133**, 1–17, 1995.
- Gu, Y., A. M. Dziewonski and C. B. Agee, Global de-correlation of the topography of transition zone discontinuities, *Earth Planet. Sci. Lett.* **157**, 57–67, 1998.
- Gudmundsson, O. and M. Sambridge, A regionalized upper mantle (RUM) seismic model, *J. Geophys. Res.* **103**, 7121–7136, 1998.
- Guillou-Frottier, L., J. Buttles and P. Olson, Laboratory experiments on the structure of subducted lithosphere, *Earth Planet. Sci. Lett.* **133**, 19–34, 1995.
- Gumis, M. and B. H. Hager, Controls of the structure of subducted slabs, *Nature* **335**, 317–321, 1988.
- Gurrola, H., J. B. Minster and T. Owens, The use of velocity spectrum for stacking receiver functions and imaging upper mantle discontinuities, *Geophys. J. Int.* **117**, 427–440, 1994.
- Hales, A. L., K. J. Muirhead and J. M. W. Rynn, A compressional velocity distribution for the upper mantle, *Tectonophysics* **63**, 309–348, 1980.
- Hasegawa, A., S. Horiuchi and N. Umino, Seismic structure of the northeastern Japan convergent margin: A synthesis, *J. Geophys. Res.* **99**, 22295–22311, 1994.
- Haskell, N. A., Crustal reflections of plane P and SV waves. *J. Geophys. Res.* **67**, 4751–4767, 1962.
- Helfrich, G., Topography of the transition zone seismic discontinuity, *Rev. Geophys.* **38**, 141–158, 2000.
- Helfrich, G. and C. R. Bina, Frequency dependence of the visibility and depths of mantle seismic discontinuities, *Geophys. Res. Lett.* **21**, 2613–2616, 1994.
- Helfrich, G. R. and B. J. Wood, 410km discontinuity sharpness and the form of the olivine α - β phase diagram: Resolution of apparent seismic contradictions, *Geophys. J. Int.* **126**, F7–F12, 1996.
- Helfrich, G. R., S. Stein, B. J. Wood, Subduction zone thermal structure and mineralogy and their relationship to seismic wave reflections and conversions at the slab/mantle interface, *J. Geophys. Res.* **94**, 753–763, 1989.
- Hirahara, K., A. Ikami, M. Ishida and T. Mikumo, Three-dimensional P-wave velocity structure beneath central Japan: low-velocity bodies in the wedge portion of the upper mantle above high-velocity subducting plates, *Tectonophysics* **163**, 63–73, 1989.

- Hirth, G. and D. L. Kohlstedt, Water in the oceanic upper mantle: implications for rheology, melt extraction and the evolution of the lithosphere, *Earth Planet. Sci. Lett.* **144**, 93–108, 1996.
- Hofmann, A. W., Mantle geochemistry: the message from oceanic volcanism, *Nature* **385**, 219–229, 1997.
- Iidaka, T. and Y. Furukawa, Double seismic zone for deep earthquakes in the Izu-Bonin subduction zone, *Science* **263**, 1116–1117, 1994.
- Iidaka, T. and D. Suetsugu, Seismological evidence for metastable olivine inside a subducting slab, *Nature* **356**, 593–595, 1992.
- Irifune, T., An experimental investigation of the pyroxene-garnet transformation in a pyrolite composition and its bearing on the constitution of the mantle, *Phys. Earth Planet. Inter.* **45**, 324–336, 1987.
- Ishida, M. and A. H. Hasemi, Three-dimensional fine velocity structure and hypocentral distribution of earthquakes beneath the Kanto-Tokai district, Japan, *J. Geophys. Res.* **93**, 2076–2094, 1988.
- Ita, J. and L. Stixrude, Petrology, elasticity and composition of the mantle transition zone, *J. Geophys. Res.* **97**, 6849–6866, 1992.
- Ito, E. and E. Takahashi, Postspinel transformations in the system Mg_2SiO_4 - Fe_2SiO_4 and some geophysical implications, *J. Geophys. Res.* **94**, 10637–10646, 1989.
- Ito, E. and H. Yamada, Stability relations of silicate spinels, ilmenites, and perovskites, in *High-Pressure Research in Mineral Physics*, edited by S. Akimoto and M. H. Manghnani, 405–419, Center for Academic Publications, Tokyo, 1982.
- Ito, E., M. Akaogi, L. Topor and A. Navrotsky, Negative pressure-temperature slopes for reactions forming $MgSiO_3$ perovskite from calorimetry, *Science* **249**, 1275–1278, 1990.
- Jeanloz, R., Effects of phase transitions and possible compositional changes on the seismological structure near 650km depth, *Geophys. Res. Lett.* **18**, 1743–1746, 1991.
- Ji Y. and H.-C. Nataf, Detection of mantle plumes in the lower mantle by diffraction tomography: Hawaii, *Earth Planet. Sci. Lett.* **159**, 99–115, 1998.
- Jones, C. H. and R. A. Phinney, Seismic structure of the lithosphere from teleseismic converted arrivals observed at small arrays in the southern Sierra Nevada and vicinity, California, *J. Geophys. Res.* **103**, 10065–10090, 1998.

- Kamiya, S., T. Miyatake and K. Hirahara, How deep can we see the high velocity anomalies beneath the Japan Island? *Geophys. Res. Lett.* **15**, 828–831, 1988.
- Karato, S. and H. Jung, Water, partial melting and the origin of the seismic low velocity and high attenuation zone in the upper mantle, *Earth Planet. Sci. Lett.* **157**, 193–207, 1998.
- Katsura, T. and E. Ito, The system Mg_2SiO_4 - Fe_2SiO_4 at high pressures and temperatures: precise determinations of stabilities of olivine, modified spinel, and spinel, *J. Geophys. Res.* **94**, 15663–15670, 1989.
- Kawakatsu, H. and F. Niu, Seismic evidence for a 920-km discontinuity in the mantle, *Nature* **371**, 301–305, 1994.
- Kellogg, L. H., Interactions of plumes with a compositional boundary at 670km *Geophys. Res. Lett.* **18**, 865–868, 1991.
- Kennett, B. L. N. and E. R. Engdahl, Travel times for global earthquake location and phase identification, *Geophys. J. Int.* **105**, 429–465, 1991.
- Kind, R. and L. P. Vinnik, The upper mantle discontinuities underneath the GRF array from P-to-S converted phases, *J. Geophys.* **62**, 138–147, 1988.
- Kind, R., G. L. Kosarev and N. V. Petersen, Receiver functions at the stations of the German Regional Seismic Network (GRSN), *Geophys. J. Int.* **121**, 191–202, 1995.
- Kirby, S. H., W. B. Durham, and L. A. Stern, Mantle phase changes and deep-earthquake faulting in subducting lithosphere, *Science* **252**, 216–225, 1991.
- Kirby, S. H., S. Stein, E. A. Okal and D. C. Rubie, Metastable mantle phase transformations and deep earthquakes in subducting oceanic lithosphere, *Rev. Geophys.* **34**, 261–306, 1996.
- Koper, K. D., D. A. Wiens, L. M. Dorman, J. A. Hildebrand and S. C. Webb, Modeling the Tonga slab: Can travel time data resolve a metastable olivine wedge? *J. Geophys. Res.* **103**, 30079–30100, 1998.
- Kosarev, G., R. Kind, S. V. Sobolev, X. Yuan, W. Hanka, S. Oreshin, Seismic evidence for a detached Indian lithospheric mantle beneath Tibet, *Science* **283**, 1306–1309, 1999.
- Kosarev, G., N. Petersen and L. Vinnik, Comment on ‘the use of velocity spectrum for stacking receiver functions and imaging upper mantle discontinuities’ by H. Gurrola, J. B. Minster and T. Owens, *Geophys. J. Int.* **124**, 637–641, 1996.
- Langston, C. A., Corvallis, Oregon, crustal and upper mantle structure from teleseismic P and S waves, *Bull. Seism. Soc. Am.* **67**, 713–724, 1977a.

- Langston, C. A., The effect of planar dipping on source and receiver responses for constant ray parameter, *Bull. Seism. Soc. Am.* **67**, 1029–1050, 1977b.
- Langston, C. A., Structure under Mount Rainer, Washington, inferred from teleseismic body waves, *J. Geophys. Res.* **84**, 4749–4762, 1979.
- Langston, C. A., Evidence for the subducting lithosphere under southern Vancouver Island and western Oregon from teleseismic P wave conversion, *J. Geophys. Res.* **84**, 3857–3866, 1981.
- Laske, G. J. P. Morgan and J. A. Orcutt, First results from the Hawaiian SWELL pilot experiment, *Geophys. Res. Lett.* **26**, 3397–3400, 1999.
- Lee, D. K. and S. P. Grand, Depth of the upper mantle discontinuities beneath the East Pacific Rise, *Geophys. Res. Lett.* **23**, 3369–3373, 1996.
- Leven, J. H., I. Jackson and A. E. Ringwood, Upper mantle seismic anisotropy and lithospheric decoupling, *Nature* **289**, 234–239, 1981.
- Li, X. and J. L. Nábělek, Deconvolution of teleseismic body waves for enhancing structure beneath a seismometer array, *Bull. Seism. Soc. Am.* **89**, 190–201, 1999.
- Li, A., K. M. Fischer, M. E. Wyssession and T. J. Clarke, Mantle discontinuities and temperature under North American continental keel, *Nature* **395**, 160–163, 1998.
- Liu, L.-G., The post-spinel phase of forsterite, *Nature* **262**, 770–772, 1976.
- Liu, L. G., *The Earth: Its origin, structure and evolution*, Academic Press, London, 1979.
- Machetel, P. and P. Weber, Intermittent layered convection in a model mantle with an endothermic phase change at 670km, *Nature* **350**, 55–57, 1991.
- Matsuzawa, T., N. Umino, A. Hasegawa and A. Takagi, Upper mantle velocity structure estimated from PS-converted wave beneath the northeastern Japan arc, *Geophys. J. R. Astron. Soc.* **86**, 767–787, 1986.
- McKenzie, D. P., Speculations on the consequences and causes of plate motions, *Geophys. J. R. Astr. Soc.* **18**, 1–32, 1969.
- McKenzie, D. and M. J. Bickle, The volume and composition of melt generated by extension of the lithosphere, *J. Petrol.* **29**, 625–679, 1988.
- Mechie, J., A. V. Egorkin, L. Solodilov, K. Fuchs, F. Lorenz and F. Wenzel, Major features of the mantle velocity structure beneath northern Eurasia from long-range seismic recordings of Peaceful Nuclear Explosions. in *Upper Mantle Heterogeneities from Active and Passive*

- Seismology*, K. Fuchs, Ed. (NATO ASI Series, Kluwer Academic Publishers, Dordrecht, Boston, London, 1997) pp. 33–50.
- Molnar, P., D. Freedman and J. S. H. Shih, Lengths of intermediate and deep seismic zones and temperatures in downgoing slab of lithosphere, *Geophys. J. R. Astr. Soc.* **56**, 41–54, 1979.
- Morgan, W. J., Convective plumes in the lower mantle, *Nature* **230**, 42–43, 1971.
- Morgan, J. P. and P. M. Shearer, Seismic constraints on mantle flow and topography of the 660-km discontinuity: evidence for whole-mantle convection, *Nature* **365**, 506–511, 1993.
- Morgan, J. P., W. J. Morgan and E. Price, Hotspot melting generates both hotspot volcanism and a hotspot swell? *J. Geophys. Res.* **100**, 8054–8062, 1995.
- Myers, S. C., T. C. Wallace, S. L. Beck, P. G. Silver, G. Zandt, J. Vandecar and E. Minaya, Implications of spatial and temporal development of the aftershock sequence for the M_w 8.3 June 9, 1994 deep Bolivia earthquake, *Geophys. Res. Lett.* **22**, 2269–2272, 1995.
- Nakakuki, T., H. Sato and H. Fujimoto, Interaction of the upwelling plume with the phase and chemical boundary at the 670km discontinuity: Effects of temperature-dependent viscosity, *Earth Planet. Sci. Lett.* **121**, 369–384, 1994.
- Nakanishi, I., Precursors to ScS phases and dipping interface in the upper mantle beneath southwestern Japan, *Tectonophysics* **69**, 1–35, 1980.
- Nataf, H.-C., Seismic imaging of mantle plumes, *Ann. Rev. Earth Planet. Sci.* **28**, 391–417, 2000.
- Neele, F., H. de Regt and J. VanDecar, Gross errors in upper-mantle discontinuity topography from underside reflection data, *Geophys. J. Int.* **129**, 194–204, 1997.
- Nishimura, C. and D. Forsyth, Rayleigh wave phase velocities in the Pacific with implications for azimuthal anisotropy and lateral heterogeneities, *Geophys. J. Int.* **94**, 479–501, 1988.
- Niu, F. and H. Kawakatsu, Direct evidence for the undulation of the 660-km discontinuity beneath Tonga: Comparison of Japan and California array data, *Geophys. Res. Lett.* **22**, 531–534, 1995.
- Niu, F. and H. Kawakatsu, Complex structure of Mantle discontinuities at the tip of the subducting slab beneath northeast China, *J. Phys. Earth* **44**, 701–711, 1996.
- Okada, H., New evidences of the discontinuous structure of the descending lithosphere as revealed by ScSp phases, *J. Phys. Earth* **27**, suppl., S53–S63, 1979.

- Olson, P., P. G. Silver and R. W. Carlson, The large-scale structure of convection in the Earth's mantle, *Nature* **344**, 209–215, 1990.
- Owens, T. J. and G. Zandt, The response of the continental crust-mantle boundary observed on broadband teleseismic receiver functions, *Geophys. Res. Lett.* **12**, 705–708, 1985.
- Owens T. J. and G. Zandt, Implications of crustal property variations for models of Tibetan Plateau evolution. *Nature* **387**, 37–43, 1997.
- Owens, T. J., S. R. Taylor and G. Zandt, Crustal structure at regional seismic test network stations determined from inversion of broadband teleseismic P waveforms, *Bull. Seism. Soc. Am.* **77**, 631–662, 1987.
- Owens, T. J., G. Zandt and S. R. Taylor, Seismic evidence for an ancient rift beneath the Cumberland Plateau, Tennessee: A detailed analysis of broadband teleseismic P waveforms. *J. Geophys. Res.* **89**, 7783–7795, 1984.
- Paulssen, H., Evidence for a sharp 670-km discontinuity as inferred from P-to-S converted waves, *J. Geophys. Res.* **93**, 10489–10500, 1988.
- Peacock, S. M. and K. Wang, Seismic consequences of warm versus cool subduction metamorphism: examples from southwest and northeast Japan, *Science* **286**, 937–939, 1999.
- Petersen, N., J. Gossler, R. Kind, K. Stammer and L. P. Vinnik, Precursors to SS and structure of transition zone of the north-western Pacific, *Geophys. Res. Lett.* **20**, 281–284, 1993.
- Phinney, R. A., Structure of the Earth's crust from spectral behaviour of long-period body waves, *J. Geophys. Res.* **69**, 2997–3107, 1964.
- Priestley K., J. Cipar, A. Egorkin and N. Pavlenkova, Upper-mantle velocity structure beneath the Siberian Platform. *Geophys. J. Int.* **118**, 369–378, 1994.
- Priestley, K. and F. Tilmann, Shear-wave structure of the lithosphere above the Hawaiian hot spot from two-station Rayleigh wave phase velocity measurements, *Geophys. Res. Lett.* **26**, 1493–1496, 1999.
- Revenaugh, J. and T. H. Jordan, Mantle layering from ScS reverberations: 2. The transition zone, *J. Geophys. Res.* **96**, 19763–19780, 1991a.
- Revenaugh, J. and T. H. Jordan, Mantle layering from ScS reverberations: 3. The upper mantle, *J. Geophys. Res.* **96**, 19781–19810, 1991b.
- Revenaugh, J. and S. A. Sipkin, Seismic evidence for silicate melt atop the 410-km mantle discontinuity, *Nature* **369**, 474–476, 1994a.

- Revenaugh, J. and S. A. Sipkin, Mantle discontinuity structure beneath China, *J. Geophys. Res.* **99**, 21911–21927, 1994b.
- Ribe, N. and U. R. Christensen, Melt generation by plumes: a study of Hawaiian volcanism, *J. Geophys. Res.* **99**, 669–682, 1994.
- Ribe, N. M. and U. R. Christensen, The dynamical origin of Hawaiian volcanism, *Earth Planet. Sci. Lett.* **171**, 517–531, 1999.
- Richter F. M. and McKenzie, D. P., On some consequences and possible causes of layered mantle convection, *J. Geophys. Res.* **86**, 6133–6142, 1981.
- Ringwood, A. E., *Composition and Petrology of the Earth's Interior*, McGraw-Hill, New York, 1975.
- Ringwood, A. E. and T. Irifune, Nature of the 650-km seismic discontinuity: implications for mantle dynamics and differentiation, *Nature* **331**, 131–136, 1988.
- Rubie, D. C. and C. R. Ross, Kinetics of the olivine-spinel transformation in subducting lithosphere: Experimental constraints and implications for deep slab processes, *Phys. Earth Planet. Inter.* **86**, 223–241, 1994.
- Russell S. A., T. Lay and E. J. Garnero, Seismic evidence for small-scale dynamics in the lowermost mantle at the root of the Hawaiian hotspot, *Nature* **396**, 255–258, 1998.
- Ryberg, T. and M. Weber, Receiver function arrays: a reflection seismic approach, *Geophys. J. Int.* **141**, 1–11, 2000.
- Ryberg, T., F. Wenzel, J. Mechie, A. Egorkin, K. Fuchs and L. Solodilov, Two-dimensional velocity structure beneath northern Eurasia derived from the super long-range seismic profile Quartz, *Bull. Seism. Soc. Am.* **86**, 857–867, 1996.
- Ryberg, T., F. Wenzel, A. V. Egorkin and L. Solodilov, Short-period observation of the 520 km discontinuity in northern Eurasia, *J. Geophys. Res.* **102**, 5413–5422, 1997.
- Ryberg, T., F. Wenzel, A. V. Egorkin and L. Solodilov, Properties of the mantle transition zone in northern Eurasia, *J. Geophys. Res.* **103**, 811–822, 1998.
- Schmeling, H., R. Monz and D. C. Rubie, The influence of olivine metastability on the dynamics of subduction, *Earth Planet. Sci. Lett.* **165**, 55–66, 1999.
- Schubert, G., D. A. Yuen and D. L. Turcotte, *Geophys. J. R. Astr. Soc.* **42**, 705–735, 1975.

- Searcy, C. K., D. H. Christensen and G. Zandt, Velocity structure beneath College Station Alaska from receiver functions, *Bull. Seism. Soc. Am.* **86**, 232–241, 1996.
- Shearer, P. M., Seismic imaging of upper mantle structure with new evidence for a 520-km discontinuity, *Nature* **344**, 121–126, 1990.
- Shearer P. M., Constraints on upper mantle discontinuities from observations of long-period reflected and converted phases, *J. Geophys. Res.* **96**, 18147–18182, 1991.
- Shearer, P. M., Global mapping of upper mantle reflectors from long-period SS precursors, *Geophys. J. Int.* **115**, 878–904, 1993.
- Shearer, P. M., Transition zone velocity gradients and the 520-km discontinuity, *J. Geophys. Res.* **101**, 3053–3066, 1996.
- Shearer, P. M. and M. P. Flanagan, Seismic velocity and density jumps across the 410- and 660-km discontinuities, *Science* **285**, 1545–1548, 1999.
- Shearer, P. M. and T. G. Masters, Global mapping of topography on the 660-km discontinuity, *Nature* **355**, 791–796, 1992.
- Shen Y., S. C. Solomon, I. Th. Bjarnason and G. M. Purdy, Hot mantle transition zone beneath Iceland and the adjacent Mid-Atlantic Ridge inferred from P-to-S conversions at the 410- and 660-km discontinuities, *Geophys. Res. Lett.* **23**, 3527–3530, 1996.
- Shen, Y., A. F. Sheehan, K. G. Duecker, C. de Groot-Hedlin and H. Gilbert, Mantle discontinuity structure beneath the southern East Pacific Rise from P-to-S converted phases, *Science* **280**, 1232–1235, 1998a.
- Shen Y., S. C. Solomon, I. T., Bjarnason and C. J. Wolfe, Seismic evidence for a lower-mantle origin of the Iceland plume, *Nature* **395**, 62–65, 1998b.
- Silver, P. G., S. L. Beck, T. C. Wallace, C. Meade, S. C. Myers, D. E. James and R. Kuehnel, Rupture characteristics of the deep Bolivia earthquake of 9 June, 1994 and the mechanism of deep-focus earthquakes, *Science* **268**, 69–73, 1995.
- Sobolev, A. V. and I. K. Nikogosian, Petrology of long-lived mantle plume magmatism: Hawaii, Pacific and Reunion Island, Indian Ocean, *Petrology* **2**, 111–144, 1994.
- Sobolev, S. V., H. Zeyen, G. Stoll, F. Werling, R. Altherr and K. Fuchs, Upper mantle temperatures from teleseismic tomography of French Massif Central including effects of composition, mineral reactions, anharmonicity, anelasticity and partial melt. *Earth Planet. Sci. Lett.* **139**, 147–163, 1996.

- Spakman, W., S. Stein, R. van der Hilst and R. Wortel, Resolution experiments for NW Pacific subduction zone tomography, *Geophys. Res. Lett.* **16**, 1079–1100, 1989.
- Stammler, K. and R. Kind, Comment on “Mantle layering from ScS reverberations, 2, The transition zone” by Justin Revenaugh and Thomas H. Jordan, *J. Geophys. Res.* **97**, 17547–17548, 1992.
- Stammler, K., Ein Beitrag zur Untersuchung des oberen Erdmantels mit Hilfe von PS-Konversionsphasen, *Ph.d thesis at the Friedrich-Alexander-University, Erlangen-Nürnberg*, 1992a.
- Stammler, K., R. Kind, N. Petersen, G. Kosarev, L. Vinnik and Q. Liu, The upper mantle discontinuities: correlated or anticorrelated?, *Geophys. Res. Lett.* **19**, 1563–1566, 1992b.
- Stixrude, L., R. J. Hemley, Y. Fei and H. K. Mao, Thermoelasticity of silicate perovskite and magnesiowustite and stratification of the Earth’s mantle, *Science* **257**, 1099–1101, 1992.
- Stunff, Y. L., C. W. Wicks and B. Romanowicz, P’P’ precursors under Africa; evidence for mid-mantle reflectors, *Science* **270**, 74–77, 1995.
- Sung, C. M., Kinetics of the olivine-spinel transition under high pressure and temperature: Experimental results and geophysical implications, in *High-Pressure Science and Technology*, K. D. Timmerhaus and M. S. Barber (Eds.), 31–41. Plenum, N. Y., 1979.
- Sung, C. M. and R. G. Burns, Kinetics of high-pressure phase transformations: Implications to the evolution of the olivine-spinel transition in the downgoing lithosphere and its consequences on the dynamics of the mantle, *Tectonophysics* **31**, 1–32, 1976a.
- Sung, C. M. and R. G. Burns, Kinetics of the olivine-spinel transition: Implications to deep-focus earthquake genesis, *Earth Planet. Sci. Lett.* **32**, 165–170, 1976b.
- Thirot, J. L., J. P. Montagner and L. Vinnik, Upper-mantle seismic discontinuities in a subduction zone (Japan) investigated from P to S converted waves, *Phys. Earth Planet. Inter.* **108**, 61–80, 1998.
- Tibi, R., C. Estabrook and G. Bock, The 1996 June 17 Flores Sea and 1994 March 9 Fiji-Tonga earthquakes: source processes and deep earthquake mechanisms, *Geophys. J. Int.* **138**, 625–642, 1999.
- Vacher, P., A. Mocquet and C. Sotin, Comparison between tomographic structures and models of conversion in the upper mantle, *Geophys. J. Int.* **124**, 45–56, 1996.

- Vacher, P., A. Mocquet and C. Sotin, Computation of seismic profiles from mineral physics: the importance of the non-olivine components for explaining the 660 km discontinuity, *Phys. Earth Planet. Inter.* **106**, 275–298, 1998.
- van der Hilst, R. and T. Seno, Effects of relative plate motion on the deep structure and penetration depth of slabs below the Izu-Bonin and Mariana island arcs, *Earth Planet. Sci. Lett.* **120**, 395–407, 1993.
- van der Hilst, R. D., R. Engdahl, W. Spakman and G. Nolet, Tomographic imaging of subducted lithosphere below northwest Pacific island arcs, *Nature* **353**, 37–43, 1991.
- van der Hilst R. D., E. R. Engdahl and W. Spakman, Tomographic inversion of P and pP data for aspherical mantle structure below the northwest Pacific region, *Geophys. J. Int.* **115**, 264–302, 1993
- van der Hilst, R. D., S. Widiyantoro and R. Engdahl, Evidence for deep mantle circulation from global tomography, *Nature* **386**, 578–584, 1997.
- van der Lee, S., H. Paulssen and G. Nolet, Variability of P660s phases as a consequence of topography of the 660km discontinuity, *Phys. Earth Planet. Inter.* **86**, 147–164, 1994.
- Vidale, J. E. and H. M. Benz, Upper-mantle seismic discontinuities and the thermal structure of subduction zones, *Nature* **356**, 678–683, 1992.
- Vinnik, L. P., Detection of waves converted from P to SV in the mantle, *Phys. Earth Planet. Int.* **15**, 39–45, 1977.
- Vinnik, L., S. Chevrot and J.P. Montagner, Evidence for a stagnant plume in the transition zone? *Geophys. Res. Lett.* **24**, 1007–1010, 1997.
- Vinnik, L., G. Kosarev and N. Petersen, Mantle transition zone beneath Eurasia, *Geophys. Res. Lett.* **23**, 1485–1488, 1996.
- Vinnik, L. P., R. W. E. Green, L. O. Nicolaysen, G. L. Kosarev and N. V. Petersen, Deep structure of the Kaapvaal craton, *Tectonophysics* **262**, 67–75, 1996.
- Walck, M. C., The P-wave upper mantle structure beneath an active spreading center: the Gulf of California, *Geophys. J. R. Astr. Soc.* **76**, 697–723, 1984.
- Watson, S. and D. P. McKenzie, Melt generation by plumes: a study of Hawaiian mechanism, *J. Petrol.* **32**, 501–537, 1991.
- Wessel, P. and W. H. F. Smith, Free software helps map and display data, *EOS Trans. Amer. Geophys. Union* **72**, 441, 445–446, 1991.

- Wessel, P. and W. H. F. Smith, New version of the generic mapping tools (GMT) version 3.0 released, *EOS Trans. Amer. Geophys. Union* **76**, 329, 1995.
- Wicks, C. W. and M. A. Richards, A detailed map of the 660-km discontinuity beneath the Izu-Bonin subduction zone, *Science* **261**, 1424–1427, 1993.
- Widiyantoro, S., B. L. N. Kennett and R. D. van der Hilst, Seismic tomography with P and S data reveals lateral variations in the rigidity of deep slabs, *Earth Planet. Sci. Lett.* **173**, 91–100, 1999.
- Wiens, D. A., J. J. McGuire and P. J. Shore, Evidence for transformational faulting from a deep double seismic zone in Tonga, *Nature* **364**, 790–793, 1993.
- Wilson, J. T. A possible origin of the Hawaiian island, *Can. J. Phys.*, **41**, 863–868, 1963.
- Woods, M. T. and E. A. Okal, Rayleigh-wave dispersion along the Hawaiian Swell: a test of lithospheric thinning by the thermal rejuvenation at a hotspot, *Geophys. J. Int.* **125**, 325–339, 1996.
- Woods, M. T., J.-J. L ev eque and E. A. Okal, Two-station measurements of Rayleigh wave group velocity along the Hawai'ian swell, *Geophys. Res. Lett.* **18**, 105–108, 1991.
- Yuan, X., Teleseismic receiver function study and its application in Tibet and the central Andes, *Ph.d thesis at the Freie Universit at Berlin*, 1999.
- Yuan, X., J. Ni, R. Kind, J. Mechie and E. Sandvol, Lithospheric and upper mantle structure of southern Tibet from a seismological passive source experiment, *J. Geophys. Res.* **102**, 27491–27500, 1997.
- Zandt, G. and C. J. Ammon, Continental crust composition constrained by measurements of crustal Poisson's ratio, *Nature* **374**, 152–154, 1995.
- Zhao, D., A. Hasegawa and H. Kanamori, Deep structure of Japan subduction zone as derived from local, regional, and teleseismic events, *J. Geophys. Res.* **99**, 22313–22329, 1994.
- Zhao, D., T. Matsuzawa, A. Hasegawa, Morphology of the subducting slab boundary in the northeastern Japan arc, *Phys. Earth Planet. Inter.* **102**, 89–104, 1997.
- Zhao, D., Y. Xu, D. A. Wiens, L. Dorman, J. Hildebrand and S. Webb, Depth extent of the Lau back-arc spreading center and its relationship to subduction processes, *Science* **278**, 254–257, 1997.
- Zhong, S. and M. Gurnis, Dynamic interaction between tectonic plates, subducting slabs, and the mantle, *Earth Interact.* **1**, 1997.

Zhou, H., How well can we resolve the deep seismic slab with seismic tomography? *Geophys. Res. Lett.* **15**, 1425–1428, 1988.

Zhou, H. W. and R. W. Clayton, P and S wave travel time inversion for subducting slabs under the island arcs of the northwest Pacific, *J. Geophys. Res.* **95**, 6829–6851, 1990.

Danksagung

Die vorliegende Arbeit entstand am GeoForschungsZentrum Potsdam. Diesem danke ich für die finanzielle Unterstützung, ohne die die Arbeit nicht zustande gekommen wäre.

Für die Überlassung des interessanten Themas, die vielen Diskussionen und Anregungen, und vor allem für die ausgezeichnete Betreuung danke ich meinem Doktorvater Prof. Dr. Rainer Kind. Sein ständiges Interesse war für die Fertigstellung dieser Arbeit sehr hilfreich und motivierend.

Prof. Dr. Serge Shapiro danke ich für die Übernahme des Koreferates.

Dr. Günter Bock und Bernd Schurr danke ich für das Lesen und die Korrekturen des Manuskripts. Ebenso gilt mein Dank Drs. Chuck Estabrook, Stephan Sobolev und Günter Bock für die unzähligen Diskussionen und hilfreichen Hinweise. Bei den Kollegen des Projektbereiches 2.4 (Globale Seismologie, GeoForschungsZentrum Potsdam) bedanke ich mich für die Unterstützung und Zusammenarbeit, insbesondere bei Drs. Winfried Hanka, Jürgen Goßler, Kurt Wylegalla und Günter Asch. Dr. Alexander Rudloff gilt ein besonderer Dank für seine allseitige Hilfe. Mein Dank gebührt Dr. Rigobert Tibi, Jörn Kummerow, Joachim Saul, Bernd Schurr und Dr. Frank Graeber für die Unterstützung und Hilfe. Bei Frau Liane Tröger, Wilhelm Rüsing und Ronny Kopischke bedanke ich mich für die allzeitige Hilfe.

Ein großer Teil der vorliegenden Arbeit wurde mit dem Analyseprogramms *SeismicHanler* durchgeführt (Stammler, 1992a). Sämtliche in dieser Arbeit gezeigten Abbildungen wurden mit der Graphik-Software *GMT (Generic Mapping Tools)* (Wessel and Smith, 1991, 1995) erstellt.

In der vorliegenden Arbeit stammten zahlreiche seismologische Daten von CDSN, GEO-SCOPE, GSN und FREESIA Netzen. Die Daten von Hawaii wurden von der *University of Cambridge* und dem *US Geological Survey* bereitgestellt.

Meinem Mann Xiaohui Yuan danke ich für seine liebevolle Unterstützung der Arbeit und zahlreiche wertvolle Diskussionen, sowie meinem Sohn Yizheng für seine verständnisvolle Nach- und Rücksicht. Meinen Eltern danke ich ganz herzlich für ihre uneingeschränkte Unterstützung und ihr bedingungsloses Vertrauen während meines gesamten Studiums.

Lebenslauf

Name: Xueqing Li
Geburtsdatum: 20. April 1963
Geburtsort: Shanghai, VR China

Schulbildung:

Mär. 1970–Jul. 1976: Nankai Grundschule, Tianjin, VR China
Sep. 1976–Jul. 1981: Nankai Mittelschule, Tianjin, VR China

Hochschulbildung:

Sep. 1981–Jul. 1986: Studium an der University of Science and Technology of China,
Studienfach: Geophysik,
Abschluß: Bachelor of Science (Jul. 1986)
Sep. 1986–Nov. 1989: Postgraduiertenstudium am Institute of Geophysics, State Seismo-
logical Bureau, Beijing.
Studienfach: Seismologie,
Abschluß: Master of Science (Nov. 1989)

Berufstätigkeit:

Nov. 1989–Mär. 1995: Wissenschaftliche Mitarbeiterin am Institute of Geophysics, State
Seismological Bureau, Beijing.
seit Nov. 1996: Wissenschaftliche Mitarbeiterin am GeoForschungsZentrum Pots-
dam

Zentralbibliothek
GFZ Potsdam B 103

00095688X

